12-8-2016

Geothermometry of Two Cascade Geothermal Systems

Donnel Alexander Malkemus
Portland State University

Geothermometry of Two Cascade Geothermal Systems

by

Donnel Alexander Malkemus

A thesis submitted in partial fulfillment of the
requirements for the degree of

Master of Science
in
Geology

Thesis Committee:
Robert B. Perkins, Chair
Max Rudolph
Carl Palmer

Portland State University
2016

ABSTRACT

For this thesis I applied classical and multi-component geothermometry techniques to new water chemistry data from Breitenbush Hot Springs, Oregon and the Wind River Valley, Washington. A total of 20 well, spring, and stream samples from Breitenbush Hot Springs and 4 spring samples from the Wind River Valley were collected and analyzed for major, minor, and select trace anions and cations, as well as stable oxygen and hydrogen isotopes. I used two computer programs, GeoT and RTEst, to conduct multi-component geothermometry reservoir condition estimation on each water sample. Water chemistry data from Breitenbush Hot Springs indicates a range of thermal, nonthermal, and mixed waters in wells and springs. Isotope data from Breitenbush Hot Springs indicates that thermal water is a mix between "andesitic waters" (6-10%) and meteoric water (90-94%) from the crest of the Oregon Cascades. Classical and multi-component geothermometry conducted for Breitenbush samples for this thesis suggest a reservoir temperature of approximately 137 °C, which is close to the bottom hole temperature recorded in the nearby 2,457 meter deep SUNEDCO well of 141 °C, but contrasts with previous applications of geothermometry which estimate a reservoir temperature between 170 and 180 °C for the system. Reservoir estimates from this thesis for the Wind River Valley hot spring samples range from 80 to 100 °C, which is consistent with previous studies. Multi-component geothermometry optimization indicates a loss of CO_2 (i.e. degassing) during the water's ascent at both Breitenbush Hot Springs and the Wind River

Valley, and that dilution from nonthermal water occurs in some samples from both areas. Multi-component geothermometry estimates were generally consistent between RTEst and GeoT; inconsistencies were primarily due to differences between the thermodynamic databases used for each program.

ACKNOWLEDGMENTS

Thank you to my advisor, Ben Perkins, my committee, Max Rudolph and Carl Palmer, Erick Burns for his help with use of PEST, to Nicholas Spycher for GeoT troubleshooting, and to my wife, Kendra for working much harder than me and thus keeping me on track.

TABLE OF CONTENTS

LIST OF TABLES

LIST OF FIGURES

1 INTRODUCTION

Interest in the development of geothermal resources for power generation in the Pacific Northwest has grown in recent years, in part due to mandated targets for renewable energy use from both federal and state governments (Grainey, 2014). In Oregon, geothermal power production is currently limited to sites east of the Cascade Mountains, with four active geothermal power plants and active exploration at several other central and eastern Oregon locations (Sifford, 2014). Elsewhere in the state, thermal waters are used directly as spas and to heat buildings, and radiant earth heating and cooling systems are widespread in urban areas. The success of eastern Oregon geothermal power projects has re-invigorated interest in identifying other areas of Oregon and Washington that could be developed as a geothermal resource.

The Cascade Range has been recognized for its geothermal energy development potential (Hook, 2005). However, this potential has been overshadowed by its challenges, which include the presence of cool, abundant meteoric water, and the apparently small, disconnected nature of the known hydrothermal systems (Guffanti and Muffler, 1995). In addition, despite indications of steep geothermal gradients, the maximum observed water temperatures in deep borings in the Cascades Range are generally less than the desired temperature for a traditional flash-steam power plant. Recent innovations in geothermal power development such as more efficient low temperature, binary phase power plants, and enhanced geothermal systems have the

potential to overcome some of these challenges. In addition to innovations to larger-scale infrastructure development, the tools associated with assessing geothermal potential have also improved, in part due to the advances in computational ability. One field of inquiry that has profited from these developments is geothermometry, the ability to estimate geothermal reservoir temperatures from surface water chemistry data.

This thesis describes the application of geothermometry to two Cascade geothermal systems in an attempt to understand how recent developments in chemical numerical modeling can improve estimates of reservoir characteristics in the Cascade Range. The first geothermal system considered, Breitenbush Hot Springs, profits from a large number of historical studies regarding the region's geothermal potential, including the drilling of numerous deep boreholes and acquisition of thermal gradient data. These data can be used to evaluate the effectiveness of the geothermometric estimates. The second geothermal system, the Wind River Valley, has less data and provides an opportunity to apply the new geothermometers to a less constrained system.

A variety of geothermometers are used for this study, including two automated multi-component geothermometry computer codes. Disparity between the results of the various geothermometers allows for an assessment of their relative efficacies as well as environmental conditions that may affect their results. I present a detailed description of the geothermometers used in this study, as well as their history and evolution in the following section, followed by relevant background information for both study areas considered. I then discuss the methods used in field data collection, laboratory analysis,

and application of quantitative geothermometers. This section is followed by a summary and discussion of results, with separate sections for both of the study areas. I finish by summarizing the conclusions of this thesis.

2 BACKGROUND

2.1 Geothermometry

The original use of the term geothermometry seemed to simply refer to any indication of high temperature with depth (White, 1970). On a theoretical level, this can include large structural or topographic features such as the presence of an active volcano or an active system of extensional tectonics. More localized theoretical indicators might include hot springs or vent systems. The first applied geothermometers were indicators that provided only slightly more specific information than did these geologic features. These so-called qualitative geothermometers included anomalous elemental concentrations or elemental ratios in soil, water, or vapor. Examples of qualitative geothermometers include the enrichment of B, NH_4, HCO_3, Hg, or H_2S in surface waters, the ratios of Cl/F or Cl/SO4 in water or gas, or the presence of Hg in soil (Fournier, 1977). Quantitative geothermometers are methods for generating specific estimates of geothermal reservoir temperatures from surface or well (gas and/or liquid) geochemical data. This section focuses on the development and application of quantitative geothermometers (hereafter geothermometers) that are applied in liquid dominated systems.

The underlying principle of geothermometry is that waters attain chemical equilibrium with host rocks of deep-seated geothermal reservoirs with which they are in

contact, and that the processes governing this equilibrium are temperature dependent. The following five underlying assumptions are typically applied in geothermometry (Fournier, 1977):

1. Reactions between host rock and water fix a certain amount of an indicator in the water.
2. These reactions are governed by thermodynamic equilibrium.
3. There is a sufficient reactive mass of the mineral(s) to allow for equilibrium and enough time elapses in order to achieve equilibrium.
4. Re-equilibration of the indicator does not occur during its ascent from the reservoir to the surface.
5. No mixing of waters occurs between the reservoir and the surface.

There is no fundamental law of chemistry or physics that establishes any of these assumptions to be true; however, the general accumulation of information from geothermal sites has led to consistent demonstration that equilibrium conditions are likely to be present, thus promoting the continued use of quantitative geothermometry and its assumptions (Arnórsson, 2000). During application of geothermometry, it is possible to test the validity of each assumption.

2.1.1 Classical Geothermometers

The study of geothermometry resulted from laboratory investigations into the solubility of quartz at various temperatures and pressures (particularly high temperature,

high pressure) in the 1940s and 1950s (Walther and Helgeson, 1977). Various geochemical models were developed to fit equations describing silica speciation to the observed laboratory solubility measurements (Walther and Helgeson, 1977). It is from these models that the idea of geothermometry seems to have grown. If certain concentrations of aqueous silica can be predicted at certain temperatures, then it stands to reason that temperatures can be predicted by silica concentrations. The earliest applications of quantitative geothermometry to geothermal environments appear to have been in 1966, at wells drilled in Wairaki, New Zealand (Mahon, 1966), and at hot springs in Yellowstone National park (Fournier and Rowe, 1966). Both studies were based on quartz solubility with temperature curves developed by Morey et al. (1962). Estimated temperatures from silica concentrations at the Wairaki well were 246 to 252°C, which closely resembled a maximum measured borehole temperature of 250°C (Mahon, 1966). Estimated temperatures in Yellowstone exceeded maximum borehole temperatures, but drilling was stopped before the maximum temperature had been reached (Fournier and Rowe, 1966). These early examples of success seemed to demonstrate that quartz solubility measurements conducted in pure water in a laboratory environment underwent the same processes as did highly mineralized water at depth, which encouraged the continued study and refinement of geothermometers (Fournier and Rowe, 1966). By the 1970s, several quantitative geothermometers had been developed, and silica geothermometers were applied in various environments and consistently improved to

match new analytical data and actual field observations. The following sections describe several classical geothermometers that are used for comparison purposes in this thesis.

2.1.1.1 Geothermometry of Fournier

Several geothermometers were proposed by Robert Fournier in the 1970s for different cations and cation ratios (Fournier and Truesdell, 1970; Fournier and Truesdell, 1973; Truesdell and Fournier, 1976; Fournier, 1977; Fournier and Potter, 1979). All of these geothermometers were based on empirical fitting of curves to data. Equations relating temperature to solubility for quartz and its polymorphs were summarized in Fournier, 1977. The following equations for amorphous silica, β-cristobalite, α-cristobalite, and chalcedony are still applied in geothermal investigations:

$$\text{Amorphous Silica: } T = \frac{731}{4.52 - \log S}$$

$$\beta \text{ Cristobalite: } T = \frac{781}{4.51 - \log S}$$

$$\alpha \text{ Cristobalite: } T = \frac{1000}{4.78 - \log S}$$

$$\text{Chalcedony: } T = \frac{1032}{4.69 - \log S}$$

Where T is temperature in K and S is silica concentration as SiO_2 in mg/kg.

In addition to silica, other cations were beginning to be assessed for their potential use as geothermometers. In 1979, Fournier and Potter published a version of a Na, Ca,

and K geothermometer that is still in use (Fournier and Potter, 1979). The justification behind this alkali geothermometer is essentially that of equilibrium with feldspars related to the equilibrium equation (Fournier and Truesdell, 1973):

$$K^+ + \text{Na feldspar} = Na^+ + \text{K feldspar}$$

Simply comparing Na to K was found to be problematic because experimental results of their relationship with temperature varied depending on which of the various minerals containing these elements were used for the basis of the reaction (Fournier and Truesdell, 1973). Although not necessarily involved in each reaction, it was observed that the addition of Ca to the Na/K equations resulted in a more predictive temperature estimate. It was suggested that Ca competes with both K and Na, but has a relatively greater effect on the abundance of K than Na in warmer waters, due to the higher general ratio of Na/K (i.e. there is less K so any missing is more noticeable). In lower temperature environments, there is generally less of both elements, so Ca competes with both elements with less apparent bias (Fournier and Truesdell, 1973). The resultant equation was determined to be:

$$T = \frac{1647}{\log\left(\frac{Na}{K}\right) + \beta \log\left(\frac{\sqrt{Ca}}{Na}\right) + 2.24}$$

Where Na, K, and Ca are the molal concentrations of sodium, potassium, and calcium, respectively, T is temperature in K, and β is either 1/3 or 4/3 depending on the log ratio

of $\frac{\sqrt{Ca}}{Na}$ and the resultant temperature estimate (Fournier and Truesdell, 1973). Figure 1 shows the fit between the Na-K-Ca geothermometer and the data on which it is based.

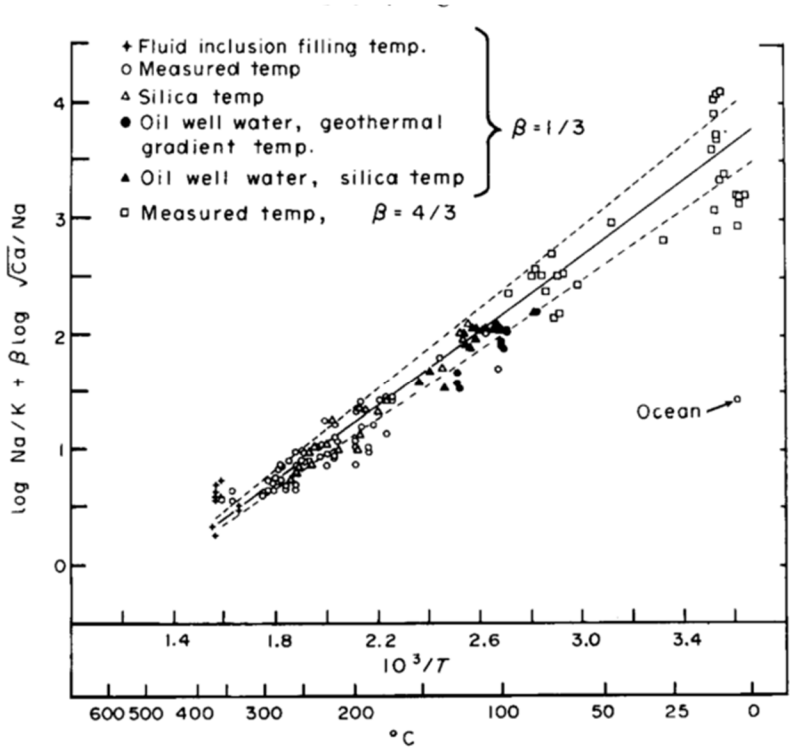

Figure 1: The fit between the Na-K-Ca geothermometer and chemical data, from Fournier, 1977.

This estimate was found to work well for high temperature systems and poorly for low temperature, magnesium-rich systems, which tended to drastically overestimate temperatures. For example, an analysis of ocean water resulted in an estimated "reservoir" temperature of 173°C (Fournier and Potter, 1979). It was observed that Mg was generally present in low concentrations in high temperature geothermal waters and relatively high concentrations in lower temperature waters. Initially both meteoric and

acidic magmatic waters will preferentially dissolve Mg bearing minerals; however, once pH and temperature reach stable conditions for Mg bearing chlorites and clays, the waters tend to show relative depletion of Mg as the minerals precipitate (Arnórsson, 2000). With this in mind, the equations were again corrected, this time to include Mg. The application of the Mg correction involved first calculating the ratio of Mg to Mg + Ca + K. If this ratio was high (R, defined below, greater than 50), it was recommended that the surface spring water temperature be accepted as the reservoir temperature. If the ratio was low (R < 5), it was recommended to ignore Mg, and apply the Na-K-Ca equations. If the ratio were moderate (5 < R < 50), the following equations were to be applied (Fournier and Potter, 1979):

$$T_{Mg} = 10.66 - 4.7472\log R + 325.87(\log R)^2 - 1.032 * \frac{10^5(\log R^2)}{T} - 1.968 * 10^7 * \frac{\log R}{T^2} + 1.605 * 10^7(\log R)^3/T^2$$

Where T_{Mg} is the corrected temperature for magnesium, $R = \frac{Mg}{Mg+0.61Ca+0.31K} * 1000$, and T is the temperature determined by the Na, K, Ca geothermometer equation described previously (Fournier and Potter, 1979).

2.1.1.2 Na/Li Geothermometer of Fouillac and Michard

Citing the tendency for silica geothermometers to underestimate high temperature environments, and Na-K geothermometers to overestimate low temperature

environments, an alternative approach was suggested, independent of these methods (Fouillac and Michard, 1981). Li, Cl, and Na concentrations of over 100 samples from a variety of water-type and thermal environments were plotted in various configurations against temperature (Fouillac and Michard, 1981). The following fits were obtained:

$$T = \frac{1000}{0.389 + \log\left(\frac{Na}{Li}\right)} \text{ if } Cl < 0.3 \frac{mol}{kg}, \text{and}$$

$$T = \frac{1195}{0.130 + \log\left(\frac{Na}{Li}\right)} \text{ if } Cl > 0.3 \frac{mol}{kg}$$

Where T is temperature in K, and Na and Li are concentrations in mmol/kg. The governing mineral equilibrium behind these apparent relationships was not determined by its authors. It was acknowledged that there is little chance of water being in equilibrium with a lithium dominant mineral, that lithium does not readily substitute for Na due to their differences in ionic radii, and that there was no observed relationship between lithium concentration and water-rock ratio (Fouillac and Michard, 1981). Nevertheless, the equations were determined to work in many environments.

2.1.1.3 Quartz Geothermometer of Fournier and Potter 1982

After several iterations of equations relating temperature to the solubility of quartz, a relationship encompassing all of the solubility data available up to the date of publication (i.e. 1982) was developed by Fournier and Potter (1982). Previous equations had been successful at interpreting specific experimental results, but were in conflict with

other laboratory results (Fournier and Potter, 1982). A set of predictive equations developed by Walther and Helgeson (1977) using a regression analysis of all previously available data and incorporating enthalpy and CO_2 concentrations was predictive of a majority of temperature and pressure environments, but did not seem to apply to some high temperature-low pressure results. Fournier and Potter (1982) attempted to improve upon these equations, with applicability at all temperatures and pressures, and to greatly simplify them into an easily applied format. The relationship between the logarithmic expression for molal silica concentration and the logarithmic expression of the specific volume of water were observed to have a roughly linear relationship at constant temperature. A multiple linear regression computer program was used to generate the following equation based on data from 518 experiments:

$$\log M = -4.66206 + 0.0034063T + \frac{2179.7}{T} - \frac{1.1292 * 10^6}{T^2} + 1.3543 * \frac{10^8}{T^3} - \left(0.0014180T + \frac{806.97}{T}\right) * \log V + 3.9465 * 10^{-4} T * \log V^2$$

Where M is molal silica concentration, V is specific volume of pure water, and T is temperature in K (Fournier and Potter, 1982).

Holding specific volume constant, the equation can be solved for temperature (Arnórsson, 2000):

$$T = -42.2 + 0.28831S - 3.6686 * 10^{-4} S^2 + 3.1665 * 10^{-7} S^3 + 87.841 \log S$$

Where S represents silica concentration as SiO_2 in mg/kg.

2.1.1.4 Giggenbach Diagrams

In 1988, Giggenbach (1988) developed a ternary diagram from which to determine both temperature estimates and the extent to which waters are in equilibrium with a presumed mineral assemblage based on average crustal rocks and their hypothetical interaction with rising magmatic fluids. The three axes of the diagram represent observed and theoretical relationships between Na, K, and Mg cations. The relative ratio of these diagram end members was thought to suggest the stage of evolution of the thermal fluid, with an early state containing a comparatively large percentage of K and Mg relative to Na, a partial equilibrium state where the three cations are relatively balanced, and a fully equilibrated state at which Na is comparatively more dominant. It should be noted that the Na concentration is divided by 1000, the K concentration is divided by 100, and the Mg concentration is taken as its square root. In this regard, even the immature fluids have significantly more Na than the other cations, just less compared to the partially and fully equilibrated waters. The justification for this relationship is the initial dissolution of rock when exposed to acidic magmatic fluids liberates all three cations, and subsequent precipitation of K and Mg mineral species removes these cations from the fluid while leaving considerable dissolved Na behind (Giggenbach, 1988). The temperature dependence of these constituents used by Giggenbach is represented by the following three equations:

$L_{KN} = \log\left(\frac{C_{K+}}{C_{Na+}}\right) = 1.75 - (\frac{1{,}390}{T})$ for the K-Na axis

$L_{KM} = \log\left(\frac{C^2{}_{K^+}}{C_{Mg^{2+}}}\right) = 14.0 - (\frac{4{,}410}{T})$ for the K-Mg axis, and

$L_{NM} = \log\left(\frac{C^2{}_{Na^+}}{C_{Mg^{2+}}}\right) = 10.5 - (\frac{1{,}630}{T})$ for the Na-Mg axis.

The temperature and relative equilibration of a water sample can be found by plotting on the ternary diagram, as shown in Figure 2.

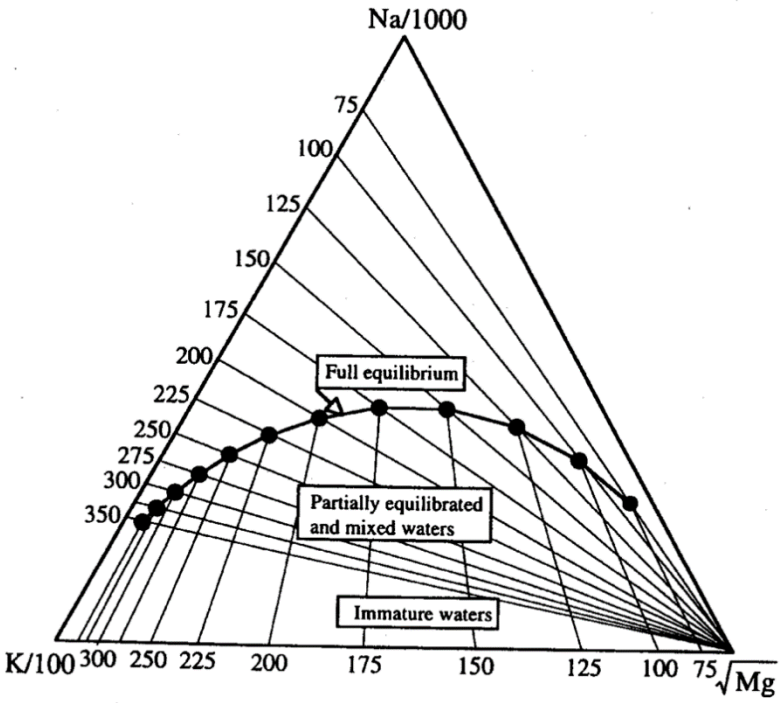

Figure 2: An example of a Giggenbach diagram, from Arnórsson 2000.

2.1.1.5 Silica Geothermometry in Arnórsson, 2000

Arnórsson (2000) summarizes the use of silica geothermometers, suggesting that the experimentally determined chalcedony geothermometer of Fournier (1977) should be used for temperatures below about 180°C, and that the silica geothermometer of Arnórsson (1998) should be used for higher temperatures. The 1998 silica geothermometer is an expanded version of Fournier and Potter's (1982) equation, based on an additional two decades of data. The equation is:

$$T = -55.3 + 0.3659S - 5.3954 * 10^{-4}S^2 + 5.5132 * 10^{-7}S^3 + 74.360 * \log S$$

2.1.1.6 Statistical Analysis of Classical Geothermometers

Verma and Santoyo (1997) used statistical data analysis to improve upon Fournier and Potter's 1982 silica geothermometer, Fournier and Potter's 1979 Na-K geothermometer, and Fouillac and Michard's 1981 Na-Li geothermometer. For the Na-K and Na-Li geothermometers, they developed a set of equations to find outlier residual values from application of the equations compared to observed values (borehole temperatures). This led to their discarding several values that were used to make the initial fits. With these values removed, they employed a system of linear regressions to generate coefficients that matched the remaining values better than the original equations. For Fournier and Potter's silica geothermometer, they were unable to throw out outliers in the same fashion because the coefficients appeared to be "perfect," perhaps as a result of the laboratory setting from which the original data were generated, or from initial

discarding of data that appeared as outliers (Verma and Santoyo, 1997). A close analysis of the equations led them to propose yet another set of equations that fit the data slightly better, one employing a fourth degree polynomial for temperatures below 210°C, and a simple linear equation for temperatures greater than 210°C. The new equations for all three geothermometers reduced errors when compared to the original equations in both the data from which the original equations were developed and other geothermal areas considered in the paper (Verma and Santoyo, 1997).

In 2008, the statistical methods described above were incorporated into the computer program SolGeo. The program incorporates 35 solute geothermometers, and develops estimates of relative uncertainty for each estimate (Verma et al., 2008). Outlier data points were found in the majority of geothermometers and the equations were recalculated with the data from the original studies. The authors also found a number of errors due to improper unit conversion (Verma et al., 2008). When outlier and conversion errors were accounted for, the various solute geothermometers were compared to a database that the authors created using geothermal reservoir conditions compiled from over 300 samples collected from geothermal fields in 17 countries. The authors concluded that the Na-K geothermometers were the most reliable reservoir estimators, and suggested that this simple elemental ratio was the least likely to be disturbed by processes such as mixing or degassing on route to the surface (Verma et al., 2008).

2.1.2 Multi-component Geothermometry

In 1984, Reed and Spycher introduced a technique utilizing bulk water chemistry that assesses the temperature dependent saturation indices of a suite of minerals (Reed and Spycher, 1984). This is done by first calculating ion activity for the component species of a particular mineral based on measured concentrations and taking the product of the species to arrive at an ion activity product (Q) for the reaction. The ratio of Q to the equilibrium constant (K) of the mineral dissolution reaction defines the reaction quotient for that chemical reaction, the log of which is taken as the saturation index (SI = log (Q/K)). A zero value for the saturation index implies that equilibrium conditions are met, a negative value implies unsaturated conditions, and a positive value implies supersaturated conditions. Because K is temperature dependent and Q is dependent on both temperature and the concentration of dissolved components, SI varies with both temperature and the concentration of dissolved components. For a given Q, it is possible to plot SI as a function of temperature.

With the assumption of equilibrium between water and a particular mineral, the equilibrium temperature will correspond to the x-intercept of a plot of SI versus temperature (Reed, 1982). When this is done for a suite of minerals that have equilibrated with a given water, the plots of each mineral's SI will intersect the x-axis at the same point, as shown in Figure 3. Reed and Spycher compared this method of estimating temperature to measured borehole temperatures and classical geothermometers (Reed and Spycher, 1984). Potential reasons for disagreement between estimates included

lack of equilibration of waters with the mineral(s) used for a certain classical geothermometer (i.e. feldspars with a Na-K geothermometer), apparent dilution of thermal fluids by other waters causing a displacement of equilibrium conditions away from the x-axis (i.e. multiple minerals SI intersect, but not at SI = 0), or not attaining equilibrium with any mineral assemblage (i.e. a wide spread SI versus temperature curves) (Reed and Spycher, 1984). Figure 4 shows a SI versus temperature plot for a sample for which equilibrium conditions were apparently not achieved (Arnórsson, 2000).

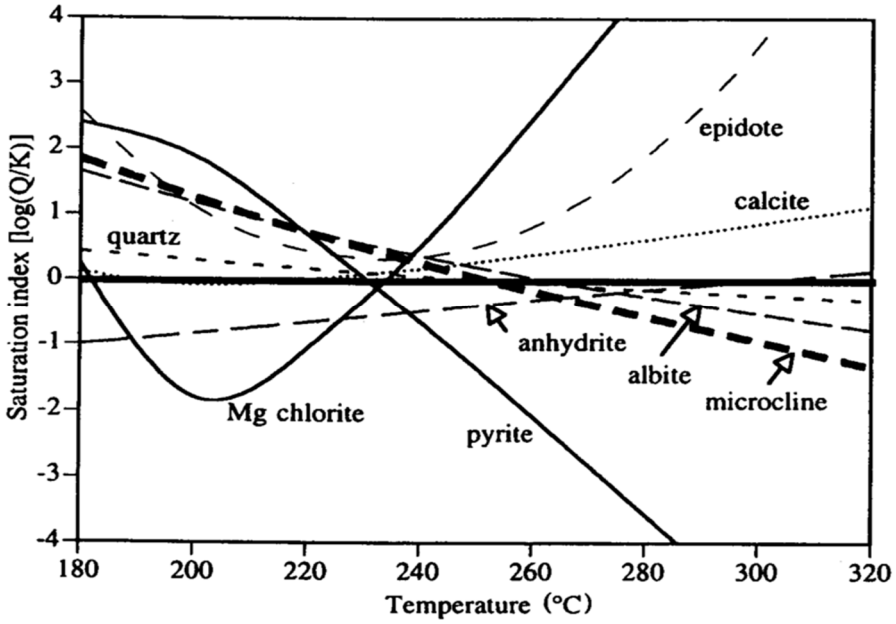

Figure 3: Mineral saturation showing approximate equilibrium at about 230 to 250°C from a well in Krafla, Iceland with a measured temperature of 230°C, from Arnórsson, 2000.

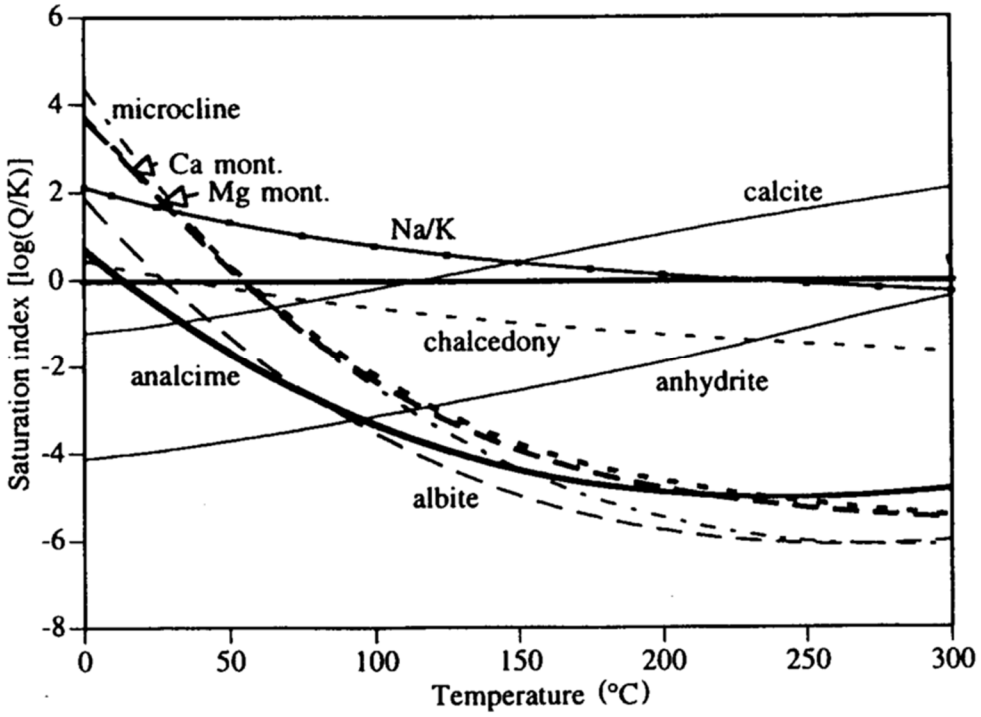

Figure 4: An example of apparent dis-equilibrium conditions on the multi-component plot, from a surface water sample of the Svarta River in Iceland, from Arnórsson, 2000.

2.1.2.1 Aluminum "Correction"

In 1998, Pang and Reed published a method of back-calculating Al concentrations of waters to make up for the common lack of aluminum data in many chemical analysis that resulted because of Al's typical low concentrations (<1 μmol) under circumneutral pH conditions and the lack of readily accessible trace element measurement techniques prior to the introduction of bench top inductively coupled plasma mass spectrometers (ICP-MS) in the mid-1990s. Aluminum is a necessary component for multi-component

geothermometry given its occurrence as a major element in common hydrothermal alteration minerals, feldspars, and micas (Pang and Reed, 1998). The correction procedure involves assuming an alumino-silicate mineral controls aluminum in the system and solving for the Al concentration by forcing that mineral into equilibrium at a given temperature (Pang and Reed, 1998). This procedure can also be applied to Fe, Mg or other elements not present in the original assemblage. This method was applied to a hot spring sample collected from Breitenbush Hot Springs, located in the Oregon Cascades. Both Fe and Al were forced into equilibrium, and a reservoir CO_2 concentration was reconstructed based on equilibrium with calcite. This method resulted in several minerals achieving equilibrium at an estimated temperature of 180°C (Pang and Reed, 1998; Figure 5).

In an analysis of sedimentary basin waters in California, Texas, and Norway, Palandri et al. (2001) developed several methods for reconstructing the composition of waters present at depth for use in multi-component geothermometry. Using a similar method to the aluminum concentration estimation, silica concentrations in several waters were estimated by forcing equilibrium with quartz and chalcedony, and checking the results against a SI versus temperature plot (Palandri et al., 2001). In other waters that had silica data, but which did not seem to be at equilibrium, it was posited that the filtering of ferrous silica precipitates that may have formed during cooling upon ascent had reduced the measured values. When additional silica and iron were added to the reported values, apparent equilibrium among mineral suites was achieved (Palandri et al.,

2001). The assumption that calcite was saturated at depth was used to correct alkalinity data to account for organic acids and to add CO_2 back to the system that may have been lost due to degassing. The relative amount of carbon allotted to organic acid versus CO_2 was determined by observing the extent to which added CO_2 affected the hypothetical reservoir pH, and the extent to which the assumed mineral suites could reach equilibrium based on this pH (Palandri et al., 2001).

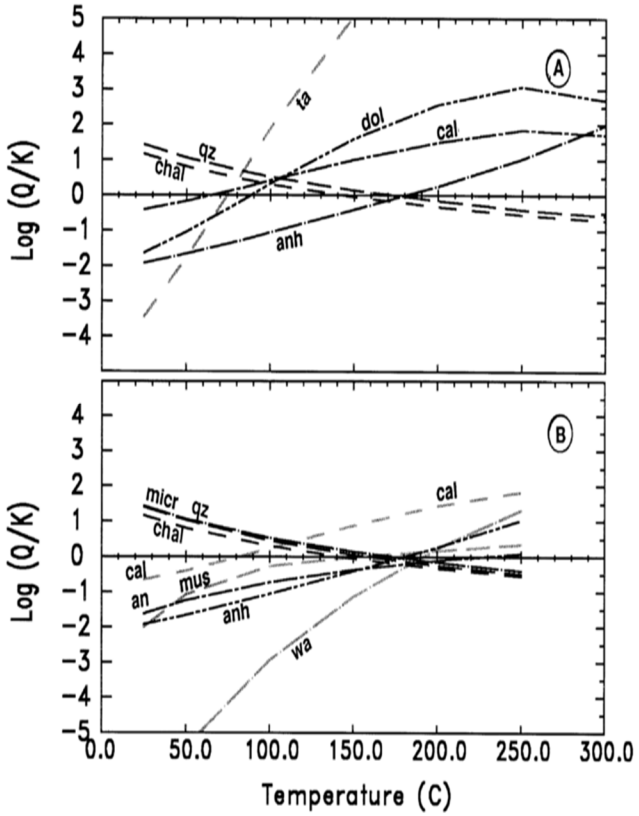

Figure 5: a) SI versus temperature from raw data collected at Breitenbush Hot Springs (Ingebritsen et al., 1992) showing relative scatter and colder equilibrium temperatures. b) The same data with aluminum and iron added to the system via forced equilibrium, from Pang and Reed, 1998.

2.1.2.2 GeoT

In 2011, Spycher et al. (2011) published a description of an automated multi-component geothermometry computer application. The mechanics of the program allow for similar methods of reconstruction of initial reservoir characteristics as those used in Palandri and Reed (2001), including mixing with shallow waters or other end-members, re-constituting gas fractions that may have escaped from the system, and forcing equilibrium with particular minerals in order to extrapolate missing chemical data or concentrations lost to precipitation. The software, GeoT, was designed to be compatible with parameter estimation software such as iTOUGH2 and PEST in order to provide optimization of unknown parameters. It also allows for the simultaneous statistical and optimization analysis of up to 100 water chemistry samples, which allows for reduction of error across a particular geothermal system (Spycher et al., 2011). In addition to calculating (or plotting) SI versus temperature, the statistics of optimized minima are calculated and can be used to generate a companion chart showing statistics with temperature for reference (Figure 6).

GeoT was initially tested on fluids from Dixie Valley, Nevada and produced reservoir temperature estimates close to measured borehole temperatures (Spycher et al., 2011). A groundwater flow model of the Dixie Valley was constructed with various simulated groundwater flow rates and rock surface area to water ratios. The model was coupled with GeoT to find correlations between flow properties and apparent equilibrium conditions. The model yielded minimum flow rates (about 1 meter per day) and reactive

to nonreactive surface area ratios (0.001-1) that were considered to be necessary to effectively transport thermal water from the estimated reservoir depth to surface springs while maintaining the equilibrium signature (Wanner et al., 2013). GeoT has also been applied at the Newberry Caldera enhanced geothermal system (EGS) site to help estimate reservoir temperatures (Sonnenthal et al., 2012). Due to the absence of reliable aluminum data, GeoT was used to generate aluminum estimates by separate forced equilibration with muscovite and kaolinite. Depending on which mineral was used for this estimate, different equilibrium mineral assemblages and temperatures were generated, demonstrating the sensitivity of the estimates to aluminum concentrations (Sonnenthal et al., 2012).

A recent application of GeoT involved a relatively unconstrained geothermal area in Ecuador (Gherardi and Spycher, 2014). Little subsurface mineralogical data was available and the water chemical analyses lacked several significant components. Various combinations of minerals and thermodynamic parameters were applied until optimization was achieved. Eventually, they were able to constrain aluminum by potassium feldspar, magnesium by clinochlore, iron by magnetite, dissolved sulfide by pyrite, and a reservoir temperature of 260±2 °C. This value contrasted greatly with that of classical geothermometers for non-reconstructed water concentrations of 89 to 236 °C (Gherardi and Spycher, 2014).

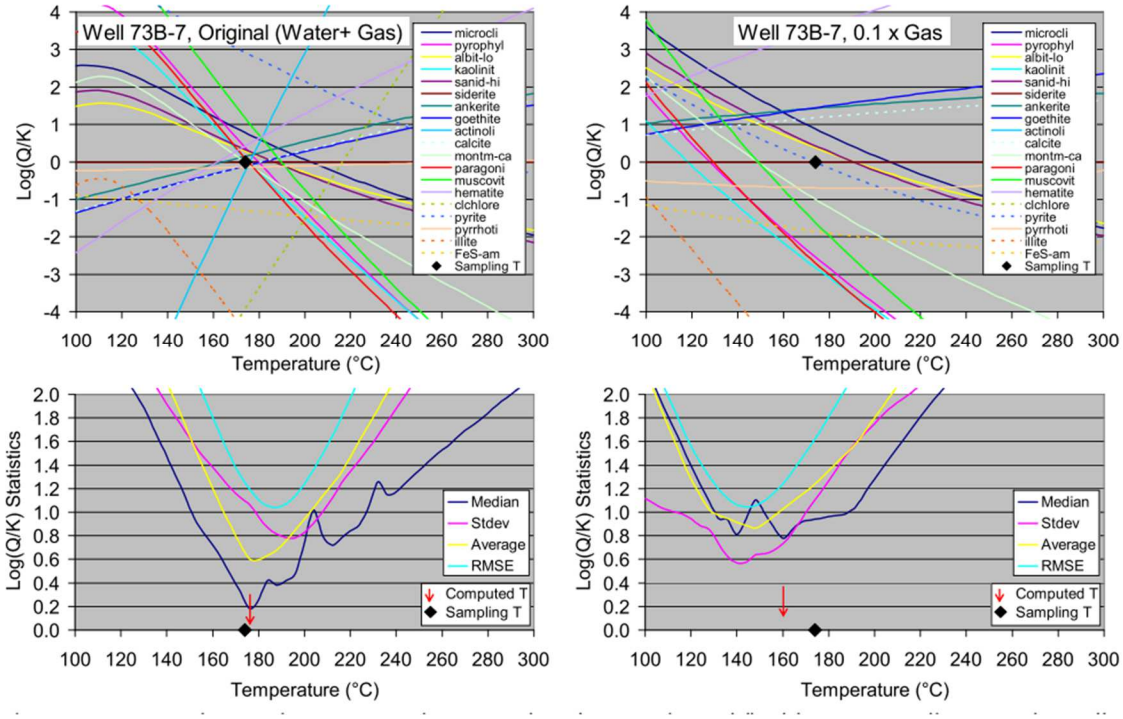

Figure 6: Output from GeoT. Top left chart shows original SI versus temperature plot. Top right chart shows the same plot with 10% reconstituted gas. The bottom charts show the associated statistics, from Spycher et al., 2011.

2.1.2.3 RTEst

Another recently developed computer program (RTEst) also automates multi-component geothermometry. RTEst was developed at the Idaho National Laboratory and estimates equilibrium conditions by acting as an intermediary between Geochemists Workbench, a suite of programs focused on aqueous geochemistry, and PEST, a parameter estimation program (Palmer, 2014). RTEst guides the user in the selection of a mineral assemblage based on minerals commonly associated with differing rock types, general water chemistries, and temperature ranges and verifies that the selected suite of minerals is compatible with the Gibbs phase rule (although it allows you to ignore the Gibbs phase rule if desired; Palmer, 2014). RTEst is able to adjust temperature, steam-fraction, end-member mixing percentage, and CO_2 fugacity to minimize an objective function that is the weighted sum of squares of the saturation indices of the selected mineral suite (Palmer, 2014). There are three built-in weighting procedures utilizing typical analytical uncertainties and mineral stoichiometry to place more weight on minerals with more certainty during its iterative calculation of the objective function (Palmer, 2014).

RTEst was used to generate estimates of equilibrium reservoir temperatures from spring samples collected in the Snake River Plain, Idaho (Neupane et al., 2014). The study was able to reduce uncertainties to between 2 and 20°C, which greatly improves on traditional geothermometry techniques that produced results varying as much as 80°C for the same samples (Neupane et al., 2014). Once again, due to unreliable aluminum data on

some samples, aluminum concentrations were estimated by forced equilibrium with potassium feldspar as per Pang and Reed, 1998 (Neupane et al., 2014). The apparent effectiveness of RTEst in the Snake River Plain motivated its use in this thesis at the study areas described in the following sections.

2.2 Study Areas

Two Cascade geothermal areas were evaluated using the geothermometers described in section 2.1. The following sections provide some background information regarding the geologic context of the areas, including past geothermal assessments.

2.2.1 Breitenbush Hot Springs

Breitenbush Hot Springs is located in the central Oregon Cascades, approximately 15 kilometers northwest of Mount Jefferson, along the Breitenbush River (Fig. 7). Geothermal interest in the Breitenbush area dates back to its original settlement in the late 1800s and the establishment of a hot spring resort in the early 20th century. The geothermal potential of Breitenbush has been the focus of several past studies that have included both classical and multi-component geothermometric assessments. The following sections summarize the geologic and structural framework of the Breitenbush area and the past assessment of its geothermal potential.

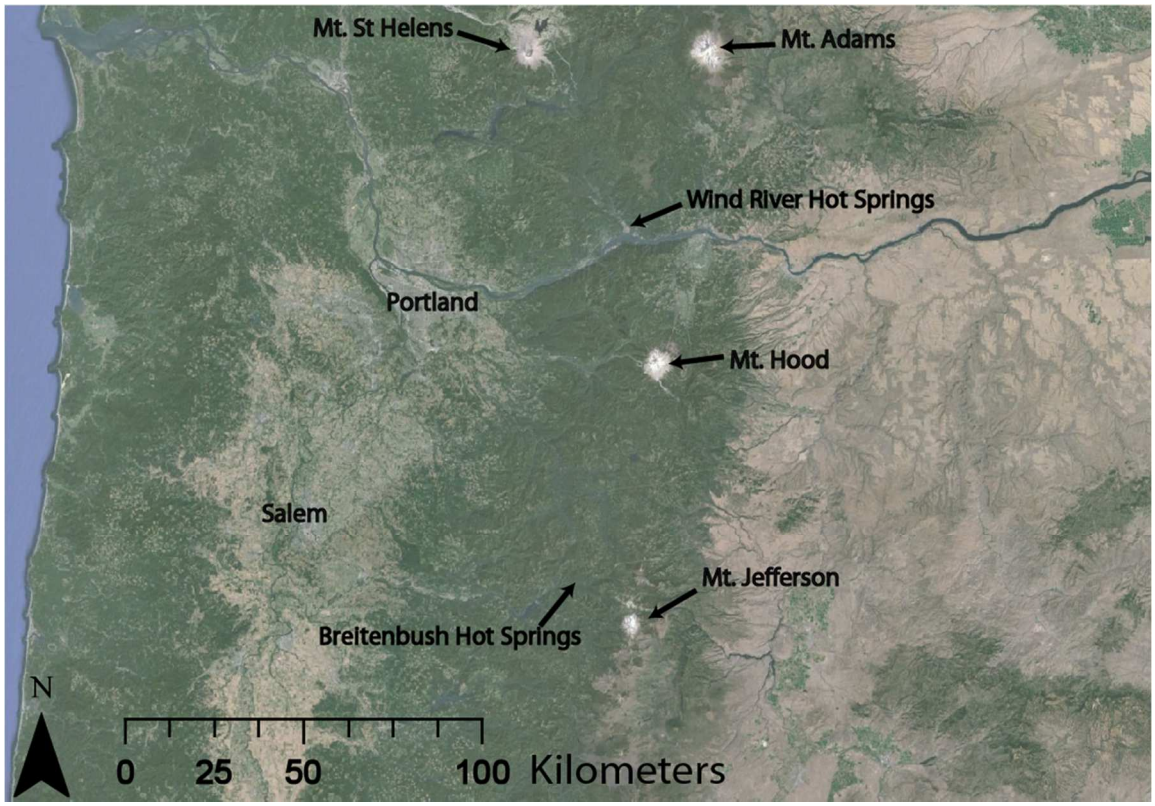

Figure 7: Breitenbush and Wind River Hot Springs regional location map. Image from Google Earth.

2.2.1.1 General Geologic Framework

The bulk of the Cascade Range can be divided broadly into two major stratigraphic sections, both of which are related to arc volcanism associated with the subduction of the Juan de Fuca plate beneath the North American plate: the Western Cascades Group (WCG) and the High Cascades Group (HCG) (Hammond, 1979). The WCG is composed of a thick (5 to 8.5 km) section of volcanic and volcaniclastic rocks, generally older than 12 Ma (Hammond, 1979). In the Breitenbush area, the WCG consists

of a diverse array of pyroclastic flows and lahars, basaltic to rhyodacitic lava flows, tuffaceous sandstones, and siltstones, and is designated the Breitenbush Formation (Figures 8 and 9; Sherrod and Conrey, 1988). The Breitenbush Formation is at least 2.5 km thick in the study area with an approximate age range of 25 to 18 Ma (Sherrod and Conrey, 1988). The HCG is composed of recent (about 5 Ma to present) andesitic and basaltic lava flows, with lesser pyroclastic flows (Hammond, 1979). Near the Breitenbush area, the HCG consists of "thick, stubby" andesite, dacite, and rhyodacite flows, generally higher in silica than other areas of the Cascades, the youngest of which is represented by recent flows at Mount Jefferson, approximately 15 km southeast of Breitenbush Hot Springs (Figures 8 and 9; Sherrod and Conrey, 1988).

The Breitenbush Formation is folded into a northeast plunging anticline associated with northwest-southeast crustal shortening that began approximately 18 Ma and ended by 12 Ma (Priest, 1990). The axis of the anticline is approximately 5 km northwest of Breitenbush Hot Springs (Sherrod and Conrey, 1988). The younger HCG volcanics unconformably overlie the anticline. Northwest trending faults present in a wide region of central and northern Oregon displace rocks older than about middle Miocene. Fewer north- and northwest- trending faults, including several mapped in the vicinity of Breitenbush Hot Springs, displace Pliocene and younger rocks (Figure 8).

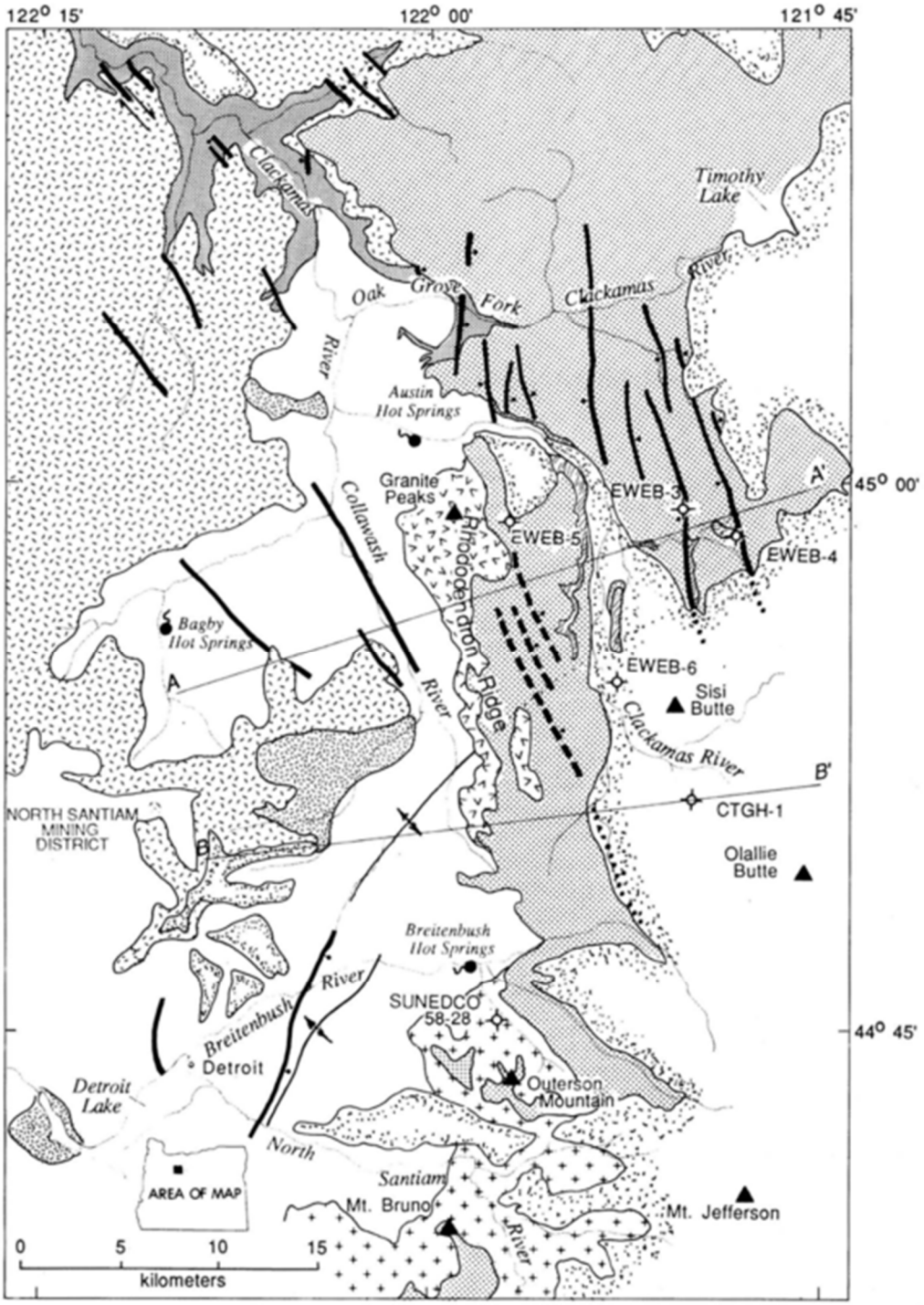

Figure 8: Geologic Map of the Breitenbush area (map), from Sherrod and Conrey, 1988.

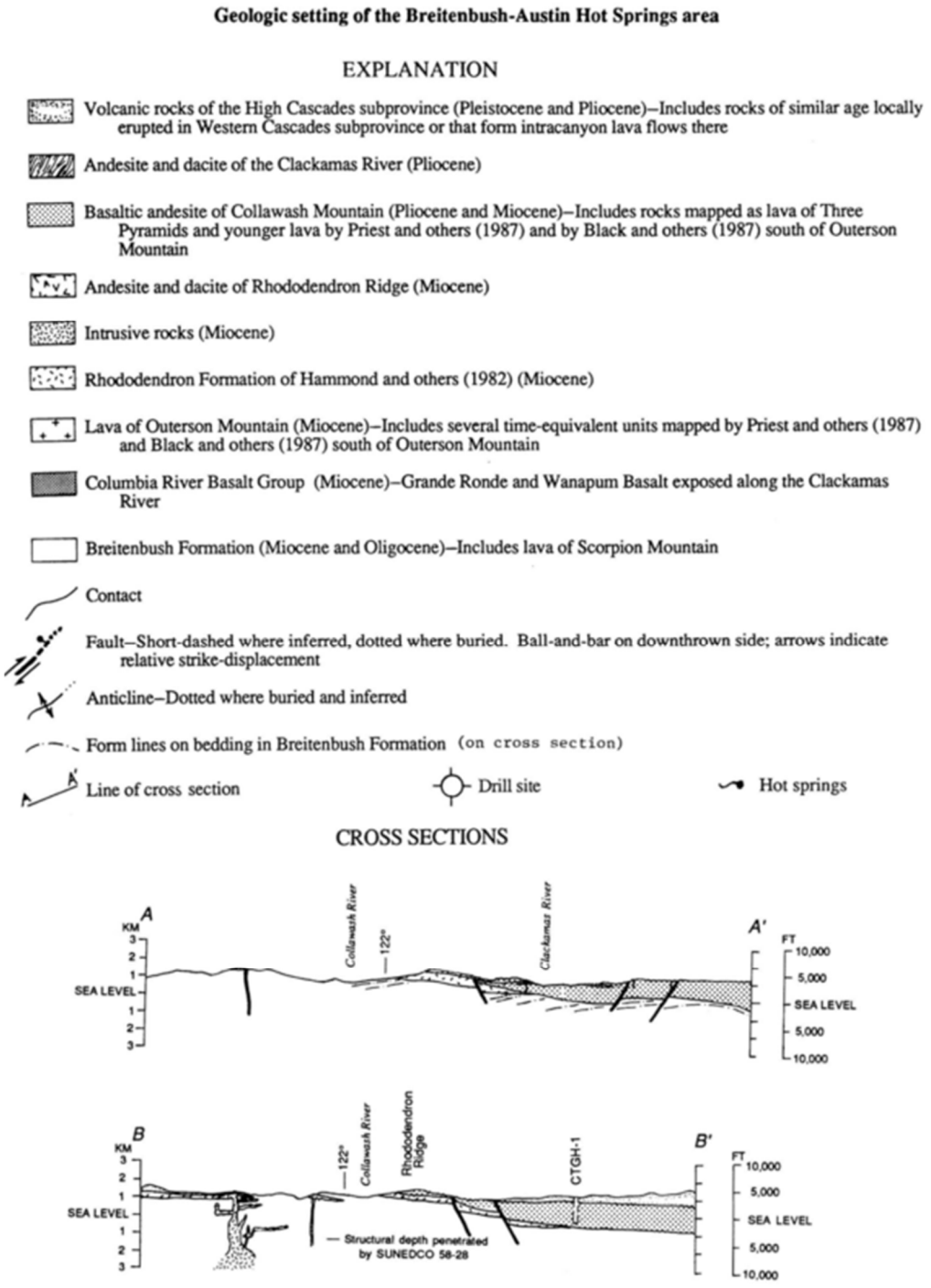

Figure 9: Geologic Map of the Breitenbush area (legend and cross sections), from Sherrod and Conrey, 1988.

2.2.1.2 Geothermal Exploration and Characterization

In the 1970s and 80s, several investigations were conducted to assess geothermal potential of the Breitenbush Hot Springs area. The bulk of the results were published in a 1988 USGS special report, from which the majority of this exploration history is summarized (Sherrod, 1988).

Several geothermal exploration wells were installed in the vicinity of Breitenbush Hot Springs (Figure 8). In 1979, 4 temperature gradient holes (EWEB-3 through EWEB-6) were drilled close to the crest of the Cascades, approximately 15 to 20 km north-northeast of Breitenbush Hot Springs, through Miocene to Pleistocene basaltic andesite to rhyodacite flows (Conrey and Sherrod, 1988). In 1981, a 2,457 meter deep well was drilled approximately 3 km southeast of Breitenbush Hot Springs (SUNEDCO well; Bargar, 1994). Except for the upper ~100 meters, which extend through andesite and basalt flows, the entirety of the well was drilled through volcaniclastic deposits of the Breitenbush Formation (Bargar, 1994). In 1986, a 1,463 meter hole was advanced near Olallie Butte, approximately 10 km northeast of Breitenbush Hot Springs. The majority of the hole was drilled through basaltic andesite, with relatively minor intervals of basalt, dacite, and tuff (Conrey and Sherrod, 1988). In addition to these wells, several wells were drilled at the Breitenbush Hot Springs Resort for use as district heating and for filling soaking pools (Figure 10). Table 1 lists these wells and describes pertinent information such as depth, temperature, use, and approximate flow rates. Well logs from the Oregon Water Resources Department are included in Appendix A.

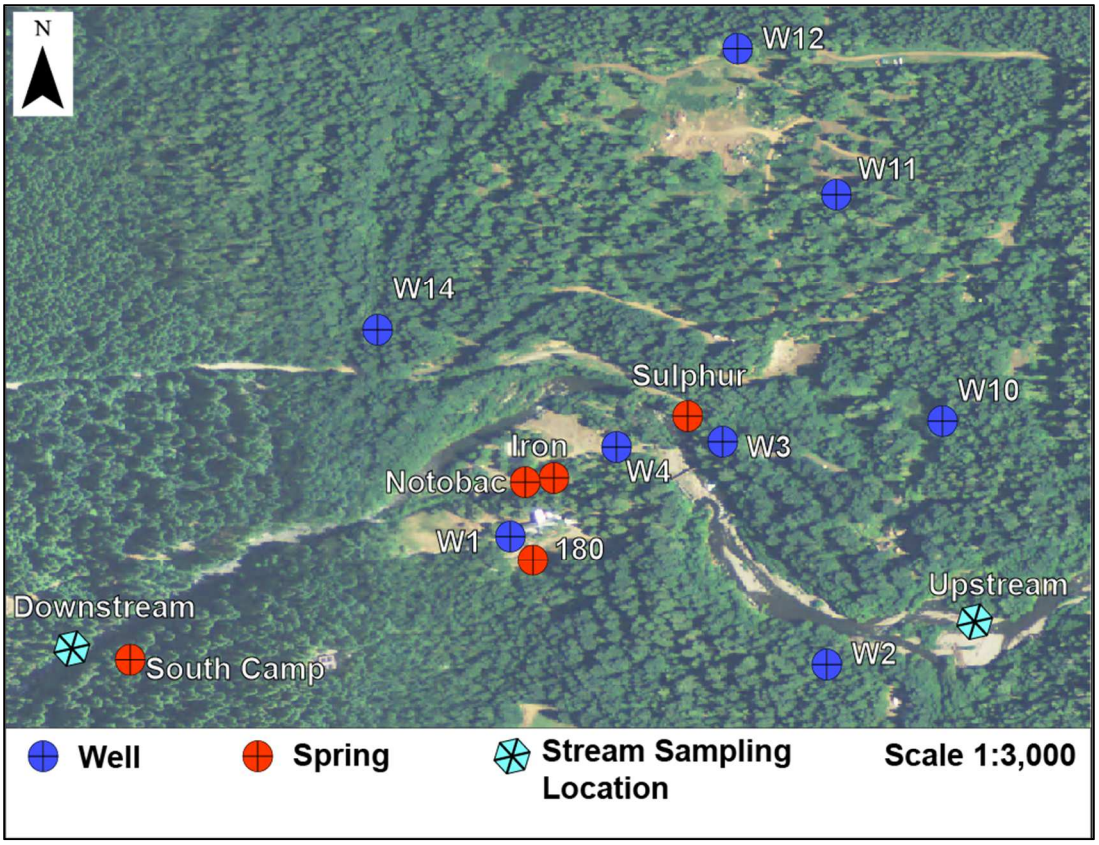

Figure 10: Breitenbush well and spring locations.

Table 1: List of wells at Breitenbush Hot Springs Resort					
Well	Depth (m)	Outflow Temperature (°C)	Max Temperature (°C)	Approximate Artesian Flow rate (l/s)	Use
W1	151	86	110[a]	2.5[b]	District Heating, filling soaking pools
W2	91	18	37[b]	-	Unused
W3	310	71	90[a]	0.13[b]	Filling soaking pools
W4	221	74	107[b]	3.8[b]	District Heating, filling soaking pools
W10	610-700[d]	82	86[c]	18[e]	Filling soaking pools
W11	443	17	39[b]	-	Unused
W12	84	16	16	-	Unused
W14	610	30	81[c]	0.06[e]	Unused

a: Blackwell and Baker, 1988

b: OWRD well logs, a "-" indicates nonartesian flow.

c: Waibel, 1983

d: Recorded depth is 610 m. According to Breitenbush staff, it may have been deepened to 710m.

e: Measured flow rates

Characterization of alteration mineralogy present in the geothermal wells and in rocks exposed at the surface in the Breitenbush area showed higher temperature alteration at the center of the Breitenbush anticline and at depth in the SUNDECO well when

compared to the flanks of the anticline or in shallower portions of the well (Keith, 1988). The fact that shallower exposures of the oldest rock share alteration mineralogy with deeper rocks of the same age implies that the highest temperature alteration occurred prior to folding (i.e. before 18 to 12 Ma) (Keith, 1988). Shallower alteration mineralogy is limited to the zeolite-facies, with lower temperature zeolite-facies assemblages present at and near surface (Keith, 1988). Table 2 lists minerals identified in boreholes in the Breitenbush area. Figure 11 shows the relative distribution of minerals in the SUNEDCO well with depth. These mineral assemblages are used as reference for application of multi-component geothermometry.

Table 2: A list of secondary minerals identified in borings in the Breitenbush Hot Springs area, depth of descriptions are included where reported

Mineral Name	Type	Formula	Depth (m)
CTGH-1 Borehole (Bargar, 1988)			
Calcite	Carbonate	$CaCO_3$	663-675
Goethite	Iron oxide	FeO(OH)	1456
Hematite	Iron oxide	Fe_2O_3	0-885
Adularia	K-Feldspar	$KAlSi_3O_8$	1293
Native Copper	Metal	Cu	1015
Celadonite	Mica	$K(Mg,Fe^{2+})(Fe^{3+},Al)[Si_4O_{10}](OH)_2$	1133-1463
Apatite	Phosphate	$Ca_{10}(PO_4)_6(OH)_2$, $Ca_{10}(PO_4)_6(F)_2$ and $Ca_{10}(PO_4)_6(Cl)_2$	665
Chalcedony	Silica	SiO_2	950-1463
Quartz	Silica	SiO_2	950-1463
α-Cristobalite	Silica	SiO_2	956-1372
β-Cristobalite	Silica	SiO_2	956-1372
Montmorillonite	Smectite	$(Na,Ca)_{0.33}(Al,Mg)_2(Si_4O_{10})(OH)_2{\cdot}nH_2O$	0-1463
Nontronite	Smectite	$(CaO_{0.5},Na)_{0.3}Fe^{3+}{}_2(Si,Al)_4O_{10}(OH)_2{\cdot}\ nH_2O$	0-1463
Saponite	Smectite	$Ca_{0.25}(Mg,Fe)_3((Si,Al)_4O_{10})(OH)_2{\cdot}n(H_2O)$	0-1463
Ilmenite	Titanium-iron oxide	$FeTiO_3$	440
Analcime	Zeolite-feldspathoid	$NaAlSi_2O_6{\cdot}H_2O$	0-885
Chabazite	Zeolite	$(Ca,Na_2,K_2,Mg)Al_2Si_4O_{12}{\cdot}6H_2O$	0-885
Clinoptilolite	Zeolite	$(Na,K,Ca)_{2\text{-}3}Al_3(Al,Si)_2Si_{13}O_{36}{\cdot}12H_2O$	885-1463
Erionite	Zeolite	$(Na_2,K_2,Ca)_2Al_4Si_{14}O_{36}{\cdot}15H_2O$	900
Heulandite	Zeolite	$(Ca,Na,K)_{2\text{-}3}Al_3(Al,Si)_2Si_{13}O_{36}{\cdot}12H_2O$	885-1463
Mordenite	Zeolite	$(Ca,Na_2,\ K_2)Al_2Si_{10}O_{24}{\cdot}7H_2O$	1099-1463
Phillipsite	Zeolite	$(Ca,Na_2,K_2)_3Al_6Si_{10}O_{32}{\cdot}12H_2O$	811-821
Scolecite	Zeolite	$CaAl_2Si_3O_{10}{\cdot}3H_2O$	750-800
Thomsonite	Zeolite	$NaCa_2Al_5Si_5O_{20}{\cdot}6H_2O$	663-812
Wellsite	Zeolite	(Ba,Ca,K2)Al2Si6O16 · 6H2O	564
Breitenbush Resort W10 (Waibel, 1983)			
Calcite	Carbonate	$CaCO_3$	
Anhydrite	Sulfate	$CaSO_4$	
Heulandite	Zeolite	$(Ca,Na,K)_{2\text{-}3}Al_3(Al,Si)_2Si_{13}O_{36}{\cdot}12H_2O$	

Table 2 (Continued)

Mineral Name	Type	Formula	Depth (m)
SUNEDCO WELL (Bargar, 1994)			
Calcite	Carbonate	$CaCO_3$	200-2457
Siderite	Carbonate	$FeCO_3$	244-2280
Chlorite-undifferentiated	Chlorite	$(Mg,Fe)_3(Si,Al)_4O_{10}(OH)_2 \cdot (Mg,Fe)_3(OH)_6$	1417-2286
Corrensite	Chlorite-smectite	$Ca_{0.6}Na_{0.2}K_{0.2}Mg_5Fe^{2+}{}_3AlSi_6Al_2O_{20}(OH)_{10} \cdot 9(H_2O)$	1800-1950
Epidote	Epidote	$Ca_2Al_2(Fe^{3+};Al)(SiO_4)(Si_2O_7)O(OH)$	600-1800
Illite	Illite	$(K,H_3O)(Al,Mg,Fe)_2(Si,Al)_4O_{10}[(OH)_2,(H_2O)]$	1426-2457
Hematite	Iron oxide	Fe_2O_3	400-2300
Magnetite	Iron oxide	Fe_2O_3	719, 1381
Kaolinite	Kaolinite	$Al_2Si_2O_5(OH)_4$	274-747
Celadonite	Mica	$K(Mg,Fe^{2+})(Fe^{3+},Al)[Si_4O_{10}](OH)_2$	777-1521
Sepiolite	Sepiolite	$Mg_4Si_6O_{15}(OH)_2 \cdot 6H_2O$	1762-1780
Chalcedony	Silica	SiO_2	200-2457
Cristobalite	Silica	SiO_2	802
Quartz	Silica	SiO_2	370-2200
Smectite-undifferentiated	Smectite	Undifferentiated, see CTGH-1	0-1920
Anhydrite	Sulfate	$CaSO_4$	1792-1920
Chalcopyrite	Sulfide	$CuFeS_2$	933
Pyrite	Sulfide	FeS_2	100-2457
Analcime	Zeolite	$NaAlSi_2O_6 \cdot H_2O$	716-780
Epistilbite	Zeolite	CaAl2Si6O16•5(H2O)	1411
Heulandite	Zeolite	$(Ca,Na,K)_{2-3}Al_3(Al,Si)_2Si_{13}O_{36} \cdot 12H_2O$	500-1700
Laumontite	Zeolite	$Ca(AlSi_2O_6)_2 \cdot 4H_2O$	765-1981
Mordenite	Zeolite	$(Ca,Na_2,K_2)Al_2Si_{10}O_{24} \cdot 7H_2O$	518-579
Scolecite	Zeolite	$CaAl_2Si_3O_{10} \cdot 3H_2O$	1280-1290
Stellerite	Zeolite	$Ca_4(Si_{28}Al_8)O_{72} \cdot 28(H_2O)$	844-1454
Stillbite/Stellerite	Zeolite	$NaCa_4(Si_{27}Al_9)O_{72} \cdot 28(H_2O)$	844-1454

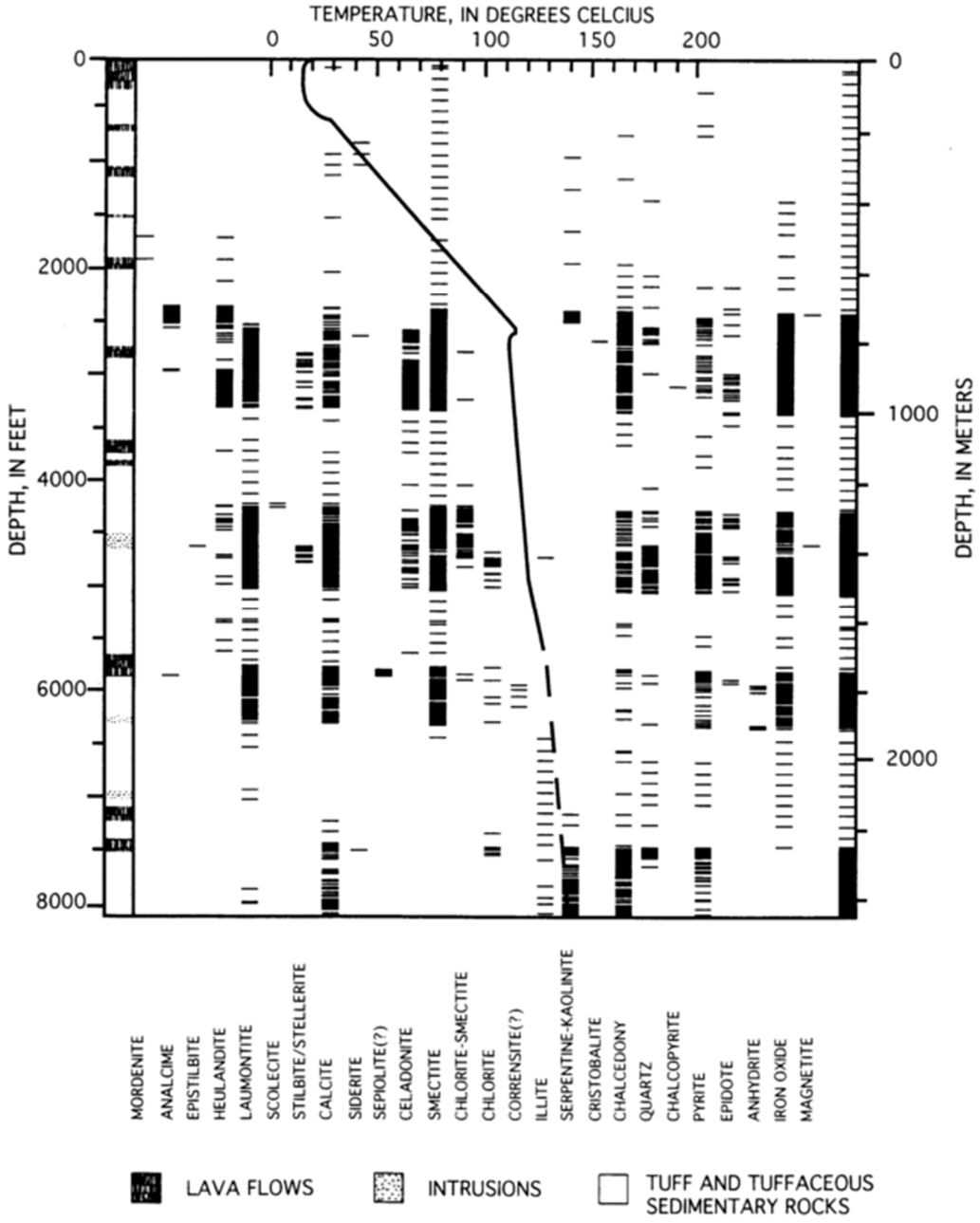

Figure 11: Distribution of hydrothermal minerals with depth in the SUNEDCO well. Left column shows the stratigraphic section of rock units encountered. A temperature with depth curve is superimposed on the graph, from Bargar, 1994.

Heat flow data collected from temperature-gradient wells in the Breitenbush area show an extension of high heat flow from the Cascade crest to the west at the location of Breitenbush Hot Springs (Blackwell and Baker, 1988). The high temperature aquifer associated with this heat flow anomaly was present at a depth of 800 m in the SUNEDCO well at a temperature of approximately 116°C. Below this depth, the temperature gradient data suggest conductive heat flow to a maximum approximate borehole temperature of 141°C at the bottom of the hole (2,457 m) (Blackwell and Baker, 1988). The maximum recorded borehole temperature of a well installed at the Breitenbush Hot Springs Resort is 116°C recorded in W3 (Figure 10; Blackwell and Baker, 1988). Current surface well temperatures are as high as 85°C (Table 1). Based on the apparent depth of the thermal aquifer and its relationship to local geologic structures, it was posited that the source of the heat was derived from igneous processes beneath the Cascade crest (i.e. near Mount Jefferson). Permeability contrasts between a highly altered zone of the Breitenbush Tuff and the overlying HCG allow movement of thermal water from the east to the west along the Breitenbush anticline, thus producing the observed high heat flow anomaly to the west of the Cascade crest, and providing a theoretical framework for the hot springs (Sherrod and Conrey, 1988). Excess N_2/Ar ratio in total gas from Oregon Cascade Range hot springs, including Breitenbush, correlate with excess calcium and dissolved chloride concentrations, suggesting that nitrogen in the system is derived from water-rock interaction (Mariner et al., 2003). In addition, total nitrogen correlates with estimated aquifer temperature in a curve that shows similarity to the observed relationship in oil

field brines, suggesting a possible sedimentary source for nitrogen and chloride (Mariner et al., 2003). Helium isotope ratios suggest that Breitenbush is fed from a magmatic source; the coupling of a widespread sedimentary basement beneath the Cascades with a source of magmatic volatilization suggests a local High Cascade origin of the thermal signature at Breitenbush (Mariner et al., 2003). This scenario is in contrast to a previously hypothesized larger scale zone of crustal weakness (Blackwell and Baker, 1988).

Several estimates of reservoir temperature have been made by various chemical geothermometers. An estimated reservoir temperature of 174°C based on silica geothermometers was derived in 1982 as part of a large-scale study across the Cascades (Forcella, 1982). A second estimate of 174°C was derived from forced equilibrium with anhydrite (Ingebritsen et al., 1992). A summary of classical geothermometers, including a sulfate isotope geothermometer, resulted in estimates from 129 to 202 °C (Mariner et al., 1993). Multi-component geothermometers produced estimates of 180°C (Pang and Reed, 1998) and 176°C (Spycher et al., 2016). In both cases, Al concentrations were derived by forced equilibrium with microcline. These temperatures were considered reasonable when compared to the anhydrite equilibrium and sulfate isotope data of Mariner et al. (1993). An estimated temperature of 177°C was used in determination of the sedimentary source of Cascade geothermal waters discussed above (Mariner et al., 2003).

In addition to these reservoir estimates using geothermometers, an analysis of fluid inclusions found in the SUNEDCO and CTGH-1 boreholes determined

temperatures ranging from 113 to 232 °C (Bargar, 1994). The majority of fluid inclusion temperatures, particularly those from secondary calcite and anhydrite minerals, were coincident with measured bore-hole temperatures at the sample depth, suggesting that they had formed in equilibrium with the current geothermal system. Fluid inclusions found in hydrothermal quartz and primary quartz phenocrysts generally showed temperatures greater than the measured borehole temperature at the associated depth (Bargar, 1994).

2.2.2 Wind River

The Wind River Valley trends northwest from the Columbia River at the town of Carson, approximately 50 kilometers northeast of Portland (Figure 7). Several thermal springs are present close to its intersection with the Columbia River. Due primarily to its potentially steep geothermal gradients and proximity to power transmission lines, a GIS-based analysis of geothermal favorability in Washington determined that the Wind River Valley is one of the most promising areas for geothermal energy development in the state (Boschmann, et al., 2014). The following sections summarize the geology of the Wind River Valley and past geothermal resource characterization that has been conducted in the area.

2.2.2.1 Geology

The oldest stratigraphic unit outcropping in the Wind River Valley is the late Eocene to early Oligocene Ohanapecosh Formation, part of the WCG (Figure 12; Hammond, 1979). The unit is thought to represent early volcanism in the Cascade arc and consists of dacitic and andesitic volcaniclastic deposits in the Wind River Valley (Jutzeler, 2013). Based on geochemical and stratigraphic similarity between these deposits and Ohanapecosh Formation further north, which consists of lava flows and breccias, the Wind River Valley Ohanapecosh may represent the depositional products of distal volcanism (Berri and Korosec, 1983). The Ohanapecosh Formation has a high degree of mineral alteration, including groundmass alteration to yellow-green clays and chlorite that provides a green hue to its deposits. This alteration may be associated with Miocene-age folding (around the same time as that experienced at Breitenbush) which could have provided a regional low-grade metamorphic signature (Berri and Korosec, 1983).

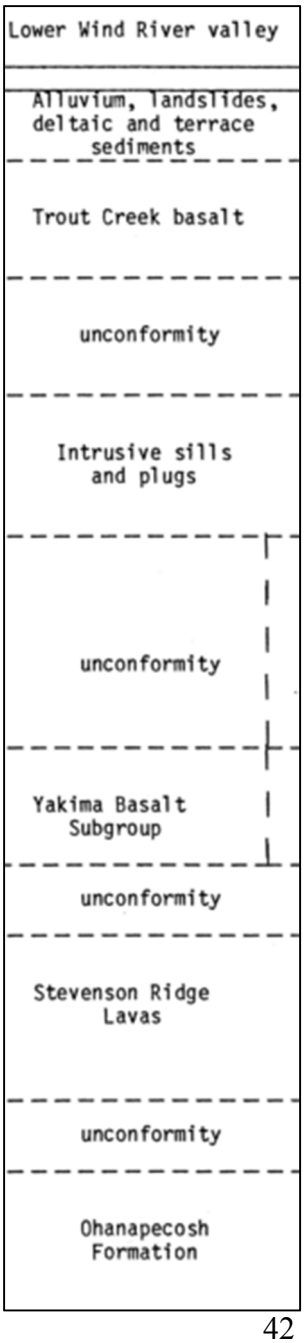

Figure 12: Stratigraphic column of rocks in the Wind River Valley. From Berri, and Korosec, 1983

Unconformably overlying the Ohanapecosh Formation in the Wind River Valley are the late Oligocene to early Miocene Stevenson Ridge Lavas, which consist of pyroxene-rich basalt and basaltic-andesite flows (Berri and Korosec, 1983). These flows outcrop at the crest of Stevenson Ridge, which forms the western border of the Wind River Valley, and may represent inverted topography of a valley carved by the ancestral Wind River (Berri and Korosec, 1983). Overlying the Ohanapecosh to the east and southeast of the Wind River Valley is the Grand Ronde Basalt of the Columbia River Basalt Group (Berri and Korosec, 1983). Several intrusive plugs and sills outcrop in the Wind River valley. Wind Mountain is a quartz diorite intrusion near the confluence of Wind River with the Columbia that apparently intruded the Grand Ronde Basalt (Berri and Korosec, 1983). The Buck Mountain Intrusion is a diorite intrusion that outcrops at the Wind River near the hot springs and makes up the steep eastern flank of the Wind River Valley in this area. Age ranges for the intrusions are between 14 and 23 Ma (Berri and Korosec, 1983). The most recent volcanic deposits in the Wind River Valley are those associated with the Trout Creek Hill Volcano, located approximately 18 kilometers northwest of the hot springs. A succession of basalt flows of the Trout Creek Hill Volcano appears to have followed the topography of the Wind River Valley. K-Ar dating of the flows resulted in an estimated age of 340 Ka for Trout Creek Volcano (Berri and Korosec, 1983).

The linearity of the Wind River Valley, coupled with the consistent northwest orientation of past lava flows and intrusions, suggests a long-existing structural feature,

such as a homocline or a fault (Berri and Korosec, 1983). A northeast-trending fault designated the little River Fault is mapped close to the intersection of Wind River and the Columbia River.

2.2.2.2 Geothermal Exploration

Three geothermal exploration borings were drilled in the 1980s, two to a depth of 152 meters, and a third to a depth of 357 meters. One of the 152 meter deep borings and the 357 meter boring were located in the western flank of the center of the valley and showed geothermal gradients of 75 and 79 °C/km, respectively (Figure 13). The second 152 meter boring was drilled close to St. Martin's Hot Spring and showed a gradient of 160 °C/km (extrapolated from a bottom hole temperature of 28°C). In 2012, the Washington Department of National Resources (DNR) drilled an 88 meter boring in the northwestern portion of the valley that had a gradient of 55.9 °C/km. No boreholes deeper than 357 meters have been drilled in the valley. In 2012, the DNR conducted 20 ground based magnetic anomaly transects and 4 electrical resistivity transects at various locations in the valley. These techniques support the existence of faults in the southeastern portion of the valley, the intersection of which may create a conduit that could explain the presence of the hot springs in this area (Czajkowski et al., 2013). The recent work was associated with the United State Department of Energy (DOE) national Play Fairway analysis. Based on these initial results, Washington State was one of five areas selected for Phase II of the Play Fairway project (Garchar et al., 2016) .

At least six springs are present in the valley (Figure 13) with temperatures ranging from 8 to 50°C, following a trend of lower temperatures to the northwest and higher temperatures to the southeast (Czajkowski, 2013). Sporadic water sampling data is available for nine named springs in and in close proximity to the valley between 1977 and 2013. The springs of the Wind River Valley have been divided into three categories based on their temperature and composition (Czajkowski et al., 2013). Group A springs are considered to be fault-related, and occur close to the Brush Creek Fault and the Wind River Fault, by the confluence of the Wind River and the Columbia River (Figure 14). Both St. Martin's Hot Spring and Shipherd's Hot Spring are assigned Group A. Reservoir temperatures at St Martin's Hot Spring and Shipherd's Hot Spring were developed from the classical geothermometers tabulated on the spreadsheet of Powell et al., 2010. Estimates for St Martin's Hot Spring were 65°C using a NA-K-Ca geothermometer and 73°C using a chalcedony geothermometer (Czajkowski et al., 2014). Shipherd's Hot Spring yeilded a reservoir temperature of 19°C using a Na-K-Ca geothermometer. Group B springs are high TDS springs at the northwestern end of the linear portion of the Wind River Valley. Group C springs are cold seeps that are likely sourced from local, cool recharge waters (Czajkowski et al., 2013). Group B and C springs were not evaluated for this thesis.

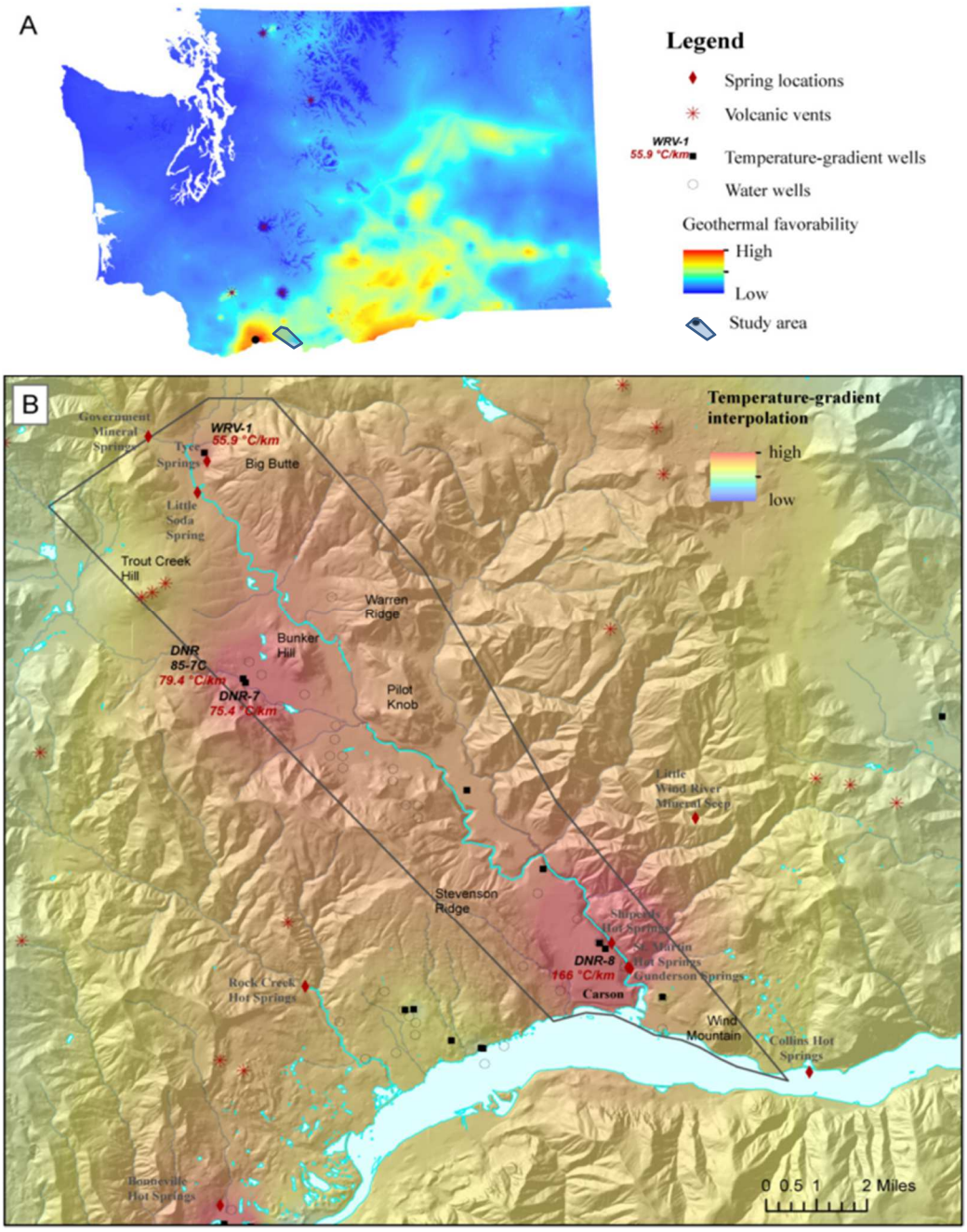

Figure 13: a) Geothermal favorability map for Washington State. B) A map of the Wind River Valley showing thermal gradient borings, and geothermal indicators, from Czajkowski, 2013.

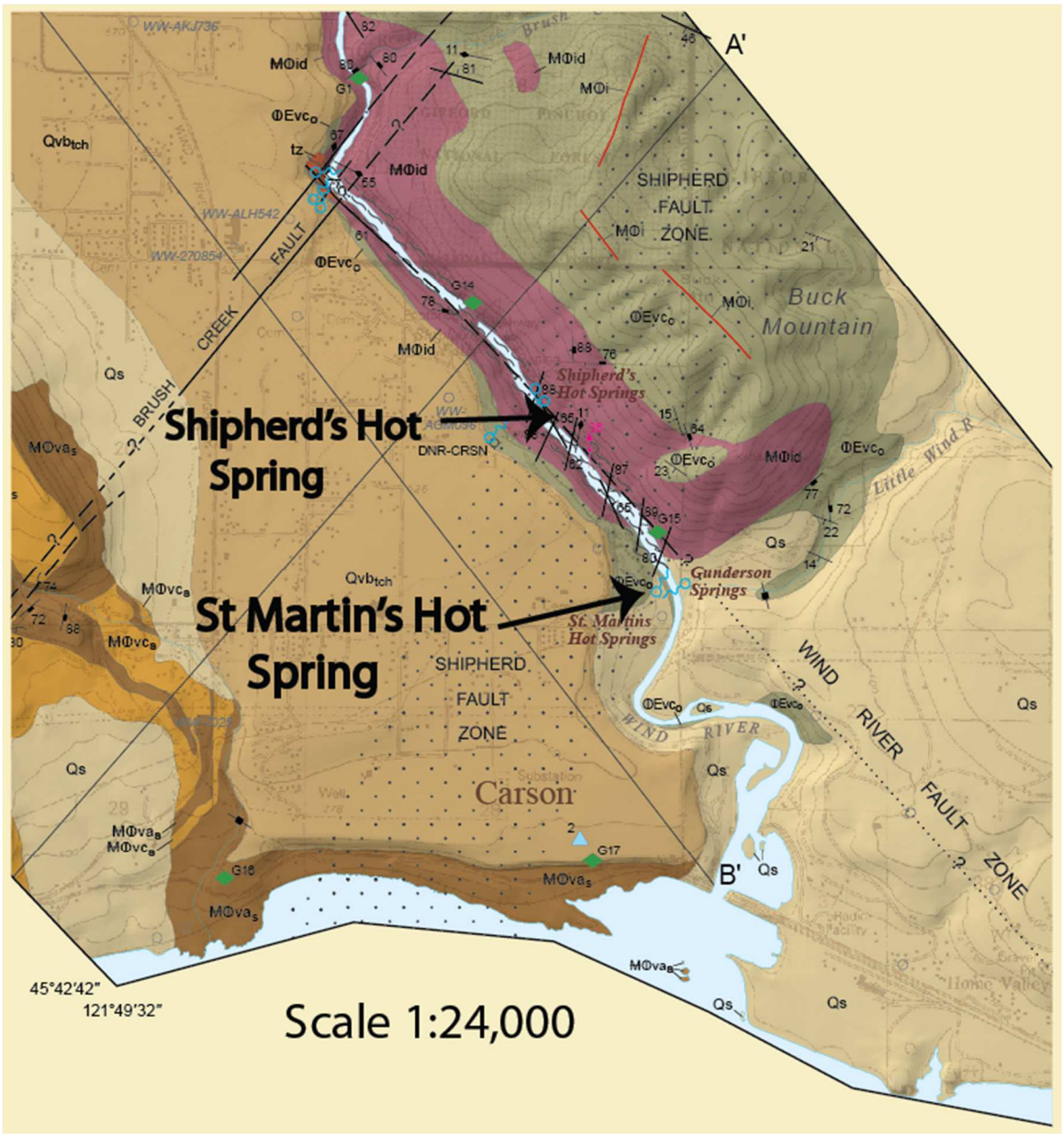

Figure 14: Wind River Valley showing sampled Hot Springs and fault traces. Note that Shipherd's Hot Spring encompasses multiple seeps on the northeast side of the Wind River, from Czajkowski et al., 2013.

3 METHODS

3.1 Field Methods

A total of 13 well samples, 5 spring samples, and 2 river samples were collected from Breitenbush Hot Springs (Fig. 10) and 4 spring samples were collected from the Wind River Valley (Fig 14) for chemical analysis. Sample locations (Table 3) were determined in the field using a handheld GPS unit.

Samples were collected in five separate campaigns (four at Breitenbush and one at Wind River) at different times of the year in differing weather conditions. Samples from Breitenbush wells W10, W12, and W14 were collected on October 7, 2014, prior to significant rainfall in water year 2014-2015. Samples from Breitenbush wells W1, W3, and W4 and 180°, Iron, No Tobacco, and Sulphur Springs, were collected on November 19, 2014 following a period of significant precipitation and while several feet of snow blanketed the area. Samples from Breitenbush wells W2 and W11 were collected on February 21, 2015, on a sunny day after several days of rainfall. Samples from the W10-time series, South Camp Springs, and the Breitenbush River were collected on June 30, 2015, a dry day weeks after the spring freshet. Samples collected from Wind River's St. Martin's and Shipherd's Hot Springs were collected on November 16, 2015, immediately following several days of heavy rainfall.

Table 3: Sampling locations and coordinates		
Sample Location	Lat.	Long.
Breitenbush Wells		
W1	44.78131	-121.9762
W2	44.77999	-121.9721
W3	44.78214	-121.9734
W4	44.78211	-121.9749
W10	44.78233	-121.9708
W11	44.78425	-121.9712
W12	44.78544	-121.9737
W14	44.78322	-121.9786
Breitenbush Springs		
180°	44.78116	-121.9762
Iron	44.78172	-121.9763
No Tobacco	44.78171	-121.97630
Sulphur	44.78231	-121.9739
South Camp	44.78098	-121.9796
Breitenbush Stream Sampling Locations		
Upstream	44.78045	-121.9715
Downstream	44.78099	-121.9802
Wind River Sampling Locations		
St. Martin's #1	45.72917	-121.798
St. Martin's #2	45.72881	-121.7962
Shipherd's #1	45.73475	-121.8024
Shipherd's #2	45.73420	-121.8021

Spring waters found as pools (180° Spring, South Camp Spring, Shipherd's #1) were collected by first observing any bubbles emerging from cracks on the pool bottom to identify the likely point of spring discharge. A Teflon beaker attached to a telescoping

polyvinylchloride rod was then placed close to the point of likely discharge and inverted for sample collection. For flowing springs (Iron Spring, No Tobacco Spring, Sulphur Spring, Shipherd's #2), sample bottles were placed directly into the flow path.

Wells W1, W3, and W4 provide water for district heating and/or filling of soaking pools at the Breitenbush Hot Springs Resort. To sample these wells, a fire hose was attached to a discharge outlet and the wells were allowed to purge for at least one well volume prior to sample collection via a hose attached to a sample port at or near the wellhead. Wells at Breitenbush Hot Springs are completed as uncased holes in bedrock without filter pack (boring logs, Appendix A). When the wellhead is opened, well W10 flows under artesian conditions at approximately 19 l/s. A total of six samples were collected from this well at intervals of ~20 to 60 minutes and increasing temperatures of 62, 64, 72, 77.5, 79.5, and 82 °C to identify any changes in water chemistry with additional purging and differing sample temperature. Samples were collected from tubing at a point approximately 7 meters from the wellhead. W14 flows constantly at a rate of approximately 0.06 l/s from the top of the wellhead. Samples were collected directly from the flowing water without purging. Water levels in wells W2, W11, and W12 are below the well casing and thus had to be pumped to the surface. The water level in W12 was high enough in the casing to sampling using a peristaltic pump. The low-flow nature of the pump allowed the use of a flow-through cell, which was constantly monitored until parameters stabilized before sample collection. The water levels in W2 and W11 were too deep for the use of a peristaltic pump. Well W2 was purged for three well volumes and

then sampled through tubing attached to an aboveground Toyota water pump. Well W11 was purged for approximately one well volume using a submersible pump attached to a 2.5 cm hose.

According to the owner of Carson Hot Spring Resort, St. Martin's Hot Spring flows under artesian conditions into a natural pool located near the river (Cam, 2015). This water is then pumped from the pool to the resort where it provides sufficient hot water to fill all of the resort's baths, which include a large swimming pool. Two samples were collected from this spring. The first was collected from a tap at the resort itself after allowing 45 minutes of flow, the second was collected from a sample port at the well house by the river. The spring pool itself was inaccessible due to a concrete and plywood covering.

At each sample location, measurements of temperature, specific conductance, electrical conductivity, oxidation-reduction potential (ORP), pH, and dissolved oxygen content were made using a calibrated YSI multimeter. For well samples, water was pumped via a hose into a YSI flow-through cell in which readings were collected. For waters in excess of 40°C, the water was first sent through a heat exchanger constructed of coiled stainless steel tubing surrounded by ice in a cooler in order to cool the water to temperatures appropriate for use with the YSI meter. For spring samples, either the probe was inserted directly into the spring or, for spring waters exceeding 40°C, readings were collected in filled containers which had been allowed to cool. ORP measurements were

made with a combination platinum electrode with a Ag/AgCl (4M KCl) reference electrode calibrated using ZOBELL solution. pH was calibrated in the field immediately prior to sampling using pH 4, 7, and 10 buffer standards. Alkalinity was determined in the field using a HACH digital titrator equipped with either a 0.160 or 1.600 N H_2SO_4 cartridge and bromcresol green-methyl red to indicate the total alkalinity endpoint. Two alkalinity measurements were made at each location and the average of the two was tabulated. No field alkalinity data was collected for the Wind River samples due to an oversight in field preparation. Samples for ion analyses were filtered through a 0.45 μm polyethersulfone membrane syringe filter and collected into acid washed, low-density polyethylene bottles. Samples retained for cation analysis were acidified in the field to < pH 2 using trace-metal grade HNO_3. Samples for anion, isotope and laboratory pH and alkalinity analyses were filled with every effort to eliminate air bubbles in the headspace. All samples were transported to the laboratory in an ice-filled cooler.

3.2 Laboratory Methods

Total alkalinity was measured at Portland State within 48-hours of sample collection by titrating 0.05 N HCl into 50 ml of sample while recording pH values every 0.1 ml until reaching a pH well below the HCO_3^- inflection point. Once sufficient data was recorded, the alkalinity value was calculated using the Gran Function (Gran, 1952). Alkalinities are reported as milligrams per liter (mg/L) of $CaCO_3$ and HCO_3^-. Samples were analyzed for major anions (Cl, F, Br, PO_3^- NO_3^-, and N^-) using high performance liquid chromatography (HPLC) on an LC25 Dionex chromatography unit equipped with a Dionex CD25 conductivity detector, a GP50 gradient pump, and an As40 automated sampler. The carrier fluid consisted of 4.5 millimollar (mM) Na_2CO_3 and 0.8 mM $NaHCO_3$. Concentrations were determined using conductivity measurements relative to the conductivity of known standards from 0.1 to 200 ppm prepared from commercial, NIST-traceable stock solutions. Large dilutions of split samples were necessary to accommodate the high chloride contents of some water samples.

Samples were analyzed for select major, minor, and trace cations using an Agilent 700 Series axial ICP-OES equipped with an Agilent SPS3 auto-sampler, a glass concentric nebulizer, a glass cyclonic spray chamber, and a low-flow quartz torch with 1.4 mm id injector tube. Operating conditions are provided in Appendix B. Calibration was performed using up to 15 external calibration standards prepared from commercial NIST-traceable stock standards.

Although silica was analyzed via ICP-OES, silica concentrations were also evaluated for select samples using a Beckman Coulter DU 730 UV/Vis Spectrophotometer. Samples were prepared using sodium molybdenate solution and nitric acid. Frequency was read at 410 nm to determine concentration.

Samples were also submitted to the Northern Arizona University Stable Isotope Laboratory for analysis of deuterium and stable oxygen isotopes (i.e. ^{18}O and ^{16}O) using a LGR Liquid Water Isotope Analyzer DLT-100.

3.3 Geothermometry Methods

3.3.1 Classical Geothermometers

Table 4 lists classical geothermometers used for this study. These were selected based on their continued use in the geothermal industry and/or their supposed effectiveness. The methods used to generate the estimates are described in the paper that is listed under the reference column with the exception of the Giggenbach Diagram, which was produced using the procedure outlined in Arnórsson, 2000. Equations for the majority of the geothermometers are presented in Section 2.1.1.

Table 4: Classical geothermometers used for temperature estimate comparison, reference key refers to the label used in figures

Equilibrium Mineral or Ion Ratio	Reference Key	Reference
Chalcedony	F77	Fournier, 1977
α-Crisobalite	F77	Fournier, 1977
β-Crisobalite	F77	Fournier, 1977
Amorphous Silica	F77	Fournier, 1977
Na-K-Ca	FT73-79	Fournier and Truesdell, 1973
Na/Li	FM81	Fouillac and Michard, 1981
Quartz	FP82	Fournier and Potter, 1982
Na/K	VS97	Verma and Santoyo, 1997
Na/Li	VS97	Verma and Santoyo, 1997
SiO2	VS97	Verma and Santoyo, 1997
SiO2	A98	Arnórsson, 1998
Na/K	C02	Can, 2002
Na/K	D08	Diaz et al., 2008
Na/K 2	D08	Diaz et al., 2008
Na/K 3	D08	Diaz et al., 2008
Na-K-Ca-Mg Ternary diagram	G88	Giggenbach, 1988

3.3.2 GeoT

Several inputs were tested in the use of GeoT. The database used for GeoT was SOLTHERM, which is a database for geothermal applications developed and maintained by the University of Oregon (Reed and Palandri, 2006). The following list describes the

variation in inputs used with applicable subheadings. GeoT input files are included in Appendix C.

- Mineral selection
    - Allowing GeoT to generate a mineral selection with no user input.
    - Using a "free-silica" mineral such as quartz and chalcedony, and allowing GeoT to estimate nearby minerals based on these equilibrium temperatures.
    - Adjusting the automated mineral assemblage based on secondary minerals reported in boreholes (Table 2).
- Input options
    - Estimating reservoir temperature for each sample location independently.
    - Estimating reservoir temperature using all applicable water chemistries simultaneously.
- Optimization using PEST on the following parameters:
    - Optimization of steam weight fraction, which indicates the extent that fluid has lost species due to subsurface degassing. The re-mixed gas concentration was based on free gas concentrations measured at Breitenbush (Mariner et al., 2003). The reported gas concentration included noble gas elements; however, these components not included due to their conservative nature. Instead,

the concentrations reflect the relative proportions of the non-ideal gas constituents.

- Optimization for adjustment of the initiation temperature, which describes the temperature at which the equilibrium chemistry of forced components is determined. The initiation temperature parameter adjusts the initial speciation of H+ ions and any species that are constrained by equilibrium with a mineral.
- Optimization of "concentration," which adds (if less than 1) or removes (if greater than 1) pure water components from the water chemistry, thus representing mixing with pure water, or removal of H_2O dominant steam.
- Optimization using the built in mixing model, which is similar to the concentration parameter, but uses user-defined water as opposed to pure water. The mixing extent parameter allows the mixing or "unmixing" of thermal water with shallower water. For this study, the water chemistry of W12 was used as the shallow water.
- Parameters for each of the basis specie activities were allowed to adjust depending on the analytical uncertainty associated with the species. For example, a 5% analytical error would allow the

associated component to vary over a range of ±5% compared to the reported value.

3.3.3 RTEst

A variety of different inputs were used for reservoir estimation using RTEst. Several of the methods are similar to those used with GEOT; however, the programs have different input options, and as such, have distinct methods of operation. The database used for RTEst assessment was the Geochemist's Workbench database thermo.dat. Use of RTEst with SOLTHERM was also attempted, as described in Section 4.2.3.3. The following list describes the variation in inputs used with applicable subheadings.

- Mineral selection
    - Using a "free-silica" mineral such as quartz and chalcedony, and allowing RTEst and/or Geochemist's Work Bench to estimate minerals based on these equilibrium temperatures.
    - Adjusting the automated mineral assemblage based on observed minerals (Table 2).
    - Using a mineral assemblage generated using GeoT estimation processes (Section 3.3.2).
    - Mineral assemblages were developed for each water sample independently to determine consistency between individual estimates.

    - Different mineral assemblages were applied to all of the water chemistries until a single assemblage could consistently reproduce reservoir conditions at each sample location while explaining the presence of the alteration minerals observed in the nearby geothermal wells.

- Optimization
    - RTEst allows for optimization of temperature, CO_2 fugacity, change in the mass of water, and mixing amount with user-input shallow water chemistry. Optimization runs were made with all combinations of these variables.

4 RESULTS

4.1 Analytical Results

Analytical results are listed in Tables 5 (field measurements), 6 (major ion concentrations), 7 (trace element concentrations), and 8 (isotope results). Figure 15 shows a Piper diagram for the Breitenbush Hot Spring samples. With the exception of the river samples, W12, and W11, all of the Breitenbush samples plotted distinctly as Na-Cl waters. W12 plots as a Na-HCO_3^- water and W11 is somewhat in between. This separation of W11 and W12 from the others is consistent with total dissolved solids values of less than 400 for W11 and W12 compared to values greater than 2,000 for the remainder of the Breitenbush samples. These data indicate a potential shallow, more recently recharged source for W11 and W12.

W2 and W14 show similarities to the majority of the other thermal water samples collected from Breitenbush in some dissolved ion concentrations (Cl^-, F^-, SO_4^{2-}, Ca^{2+}, and Na^+) and differences in others (notably SiO_2, HCO_3^-, Mg^{2+}, K^+, As, and Mn^{2+}). The similarity in the conservative Cl^- ion in particularly suggests that the waters may have originated from a similar thermal source as the other waters. Their depletion in other ions suggests that they may have experienced more shallow mineral precipitation than other wells and springs. W2 and W14 had water temperatures of 17.6 and 29 °C during sampling,, both of which are much cooler than the other waters with a thermal signature.

These cooler temperatures could be due to relatively slower flow paths, which would provide more time for mineral precipitation between the reservoir and the surface and thus explain the difference in water chemistry. The differences between the average concentration of Mg^{2+}, K^{+}, and SiO_2 in W1, W3, W4, and the hot springs with the concentration of Mg^{2+}, K^{+}, and SiO_2 in W2 are 0.030 mmol, 1.2 mmol, and 2.1 mmol, respectively. The differences between the average concentration of Mg^{2+}, K^{+}, and SiO_2 in W1, W3, W4, and the hot springs with the concentration of Mg^{2+}, K^{+}, and SiO_2 in W14 are 0.023 mmol, 0.91 mmol, and 1.3 mmol, respectively. The ratios of these differences (W2/W14) are 0.77, 0.76, and 0.62. The consistency in these ratios suggests that there is also consistency in the minerals precipitated during ascent, with the waters in W2 having undergone more precipitation than the waters in W14.

Isotope results are reported relative to Vienna Standard Mean Ocean Water (VSMOW) in δ notation (the same equation applies to δD, with D/H replacing $^{18}O/^{16}O$):

$$\delta\ ^{18}O\ ‰ = 1000 * [(\text{Sample } ^{18}O/^{16}O - \text{VSMOW } ^{18}O/^{16}O)/ \text{VSMOW } ^{18}O/^{16}O].$$

Figure 16 shows the extent to which the samples collected for this study fall on or away from the global meteoric water line of deuterium and ^{18}O isotopes. Both W12 and W11 fall close to a local meteoric water line (LMWL) developed from samples collected in the nearby Willamette Basin (Brooks et al., 2012), further suggesting a shallow recharge source for these wells. W11 falls to the left (more depleted in both isotopes) than W12. This may be due to the fact that W11 is 359 meters deeper than W12, and may

intersect higher elevation flow paths. In general, as precipitation moves further inland and to higher elevations, it becomes progressively depleted in heavier isotopes, which prefer liquid over vapor phase compared to their lighter counterparts.

All of the other samples from Breitenbush show enrichment of ^{18}O over deuterium relative to the LMWL. A trend line drawn through these sample points is depicted on Figure 16. Figure 17 shows these samples with the trend line extrapolated to more and less isotopic enrichment. The trend line intersects the LMWL at -14 ‰ $\delta^{18}O$ and -101 ‰ δD, close to the value for W11 (-13.9 ‰ $\delta^{18}O$ and -97 ‰ δD) and indicating a similarly higher elevation meteoric water source for the thermal waters compared to locally recharged precipitation. When extrapolated towards higher enrichment, the trend line intersects the area of "andesitic water" proposed by Giggenbach (1992). Andesitic water is considered to represent subducted seawater either trapped in pores or present in hydrated clays that interacts with the upper mantle during slab descent. Based on the $\delta^{18}O$ shift along the trendline, Breitenbush waters represent 6 to 10 % andesitic waters. This mantle signature is consistent with He isotope values (Mariner, 2003). Other possible andesitic waters in the Cascade Arc were recognized by Clark and Fritz (1997) in regard to isotope data from the Meager Creek, Canada, geothermal area collected during the 1980s.

The Wind River samples isotopic data show the Shipherd's Hot Spring samples close to the meteoric water line and the St. Martin's Hot Spring samples less enriched in D, and slightly more enriched in ^{18}O. The offset of the St. Martin's Hot Spring samples

may be due to water-rock interaction, which would tend to enrich the water samples with ^{18}O relative to D. In this case, the St. Martin's Hot Spring would have a have a higher elevation meteoric water signature than the Shipherd's Hot Spring. The Shipherd's Hot Spring samples are likely a mixture of St. Martin's thermal source and low elevation precipitation. The Wind River samples are less depleted in both deuterium and ^{18}O compared to the Breitenbush samples, which suggests that the original source water is from a lower elevation or closer to the oceanic water source.

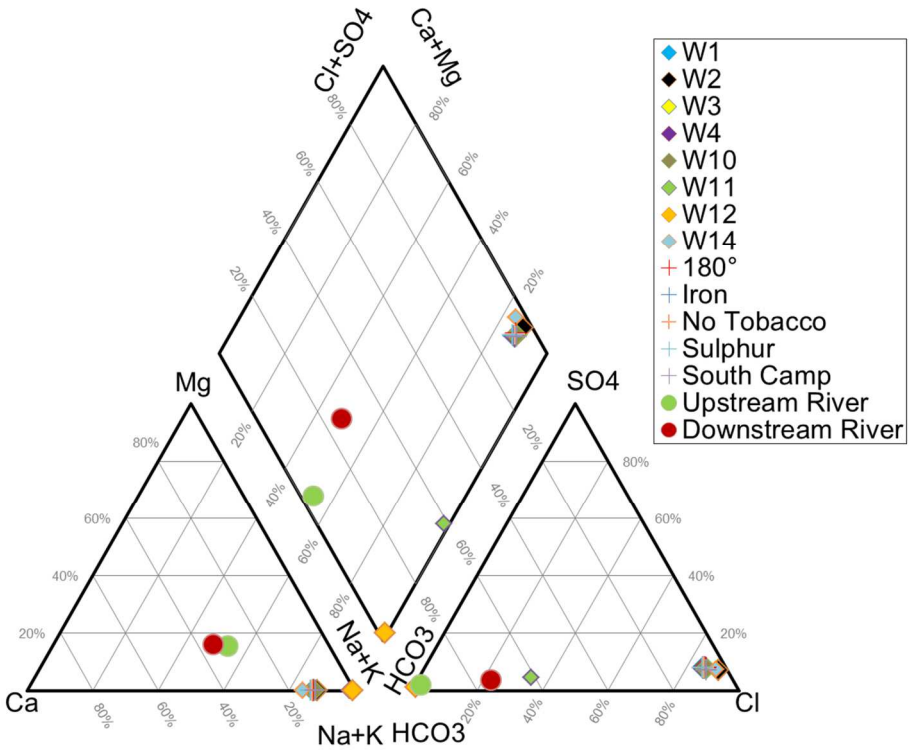

Figure 15: Piper diagram of Breitenbush samples. Note that W12 and W11 are the only non-river samples that plot outside of the Na-Cl water quadrant. The majority of the samples overprint each other near the tip of the Na-Cl quadrant. Wells are depicted with diamonds, springs are depicted with crosses, and stream samples are depicted with circles.

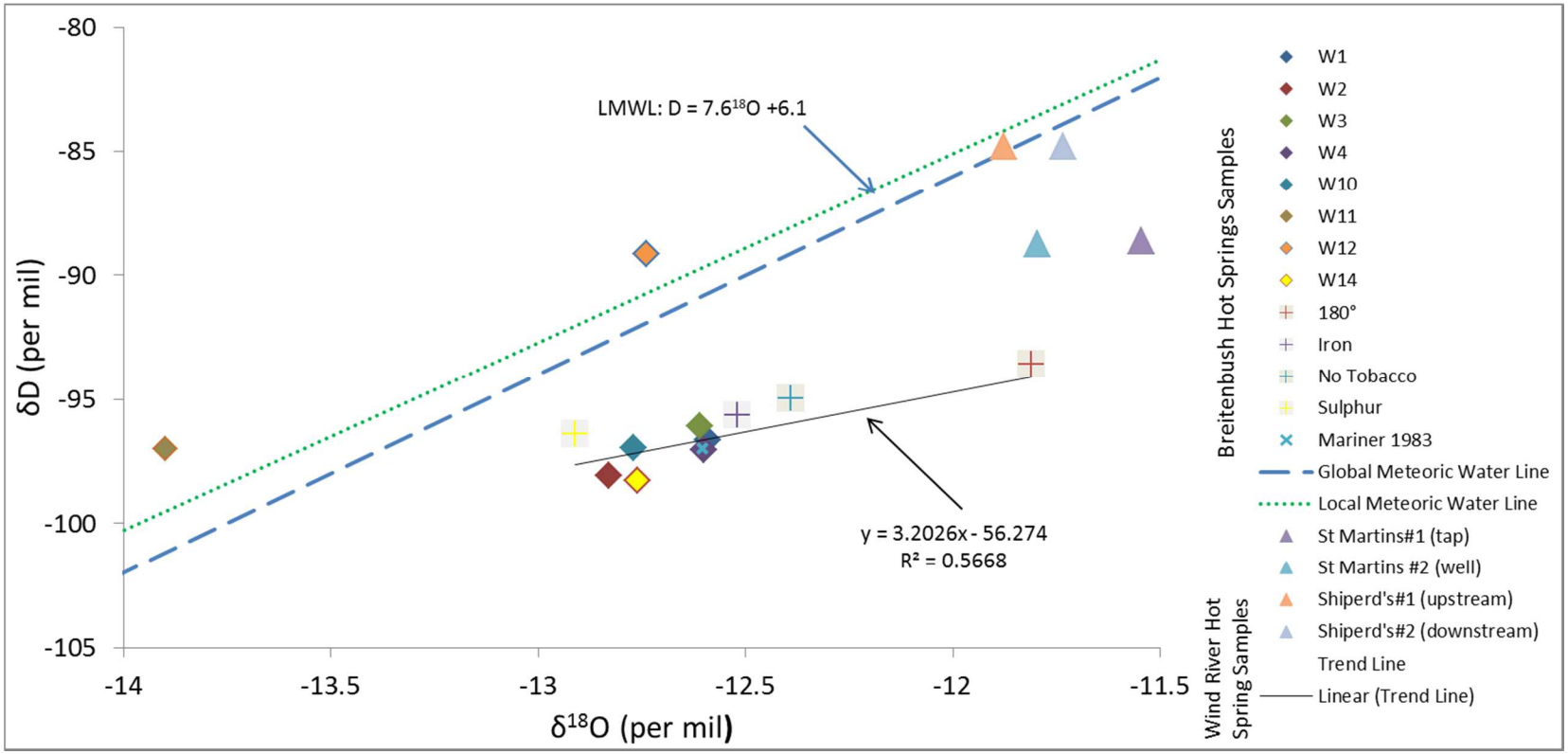

Figure 16: δD versus δ18O. The dashed blue line is the expected global meteoric water line. The dotted green line represents a local meteoric water line (Brooks et al., 2012). Breitenbush wells are depicted with diamonds, Breitenbush springs are depicted with crosses. Data from Mariner, 1983 are depicted with an x. Wind River Hot Spring samples are depicted with triangles. A line shows the trend between Breitenbush Hot Spring samples, excluding W11 and W12.

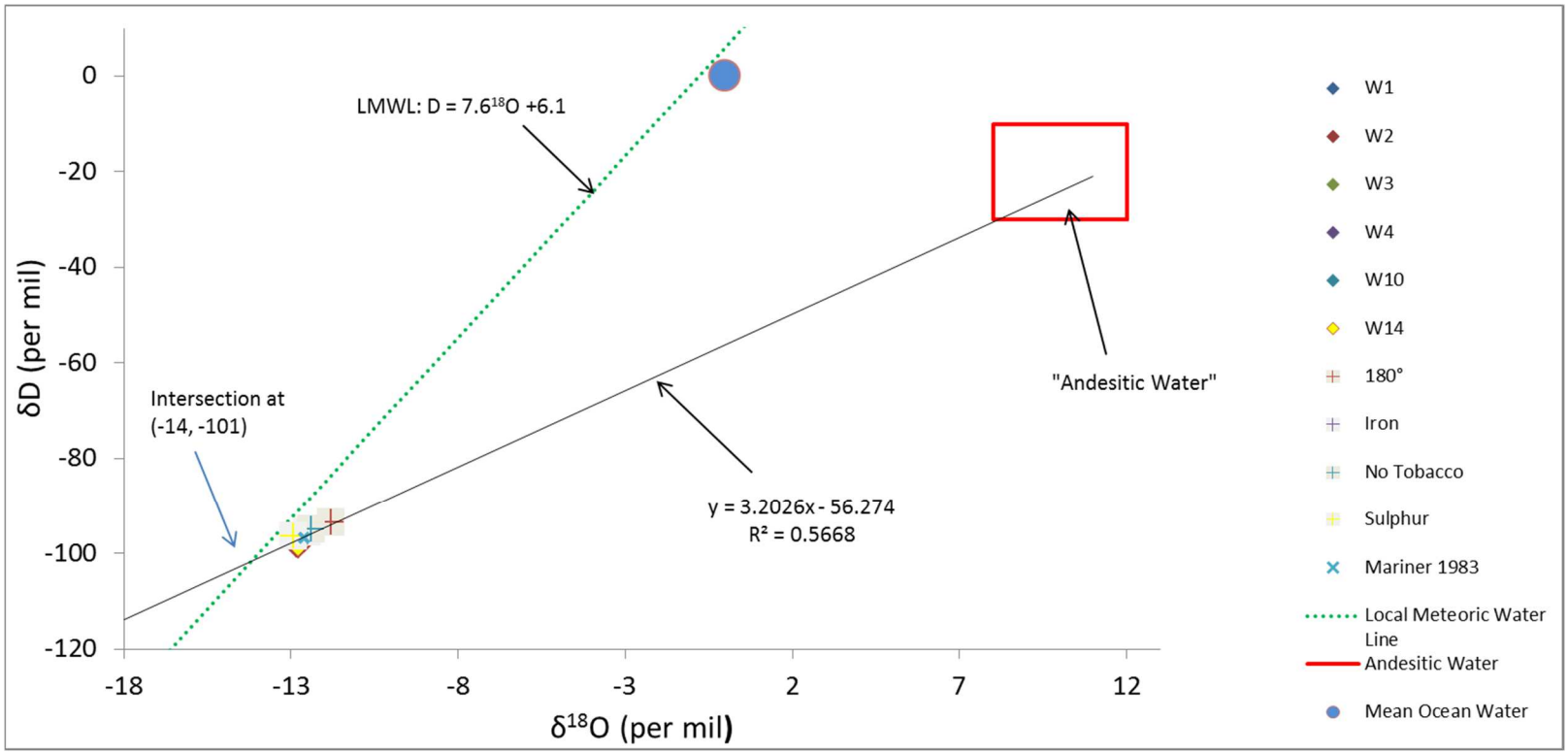

Figure 17: Isotopic data from Breitenbush Hot Springs in context of "andesitic water" of Giggenbach, 1992. The trend line fit from Breitenbush data extrapolates to andesitic water and the local meteoric water line.

Figure 18 shows a Piper diagram for the Wind River Valley samples. St. Martin's waters plot as Na-Cl waters and the Shipherd's samples plot between Na-HCO_3^- and Na-Cl waters. This is potentially indicative of shallow mixing occurring at the Shipherd's Hot Spring that is not present at St Martin's Hot Spring.

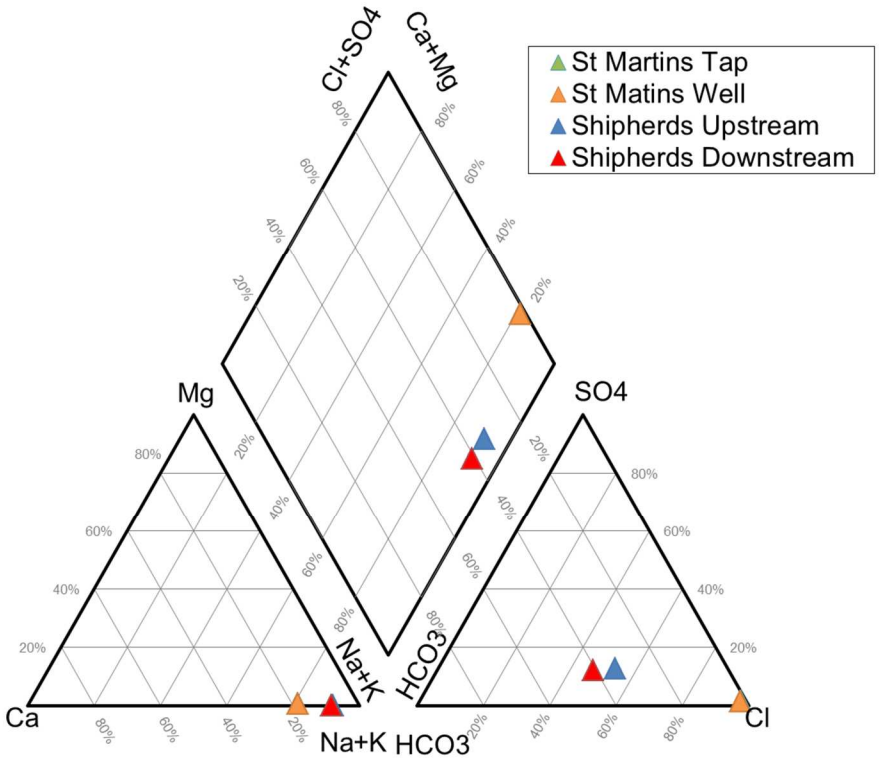

Figure 18: Piper diagram of Wind River samples. The St. Martin's Hot Spring samples directly overprint each other, but are located distinctly in the Na-Cl quadrant.

Table 5: Temperature, pH, conductivity, Eh, and pe for Breitenbush and Wind River samples.

Sample Location	Sample Date	Temp (°C)	Field Parameter Temp (°C)	Field pH	Lab pH (22°C)	Field Conductivity (µS/cm)	Field Specific Conductance (µS/cm)	Eh (mV)	pe
Breitenbush Wells									
W1	11/19/2014	86	62	6.95	6.72	8582	5020	65.0	0.980
W2	2/21/2015	17.6	18	7.61	7.66	3395	3400	66.0	1.13
W3	11/19/2014	71	23	6.90	6.75	4728	4914	113	1.92
W4	11/19/2014	74	45	6.91	6.60	3784	4751	154	2.44
W10	10/7/2014	64	32	6.85	6.93	5733	5028	124	2.05
W11	2/21/2015	16.6	17	9.16	9.06	190.0	228.0	191	3.31
W12	10/7/2014	16	16	9.30	8.96	239.5	288.9	133	2.32
W14	10/7/2014	29	29	7.27	7.32	5498	5136	55.0	0.920
W10-62	6/30/2015	62	55	7.55	7.06	5368	3564	109	1.67
W10-72.4	6/30/2015	72.4	55	7.35	7.06	5704	3551	121	1.86
W10-77.5	6/30/2015	77.5	55	7.51	7.06	5660	3562	98.0	1.50
W10-79.5	6/30/2015	79.5	22	7.98	7.01	3225	3465	163	2.78
W10-82	6/30/2015	82	47	7.43	6.86	4920	3500	163	2.56

Table 5: (continued)

Sample Location	Sample Date	Temp (°C)	Field Parameter Temp (°C)	Field pH	Lab pH (22°C)	Field Conductivity (µS/cm)	Field Specific Conductance (µS/cm)	Eh (mV)	pe
Breitenbush Springs									
180°	11/19/2014	82	30	7.73	7.45	5160	4795	407	6.76
Iron	11/19/2014	85	43	7.23	6.93	3284	2464	205	3.27
No Tobacco	11/19/2014	77	35	7.73	7.37	3130	2628	254	4.15
Sulphur	11/19/2014	58	42	7.17	7.03	6723	5102	131	2.09
South Camp	6/30/2015	43	43	7.59	7.36	4532	3411	290	4.63
Breitenbush River									
Upstream River	6/30/2015	14.4	14	7.59	7.48	27.9	35.7	-	-
Downstream River	6/30/2015	15	15	7.86	7.1	46.2	57	-	-
Wind River Samples									
St Martin's Tap	11/16/2015	51.6	52	8.18	7.92	3404	2249	-32.0	-0.500
St Martin's Well	11/16/2015	51.5	52	8.20	7.8	3404	2260	26.0	0.400
Shipherd's 1	11/16/2015	34.7	30	9.40	9.355	280.9	236	288	4.78
Shipherd's 2	11/16/2015	39.3	30	9.38	9.1	298	232	282	4.68

Table 6: Major ion concentrations, total dissolved solids, and charge imbalances for Breitenbush and Wind River samples. Total dissolved solids value and charge imbalance are reported from Geochemist's Workbench speciation output.

Sample Location	Na (mg/L)	SiO_2 (mg/L)	Ca (mg/L)	K (mg/L)	Mg (mg/L)	Fe (µg/L)	Mn (µg/L)	Alkalinity as $CaCO_3$ (mg/L)	Cl (mg/L)	SO_4 (mg/L)	F (mg/L)	TDS (mg/L)	Charge Imbalance (%)
Breitenbush Wells													
W1	698	148	90	53	0.70	127	116	120	1115	141	3.66	2396	-0.68
W2	745	18.7	85	3.6	0.12	49.8	65	60	1309	140	4.87	2333	-5.83
W3	703	158	92	52	0.68	163	165	133	1110	141	3.56	2422	-0.52
W4	695	153	90	54	0.57	112	82	131	1145	143	3.51	2456	-2.40
W10	746	138	95	42	0.67	306	132	129	1216	145	3.53	2527	-2.04
W11	111	19.5	1.6	0.41	0.01	27.0	1.5	150	52	9.5	7.10	366	-1.75
W12	63	38.0	0.31	0.30	0.07	232	3.8	158	0.69	1.67	0.69	288	-8.42
W14	743	67.0	123	15	0.27	373	70	70	1241	142	2.22	2381	-0.47
W10-62	762	129	98	39	0.68	222	131	133	1208	139	3.33	2498	-0.52
W10-72.4	769	125	94	40	0.7	316	123	129	1224	142	3.33	2506	-1.09
W10-77.5	810	126	98	43	0.7	167	130	133	1233	142	3.30	2570	1.17
W10-79.5	788	128	100	42	0.8	147	128	135	1231	141	3.29	2551	0.02
W10-82	777	133	101	44	0.8	140	122	136	1209	142	3.26	2559	0.32

Table 6: (continued)

Sample Location	Na (mg/L)	SiO_2 (mg/L)	Ca (mg/L)	K (mg/L)	Mg (mg/L)	Fe (µg/L)	Mn (µg/L)	Alkalinity as $CaCO_3$ (mg/L)	Cl (mg/L)	SO_4 (mg/L)	F (mg/L)	TDS (mg/L)	Charge Imbalance (%)
Breitenbush Springs													
180°	706	149	94	52	0.66	42	59	119	1115	140	3.72	2372	0.04
Iron	645	144	88	50	0.89	152	138	119	1010	129	3.47	2215	0.20
No Tobacco	659	145	89	50	0.87	127	132	118	1023	131	3.52	2216	0.79
Sulphur	699	148	98	51	1.09	177	167	142	1102	140	3.58	2398	-0.22
South Camp	777	145	93.8	51	1.31	289	79	133	1214	136	3.58	2544	0.39
Breitenbush River													
Upstream River	8	27.3	4.3	1.0	1.3	0.50	nd	26	0.396	0.47	0.029	75	12.3
Downstream River	7	27.3	4.8	1.1	1.3	2.1	0.8	27	5.82	1.2	0.041	84	-3.4
Wind River Samples													
St Martin's Tap	393	44.9	78.1	10	1.48	8.8	3.3	18	660	13	0.61	1212	5.1
St Martin's Well	395	45	78.5	10	1.48	7.4	3.2	20	658	14	0.60	1215	5.3
Shipherd's 1	48.4	46.3	3.7	0.49	0.05	7.9	0.57	40	35.1	11	0.50	198	-0.42
Shipherd's 2	47.5	45.3	3.8	0.45	0.03	10.7	nd	47	32.7	12	0.32	201	-0.52

Table 7: Trace element concentrations for Breitenbush and Wind River samples. Note that Cd, B, and Sb were not analyzed on every run.

Sample Location	B (µg/L)	Li (µg/L)	Sr (µg/L)	As (µg/L)	Ba (µg/L)	Al (µg/L)	Cd (µg/L)	Cu (µg/L)	Zn (µg/L)	Sb (µg/L)	Pb (µg/L)	Br (µg/L)	NO_3 (µg/L)	NO_2 (µg/L)	HPO_4 (µg/L)
Breitenbush Wells															
W1	4284	1858	623	438	47	14	4.2	2.1	35	10	30	3301	nd	nd	104
W2	2810	741	32.8	116	8.8	13	nd	2.3	1.3	2.1	nd	4440	nd	nd	nd
W3	4023	1512	525	469	52	16	3.9	2.5	0.90	2.1	nd	3283	156	nd	264
W4	3540	1601	524	480	50	12	3.6	2.4	47	6.7	nd	3316	nd	nd	nd
W10	4524	1659	371	481	38	30	nd	2.4	1.4	5.9	nd	3417	nd	nd	244
W11	na	92	1.50	105	nd	34	nd	3.0	1.8	na	2.4	180	nd	nd	nd
W12	417	375	1.80	34	55	125	nd	0.51	5.3	nd	nd	nd	50	nd	nd
W14	4217	1809	112	282	21	154	nd	2.9	nd	nd	nd	3660	103	nd	nd
W10-62	na	2960	401	473	37	54	nd	nd	19	na	nd	3360	nd	nd	nd
W10-72.4	na	1409	403	492	37	8.0	nd	2.3	20	nd	nd	3374	nd	nd	nd
W10-77.5	na	1425	432	509	40	7.4	nd	2.0	31	nd	nd	3390	nd	nd	nd
W10-79.5	na	1382	423	500	39	7.9	nd	2.0	22	nd	nd	3365	nd	nd	nd
W10-82	3510	1641	428	487	40	4.1	nd	2.3	30	11	nd	3324	nd	nd	nd

Table 7: (continued)

Sample Location	B (µg/L)	Li (µg/L)	Sr (µg/L)	As (µg/L)	Ba (µg/L)	Al (µg/L)	Cd (µg/L)	Cu (µg/L)	Zn (µg/L)	Sb (µg/L)	Pb (µg/L)	Br (µg/L)	NO_3 (µg/L)	NO_2 (µg/L)	HPO_4 (µg/L)
Breitenbush Springs															
180°	3982	1853	674	442	43	8.8	4.4	2.4	nd	12	nd	3343	1836	396	nd
Iron	4210	1764	621	425	45	6.1	4.1	1.5	nd	11	nd	3096	161	nd	23
No Tobacco	3826	1745	635	426	45	6.2	3.9	1.6	nd	11	nd	3144	167	441	25
Sulphur	3786	1791	675	425	53	4.7	4.2	1.7	7.4	11	nd	2758	3021	nd	nd
South Camp	3417	2653	578	490	47	3.6	na	2.2	20	11	nd	3310	2.5	nd	nd
Breitenbush River															
Upstream River	56.5	2.6	25.3	nd	0.80	5.2	na	0.20	28	nd	nd	nd	nd	nd	nd
Downstream River	47.1	16.3	28.5	1.3	1.2	6.0	na	0.30	23	nd	nd	nd	nd	nd	nd
Wind River Samples															
St Martin's Tap	3616	221	76.1	1.6	3.8	8.0	na	1.7	8.6	nd	nd	2037	299	nd	nd
St Martin's Well	3589	222	76.3	1.6	3.7	10	na	1.8	2.9	nd	0.2	2092	86	nd	nd
Shipherd's 1	957	20.7	6.90	11	nd	33	na	nd	nd	nd	nd	125	nd	nd	nd
Shipherd's 2	963	21.5	6.80	12	nd	29	na	nd	nd	nd	nd	136	nd	nd	nd

Table 8: Isotopes analysis results for Breitenbush and Wind River samples. Included are sulfate and chlorine isotope data reported from previous studies at Breitenbush.

Sample Location	δ^2H (‰)	$\delta^{18}O$ (‰)	$\delta^{18}O_{SO4}$ (‰)	$\delta^{37}Cl$ (‰)
Breitenbush Wells				
W1	-96.65	-12.59		
W2	-98.08	-12.83		
W3	-96.08	-12.61		
W4	-97.05	-12.6		
W10	-96.96	-12.77		
W11	-97.01	-13.9		
W12	-89.13	-12.74		
W14	-98.27	-12.76		
W10-62	-97.42	-12.26		
W10-82	-96.74	-12.58		
Breitenbush Springs				
180°	-93.59	-11.81		
Iron	-95.63	-12.52		
No Tobacco	-94.96	-12.39		
Sulphur	-96.39	-12.91		
South Camp	-94.82	-12.07		
Breitenbush River				
Upstream River	-85.78	-12.03		
Downstream River	-84.79	-11.91		
Breitenbush Historic Values				
Mariner 1983	-97	-12.6	-2.67	
Hull 2015	-102	-12.3		0.9
Wind River Samples				
St Martin's Tap	-88.612	-11.55		
St Martin's Well	-88.751	-11.80		
Shipherd's 1	-84.818	-11.88		
Shipherd's 2	-84.802	-11.73		

4.1.1 Quality Control

Charge balance errors were generally acceptable (i.e. less than 5%). The majority of samples had charge balance errors with absolute values less than 1. The sign of the charge balance errors varied from sample to sample, suggesting random, rather than systematic, error. Five samples had charge balance errors with absolute values greater than 5%. These tended to be waters with relatively low total dissolved solids. For example, the upstream sample collected from the Breitenbush River had the highest charge balance error (12.29%) with an associated total dissolved solids value of 75. For Breitenbush wells W2 and W11, laboratory alkalinity results were processed outside of the applicable holding time and the results were considered unacceptable; field alkalinity values were used for these samples. Full quality control results are included in Appendix B.

4.2 Breitenbush Geothermometry

4.2.1 Classical Geothermometry

Table 9 shows the temperature estimate of each classical geothermometer used for this report for both Breitenbush and Wind River samples. Shaded cells indicate estimates outside of the acceptable range for a particular geothermometer. Figure 19 shows results of the silica geothermometer of Arnórsson (1998) for all of the Breitenbush samples. Figure 20 shows results of the Na-K-Ca geothermometer of Fournier and Truesdell (1973-79) for all of the Breitenbush samples.

Table 9: Results of various classical geothermometers as applied to Breitenbush and Wind River samples. Refer to Table 4 for geothermometer reference information.

Sample Location	Chalcedony (F77) (°C)	α-Crisobalite (F77) (°C)	β-Crisobalite (F77) (°C)	Amorphous Silica (F77) (°C)	Na-K-Ca (FT73-79) (°C)	Na/Li (FM81) (°C)
Breitenbush Wells						
W1	135	109	60	37	178	136
W2	28	11	-32	-49	57	75
W3	140	113	64	41	176	121
W4	138	111	62	39	179	126
W10	131	105	55	33	163	123
W11	30	13	-31	-47	52	66
W12	58	39	-7	-25	70	204
W14	86	65	17	-2	95	130
W10-62	126	100	51	29	158	166
W10-72.4	124	99	50	28	159	111
W10-77.5	124	99	50	28	160	108
W10-79.5	125	100	51	29	160	108
W10-82	128	102	53	31	163	120
Breitenbush Springs						
180°	136	110	60	37	176	135
Iron	133	107	58	36	177	138
No Tobacco	134	108	58	36	177	136
Sulphur	135	109	60	37	175	133
South Camp	134	108	58	36	152	155
Breitenbush River						
Upstream River	43	25	-20	-37	35	25
Downstream River	43	25	-20	-37	35	127
Wind River Samples						
St Martin's Tap	66	46	0	-19	82	47
St Martin's Well	66	46	0	-19	82	48
Shipherd's Upstream	67	47	1	-18	35	36
Shipherd's Downstream	66	46	0	-18	32	38

Shaded cells indicate that the estimate is outside of the applicable range for the listed geothermometer.

Table 9: (Continued)

Sample Location	SiO2 (FP82) (°C)	Na/K (VS97) (°C)	Na/Li (VS97) (°C)	SiO2 (VS97) (°C)	SiO2 (A98) (°C)	Na/K Eq 1 (D08) (°C)
Breitenbush Wells						
W1	183	198	147	159	149	163
W2	74	55	86	61	45	1
W3	188	196	132	164	154	160
W4	185	200	137	162	151	165
W10	178	177	135	155	145	136
W11	76	45	76	62	47	-9
W12	106	54	216	90	75	0
W14	135	117	141	116	102	67
W10-62	174	170	177	151	140	128
W10-72.4	172	172	122	149	138	130
W10-77.5	172	172	119	150	139	131
W10-79.5	173	172	119	151	140	131
W10-82	176	177	131	153	142	136
Breitenbush Springs						
180°	184	196	146	160	150	160
Iron	181	200	149	158	147	164
No Tobacco	182	198	147	158	148	163
Sulphur	183	196	145	159	149	159
South Camp	182	187	166	158	148	148
Breitenbush River						
Upstream River	91	239	35	76	61	214
Downstream River	91	260	138	76	61	243
Wind River Samples						
St Martin's Tap	114	126	126	97	82	77
St Martin's Well	115	126	126	97	82	77
Shipherd's 1	116	84	84	98	84	31
Shipherd's 2	115	81	81	97	83	28

Shaded cells indicate that the estimate is outside of the applicable range for the listed geothermometer.

Table 9: (Continued)

Sample Location	Na/K Eq 2 (D08) (°C)	Na/K Eq 3 (D08) (°C)	Na/K (C02) (°C)	Median	Mean	Range
Breitenbush Wells						
W1	173	166	184	159	145	161
W2	-1	2	91	59	55	74
W3	170	163	182	160	144	157
W4	175	168	185	162	145	161
W10	146	139	164	139	132	145
W11	-11	-8	88	57	53	63
W12	-1	1	91	82	107	177
W14	72	69	120	116	111	76
W10-62	138	131	158	140	133	145
W10-72.4	140	133	160	133	126	144
W10-77.5	140	133	160	133	126	144
W10-79.5	141	133	160	133	126	144
W10-82	146	139	164	139	131	146
Breitenbush Springs						
180°	170	163	182	160	144	164
Iron	174	167	185	158	145	163
No Tobacco	173	166	184	158	144	163
Sulphur	169	162	181	159	144	159
South Camp	158	151	173	152	141	151
Breitenbush River						
Upstream River	222	218	225	91	132	200
Downstream River	247	247	248	127	141	223
Wind River Samples						
St Martin's Tap	83	79	125	82	87	80
St Martin's Well	83	79	125	82	88	80
Shipherd's 1	32	33	102	84	77	81
Shipherd's 2	29	30	101	81	77	83

Shaded cells indicate that the estimate is outside of the applicable range for the listed geothermometer.

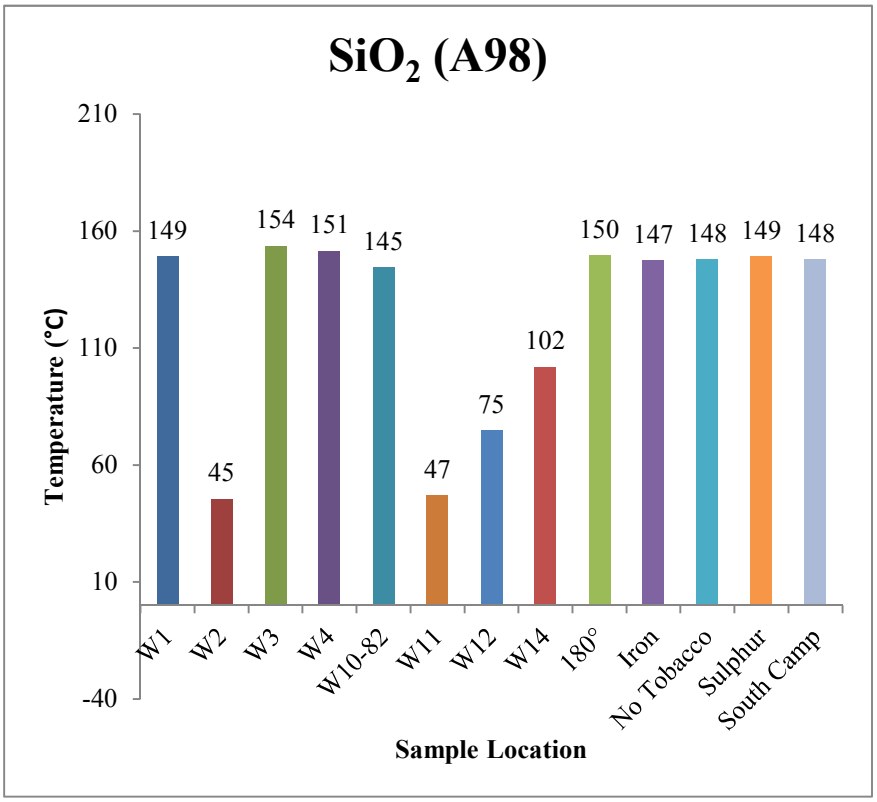

Figure 19: Silica geothermometer of Arnórsson, 1998, showing estimated reservoir temperatures of Breitenbush samples.

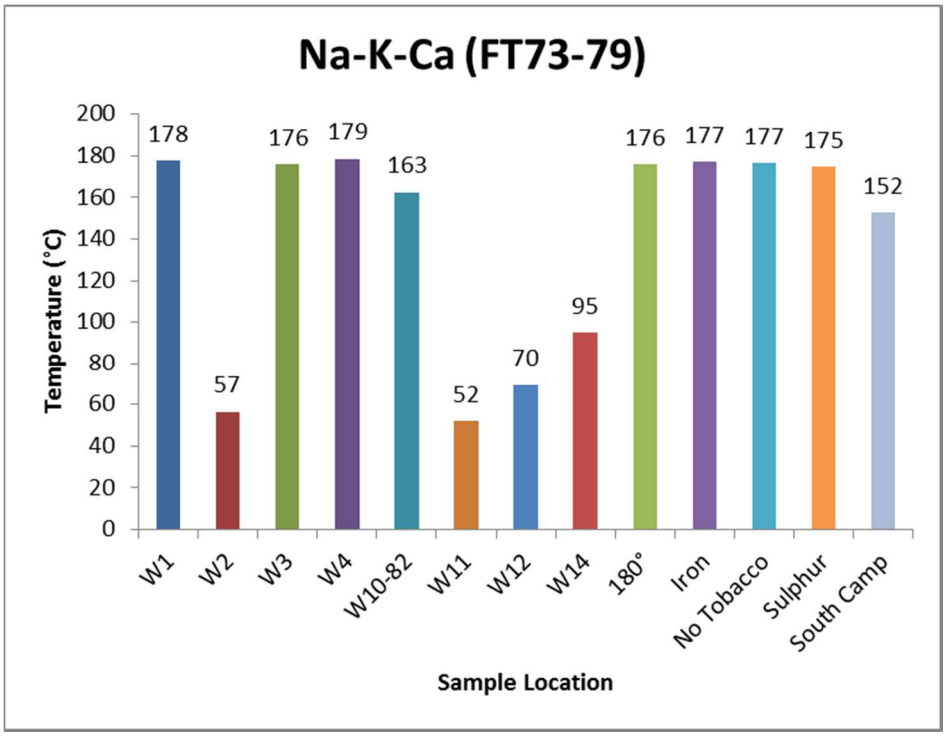

Figure 20: Na-K-Ca geothermometer of Fournier and Truesdell, 1973, showing estimated reservoir temperatures for Breitenbush samples.

Figure 21 shows the results of each of the classical geothermometers, as well as their mean and median values for W4. The average of the three quartz geothermometers is 169 °C. The chalcedony geothermometer yields an estimate of 138 °C. The average of the six Na-K geothermometers is 179 °C.

In contrast to W4, the sample collected from W12 indicates a cool shallow source. Figure 22 shows the results of each of the classical geothermometers, as well as their mean and median values for W12. These results are similar to that of the Breitenbush River (Table 9). When using chemistry from the river samples, the estimated reservoir

temperatures range from 25 to 260 °C. That the river water is only minutely contributed to from deep thermal water underscores that the empirical classical geothermometers were developed particularly with thermal waters in mind.

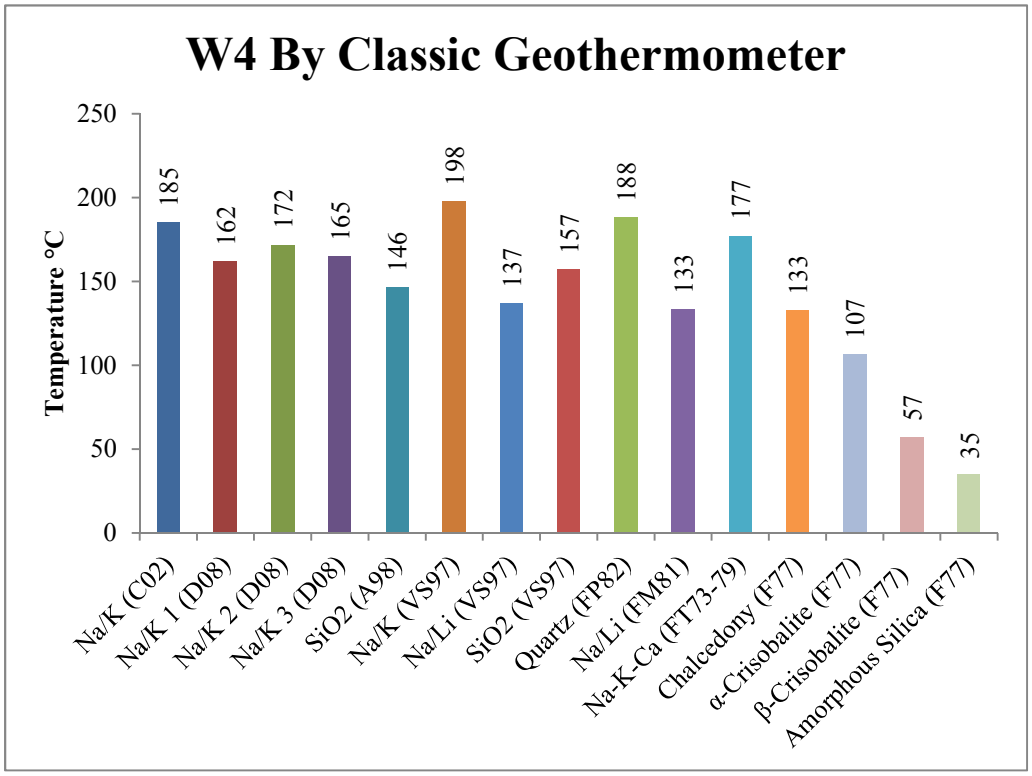

Figure 21: Each of the classic geothermometers used for this study applied to water chemistry of W4.

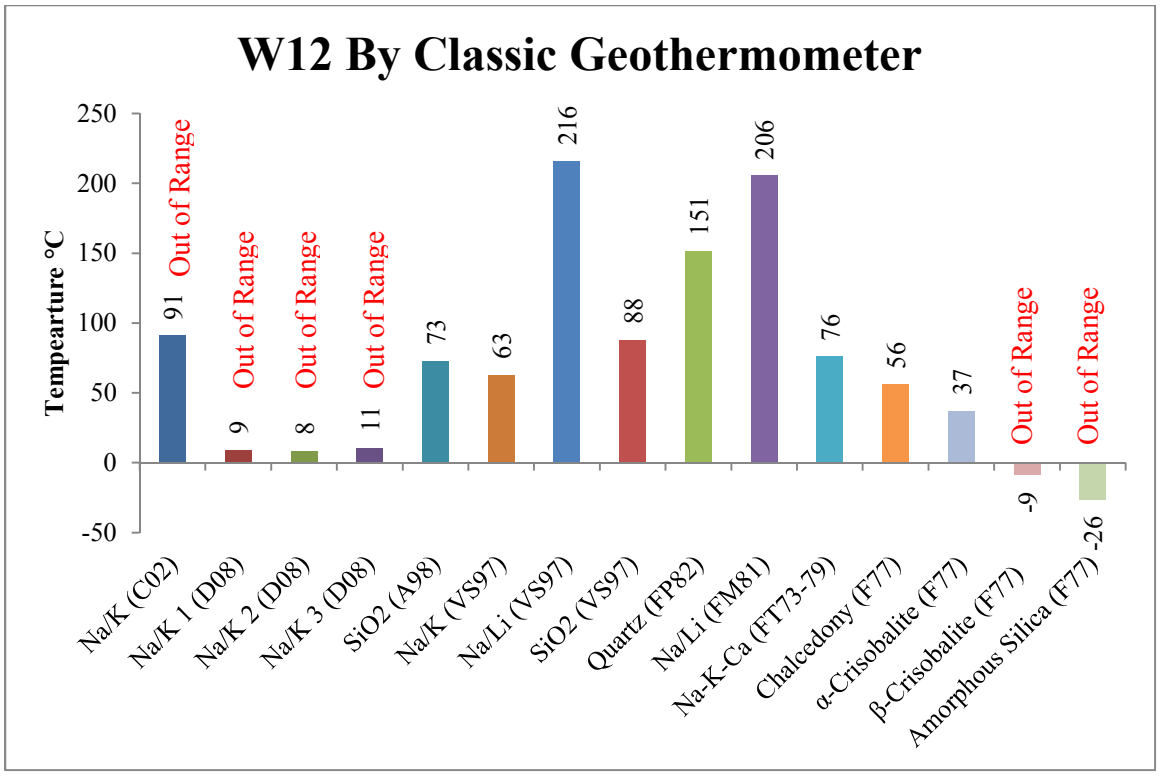

Figure 22: Each of the classic geothermometers used for this study applied to water chemistry of W12. Six of the geothermometers are outside of the applicable range.

Figure 23 shows a Giggenbach diagram for all of the Breitenbush samples. Figure 24 shows a plot of SiO_2 in mg/kg versus log(K^2/Mg). These plots both show waters from W12 on the extreme between other samples and the bulk of the spring samples. In particular, the SiO_2 versus log (K^2/Mg) plot shows a potential mixing curve between the waters. This would indicate that the shallow waters represented by W12 have mixed with thermal waters to yield the waters of W11, W2, and W14, in decreasing proportion. W10 also appears to be affected by mixing of W12 waters, though to a lesser extent than W11, W2, or W14.

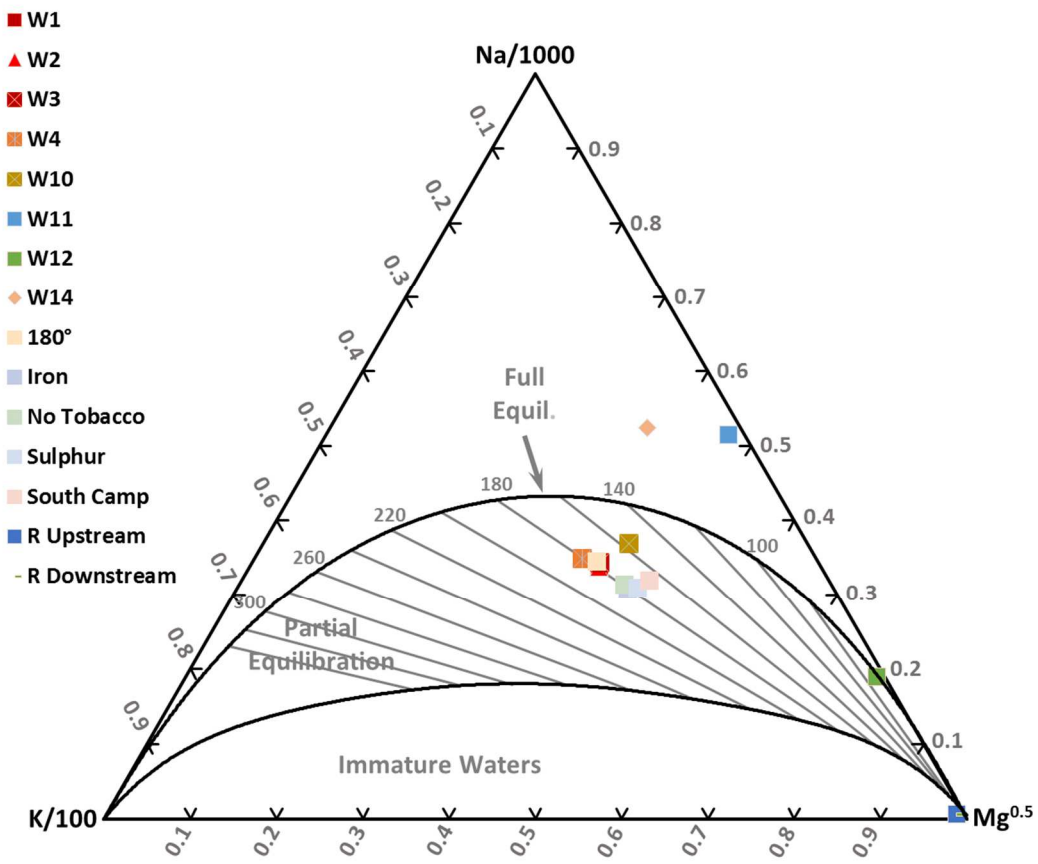

Figure 23: Giggenbach diagram for Breitenbush Hot Spring samples.

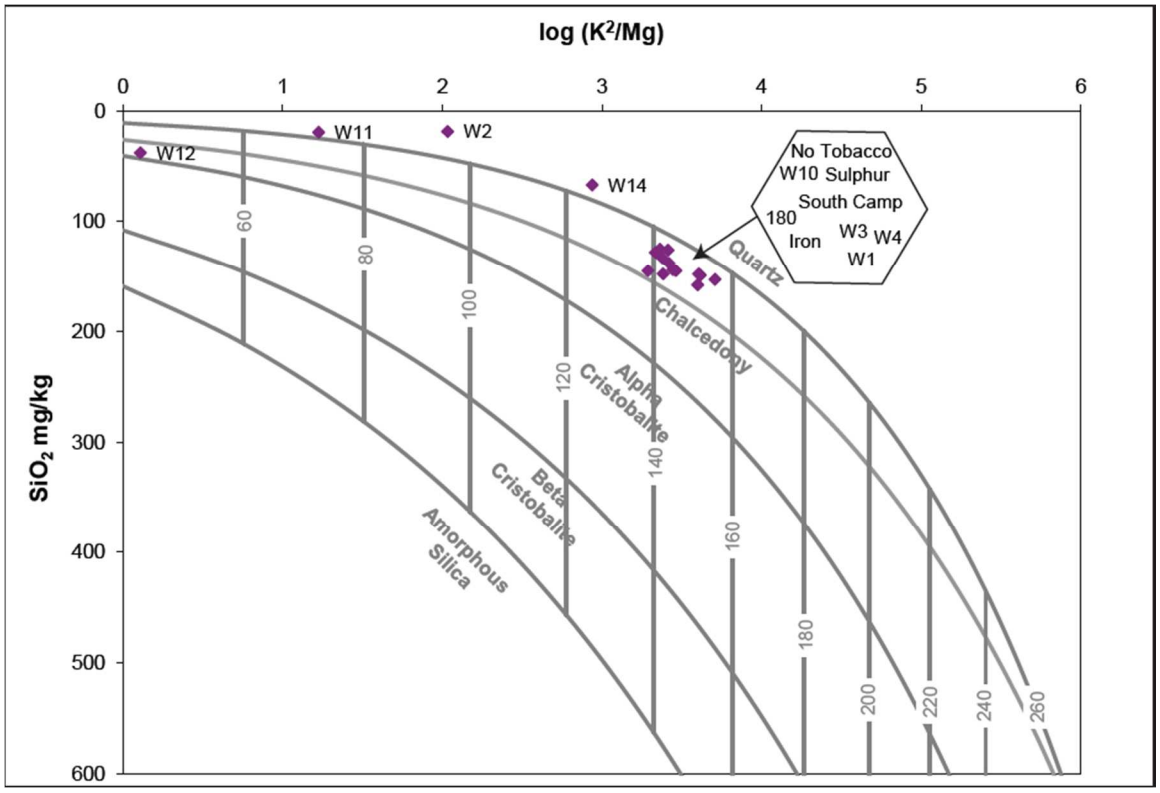

Figure 24: SiO2 versus log (K2/Mg) diagram for Breitenbush Hot Spring samples. The curve between the clumped values and W12 shows a potential mixing pathway.

4.2.2 GeoT

GeoT allows the user to simply input water chemistry and allow the program to generate the best fit temperature based on an arbitrary collection of minerals that are listed in the chosen geothermal database and that have basis species present in the provided water chemistry. This is a fast way to generate an initial temperature estimate and mineral assemblage. The temperature estimate is produced by calculating chemical speciation and mineral saturation indices and comparing the median of saturation indices (RMED) for a selected number of minerals at each evaluated temperature. Although RMED is used for the temperature determination, GeoT also calculates the root mean square error (RMSE), standard deviation (SDEV), and mean (MEAN) of the saturation indices for the chosen number of minerals. Each of these four statistics is optimized at a value of 0, which would correspond to equilibrium conditions for all of the minerals assessed. In addition to these statistics, GeoT also provides an automated measure of the discrepancy between statistics, T_{RMED}-T_{STATAV}, which takes the difference between the temperature at which RMED is minimized and the mean of the temperatures at which RMSE, SDEV, and MEAN are minimized. This statistic also has an ideal value of zero, which would result if the temperature of each minimized statistic was identical. In addition, GeoT lists the average temperature at which the minerals used for statistics have SI=0 (T_{DT}), the difference between the highest and lowest of these temperatures (DT), and the standard deviation of this difference (σ_{DT}) (Spycher et al., 2014).

A plot of temperature, minerals, and statistics output using water chemistry from W4 with no additional user inputs is shown on Figure 25. The default number of minerals to assess is 10, and this arbitrary number was used to generate temperature and statistics for the minerals shown in Figure 25. In Figure 25 and other GeoT figures presented here, T_{RMED} is listed on the upper half of the figure and the T_{RMED}-T_{STATAV} value is listed in the lower half of the figure. T_{DT} and T_{RMED} are generally different temperatures. For this GeoT result, T_{RMED} = 136 °C, T_{DT} = 132.5, DT = 23, and σ_{DT} = 6.87.

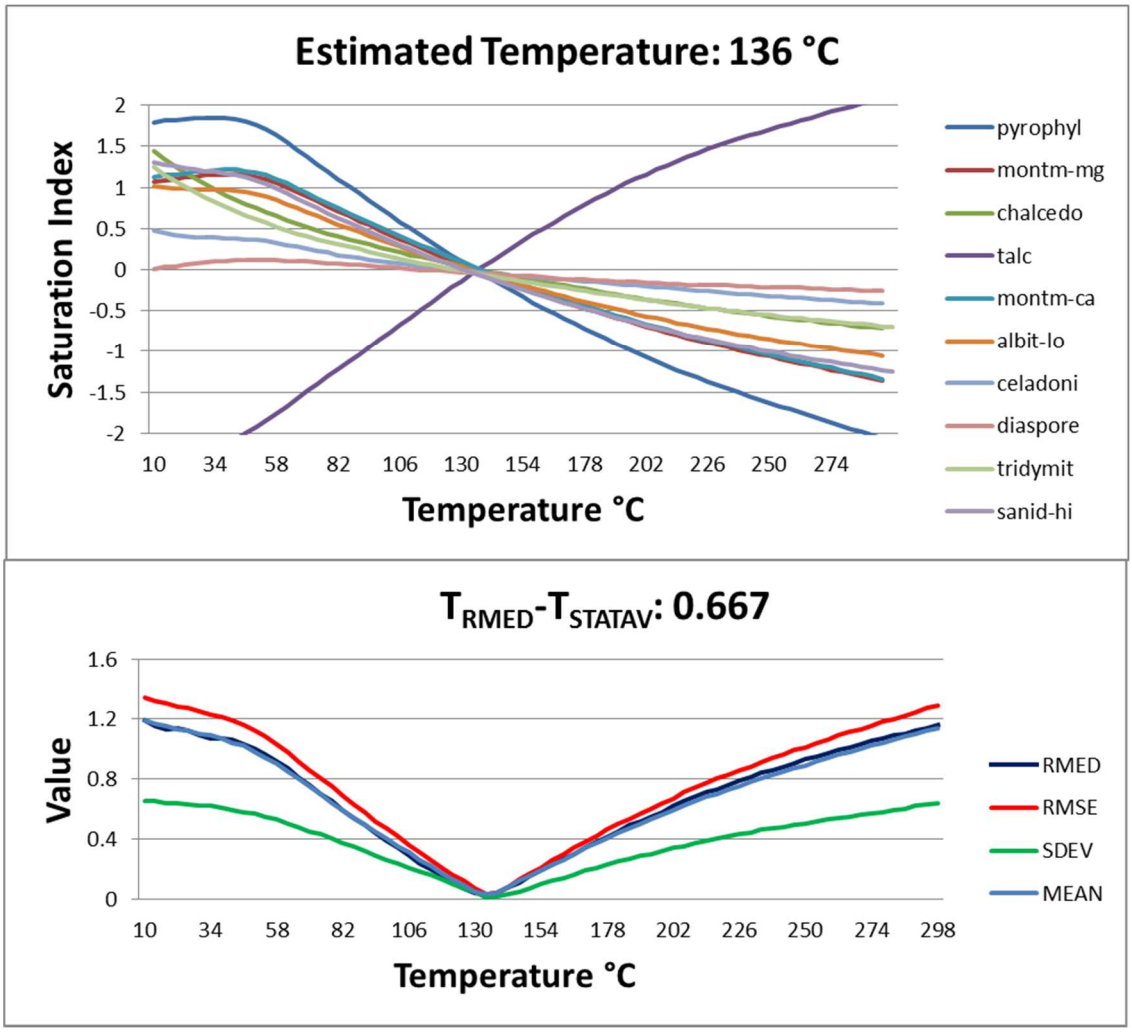

Figure 25: GeoT output for W4 with limited user input. Estimated reservoir temperature is 136 °C ± 6.87 °C and T_{RMED}-T_{STATAV} is 0.667.

Due to the prevalence of silicate minerals, it is likely that geothermal fluids contain enough dissolved silica to show equilibrium with quartz or its polymorphs. Both chalcedony and quartz were observed in deep borings and exhibit equilibrium temperatures within a reasonable range of temperatures (i.e. greater than measured

borehole temperatures and less than the highest classical geothermometer temperature estimates). As shown in Figure 25, chalcedony exhibited equilibrium with the W4 water sample with no additional inputs or forcing. Figure 26 shows the output from GeoT produced when limiting the mineral selection process to five minerals, all of which were observed within the deep Breitenbush area borings (Table 2). The mineral assemblage was further refined by allowing only one type of montmorillonite, and excluding tridymite from consideration, as chalcedony already suffices for a free silica mineral. The resultant mineral assemblage generated by GeoT using these constraints included celadonite, calcite, chalcedony, calcium-beidellite, and sudoite. This assemblage resulted in a temperature estimate of 122 °C ± 6.99 °C.

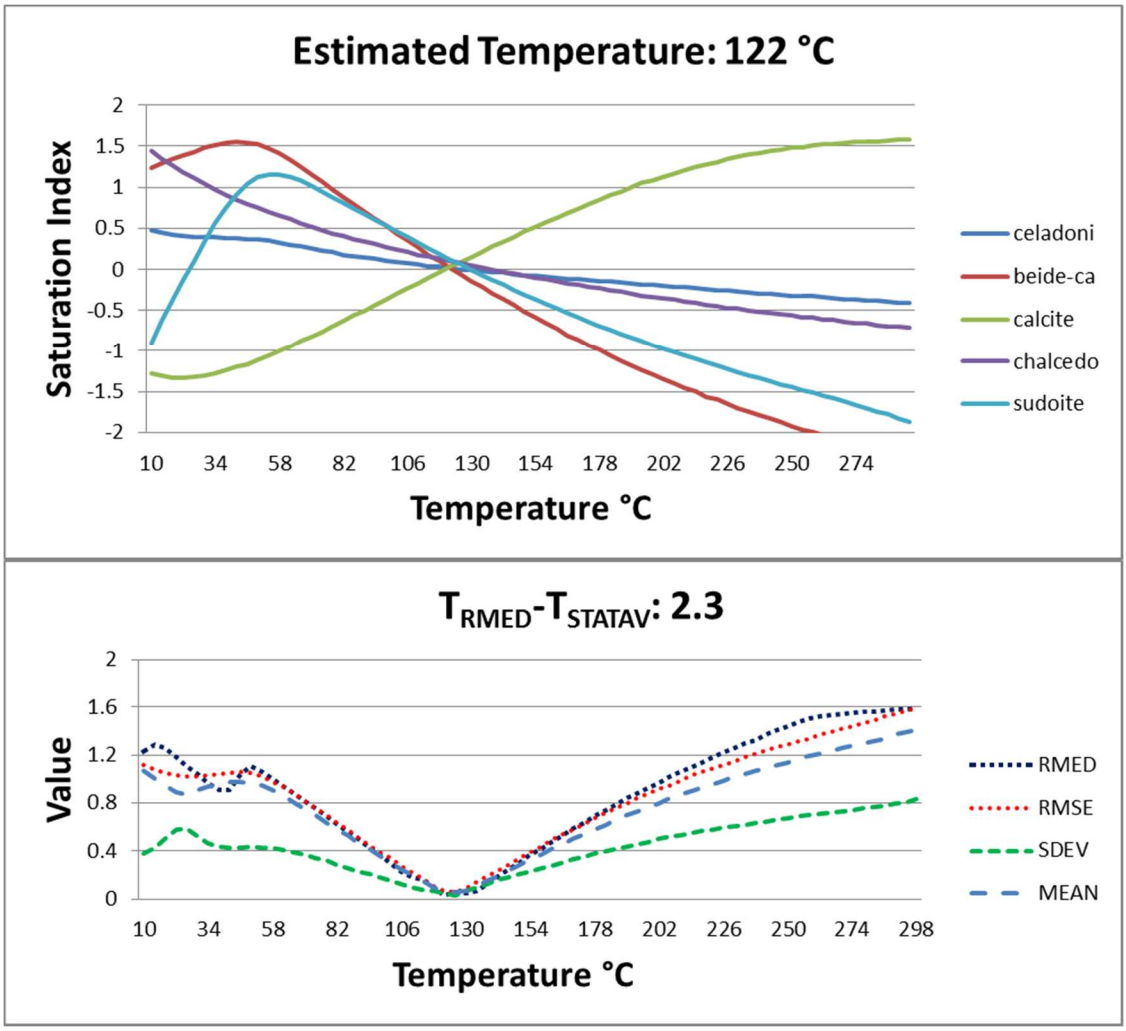

Figure 26: GeoT output using reported minerals in boreholes at or near chalcedony equilibrium temperature.

A similar process was conducted using quartz instead of chalcedony. In this case, however, simply limiting the mineral assemblage to include quartz and exclude its polymorphs was not sufficient to generate a mineral assemblage and temperature estimate

close to quartz' equilibrium temperature. Instead, minerals that were observed in the deep borings which showed equilibrium temperatures close to quartz (anhydrite and stilbite) were included in the estimation process in order to force GeoT to assess minerals in this temperature range. Figure 27 shows the resultant SI versus temperature curves with an associated temperature estimate of 175 ± 24.22 °C.

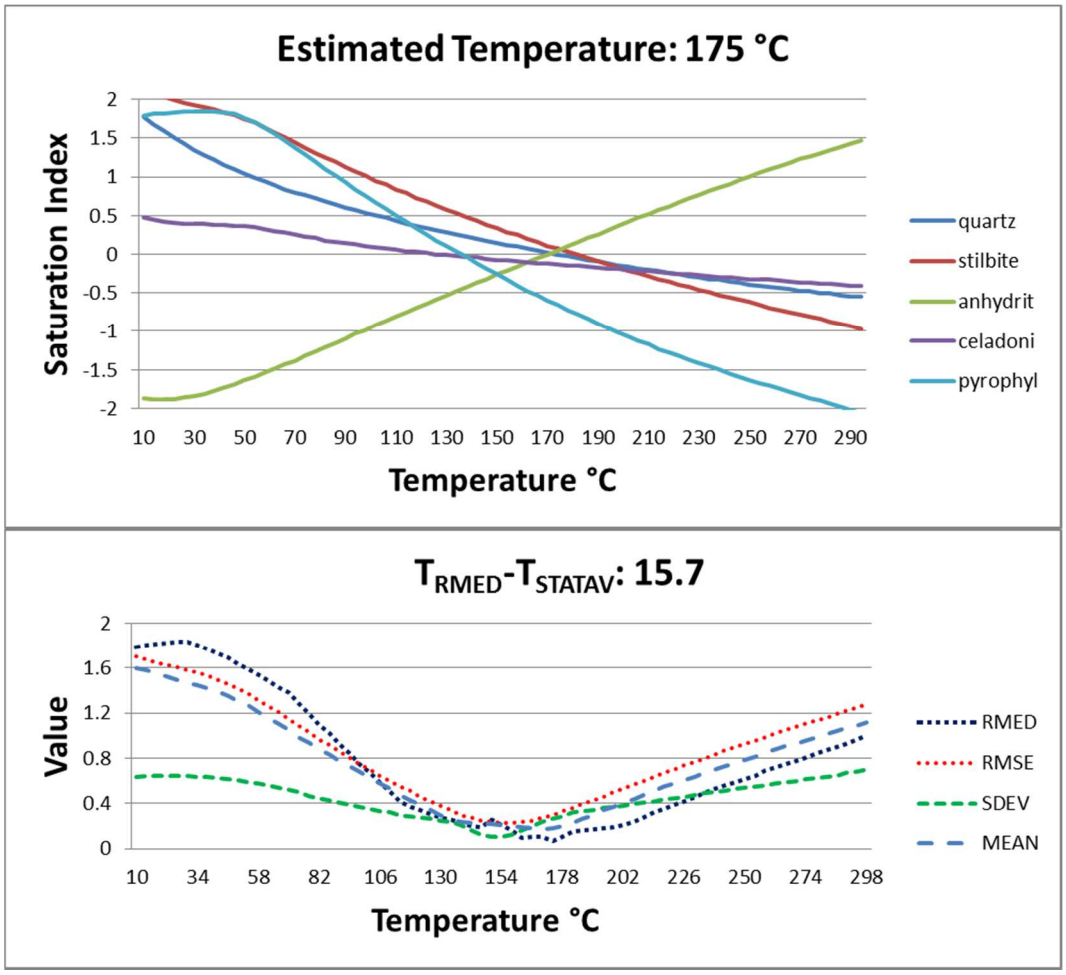

Figure 27: GeoT output using quartz and other minerals close to its equilibrium temperature. Note the disagreement between saturation index curves and the x-intercept as well as the relative scatter among statistic curves.

4.2.2.1 Multiple Water Analysis

GeoT allows the simultaneous assessment of up to 100 waters. For Breitenbush, wells W1, W3, W4, and W10 and South Camp, Sulphur, No Tobacco, Iron, and 180° Springs were simultaneously assessed. W11 and W12 were not assessed due to their

apparent shallow nature. W2 and W14 were not assessed due to their apparent mixing with shallow waters (Table 9, Figures 19, 20 and 24). Using chalcedony, calcium-beidellite, and sudoite yielded an average equilibrium temperature of 114 °C, with a range of 100 °C (South Camp Spring) to 133 °C (W1). Associated T_{RMED}-T_{STATAV} values ranged from 1 (W4) to 17 (180° Spring), with an average of 6. Using quartz, stilbite, and anhydrite yielded an average equilibrium temperature of 172 °C, with a range of 170 °C (Sulfur Spring) to 174 °C (W4). Associated T_{RMED}-T_{STATAV} values ranged from 11 (W1) to 44 (South Camp Spring) with an average of 22. In this regard, the range of estimated temperatures using the chalcedony mineral assemblage was much higher, but the statistics were closer to minimization when compared to the quartz mineral assemblage.

4.2.2.2 Optimization

Optimization using GeoT was performed with PEST. The optimized parameters included steam weight fraction, concentration factor, mixing extent, initiation temperature, and activities (see Section 3.3.2 for a description of these parameters). Various iterations were conducted to determine the range of allowable parameters and the interval with which to adjust the parameters. In addition, the sensitivities of the various parameters were evaluated and tweaked until the salient adjustable parameters were determined. The associated PEST files used with GeoT, including control files, instruction files, and template file, are provided in Appendix C.

Figure 28 shows the results of using optimization on a chalcedony-based mineral assemblage. Optimization was achieved by "unmixing" 20% of a shallow water equivalent to W12, allowing no gas/vapor loss, and adjusted input activities that were generally equal to the original estimate, with the exception of Cl- and F-, both of which increased, and K+, which decreased. The estimated equilibrium temperature was 134± 1.52 °C, and T_{RMED}-T_{STATAV} was 0.00. All six minerals had saturation indices equal to 0 between 134 and 138 °C.

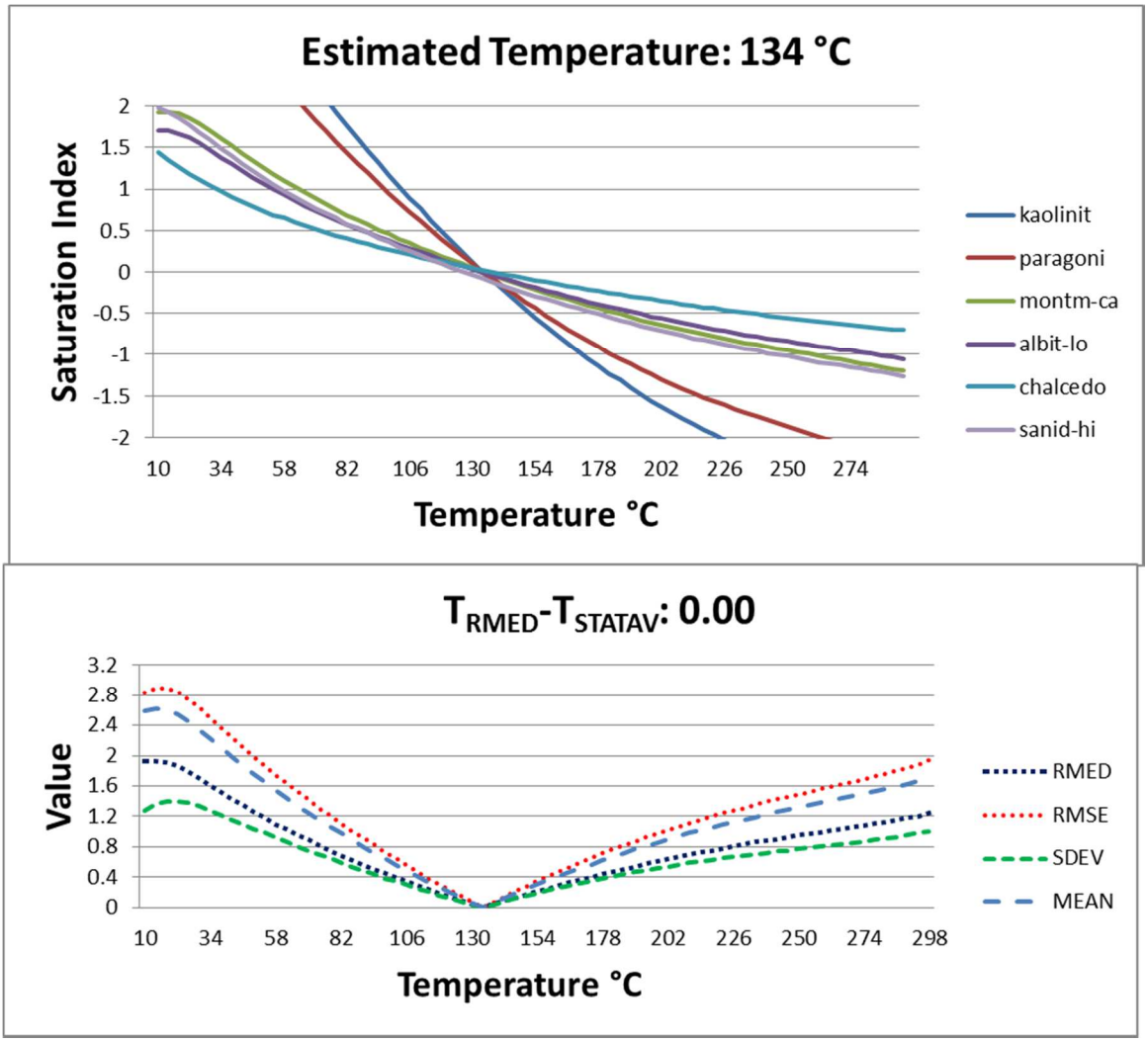

Figure 28: Optimized GeoT output, with optimization for gas loss, shallow water mixing, and activities (within the bounds of analytical uncertainty). Small variation in crossing temperatures was observed, and all four statistics agreed on a temperature of 134 °C.

Figure 29 shows the results of optimization using quartz, anhydrite, heulandite, celadonite, and calcite. The optimized parameters are identical to the original inputs (i.e. no gas loss, no mixing, no dilution), with the exception of an optimized initiation

temperature of 170 °C. The optimized T_{RMED}-T_{STATAV} value was 1 (compared to 13.3 not optimized) and the optimized RMED was 0.045 (compared to 0.066 not optimized). All of the selected minerals in the assemblage were identified in deep borings.

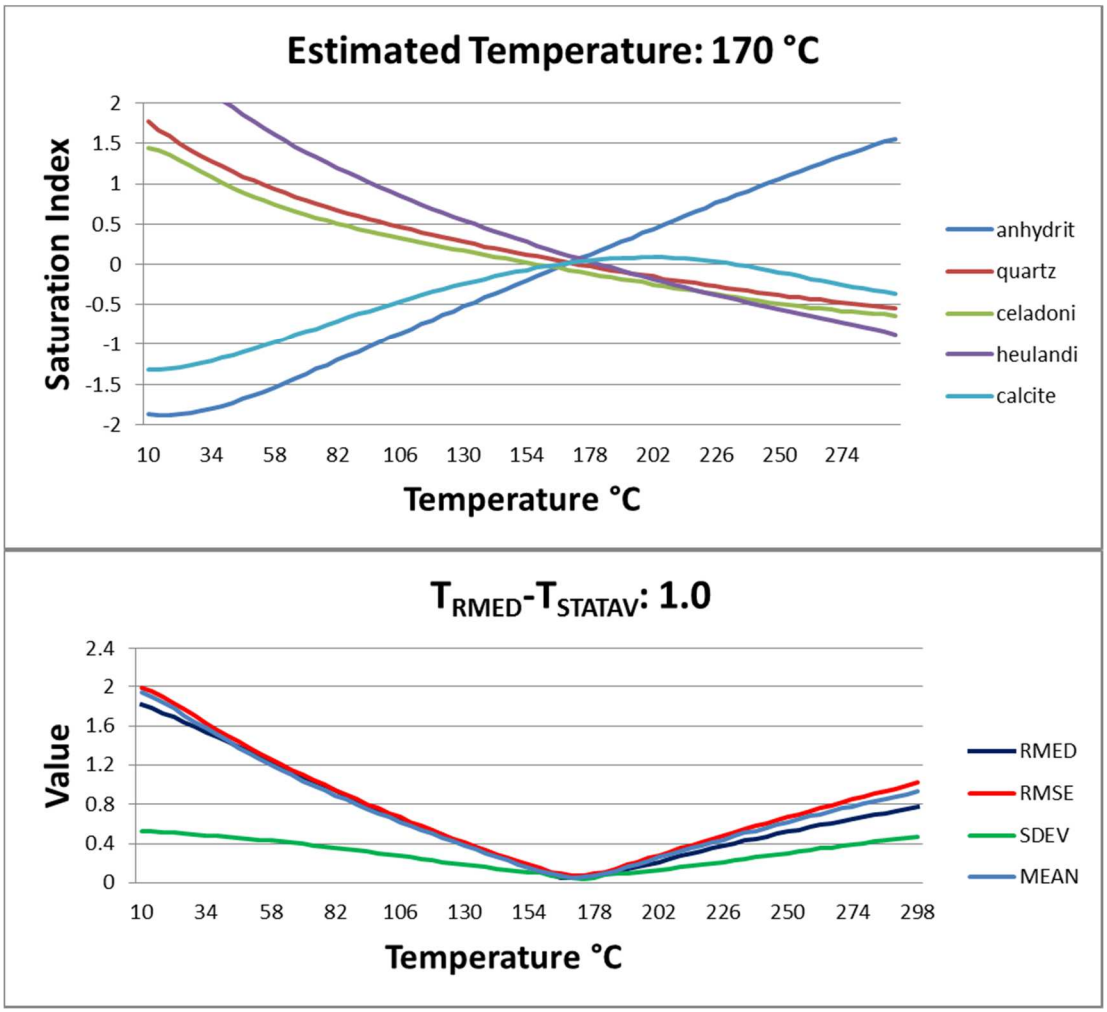

Figure 29: Optimized GeoT output with resultant reservoir estimate of 170°C, and minerals anhydrite, quartz, celadonite, heulandite, and calcite.

4.2.2.3 Summary

An assessment of the sensitivities of the various parameters used in optimization of W4 indicated that the most sensitive parameters were initiation temperature, steam weight fraction, and concentration factor. Using these parameters, each of the well and spring waters collected from Breitenbush were assessed using GeoT. For each sample, the mineral assemblages were adjusted based on observed equilibrium or disequilibrium. Mineral assemblage clusters at both chalcedony and quartz were used for each sample. Table 10 summarizes the results, including the four minerals used for statistics for each water sample. Using the chalcedony mineral assemblage, the median estimated temperature was 134 °C with a standard deviation of 5.8. Using the quartz mineral assemblage, the median estimated temperature was 170 °C, with a standard deviation of 6.8. Table 10 includes statistics for each optimized sample. As is evident in Table 10, steam weight fraction was not determined to have a significant effect on the temperature estimates. This is largely due to the fact that few of the minerals used had carbon bearing basis species, and that the concentration factor parameter already dilutes and concentrates the remaining species such that the additional dilution or concentration of H_2O in the steam fraction is already accounted for.

Table 10: GeoT results for Breitenbush Hot Springs, including statistics, optimized parameter values, and mineral assemblages.									
Sample Location		**W1**		**W2**		**W3**		**W4**	
min RMED	unitless	0.002	0.017	0.016	0.170	0.001	0.017	0.003	0.003
T_{RMED}	(°C)	135	175	128	150	140	176	133	173
$T_{RMED-TSTATAV}$	(°C)	0.67	1.67	1.00	4.00	0.00	2.00	0.33	0.00
T_{DT}	(°C)	135.00	172.50	128.00	154.50	140.00	181.20	134.50	174.00
σ_{DT}	(°C)	1.41	5.74	4.08	5.07	0.00	5.76	1.73	0.82
T-initiation	(°C)	113	162	107	130	130	170	46	74
Gas Loss	(Wght %)	0	0	0	0	0	0	0	0
Concentration factor	unitless	1	0.89	7.7	3	1	1	1	1.01
Mineral Suite		chalcedony, albite-lo, montmorillonite-mg, sanidine-hi	quartz, anhydrite, heulandite, stilbite	chalcedony, montmorillonite-k, wairakite, cummingtonite	heulandite, stilbite, celadonite-fe, cummingtonite	chalcedony, albite-lo, montmorillonite-mg, aragonite	quartz, anthophyllite, heulandite, chloritoid-fe	kaolinite, paragonite, chalcedony, montmorillonite-ca	anhydrite, quartz, celadonite, sepiolite

Table 10: (Continued)

Sample Location	W10		W10-62		W10-72.4		W10-77.5	
min RMED	0.006	0.008	0.011	0.030	0.004	0.020	0.007	0.007
T_{RMED}	133	176	124	168	127	181	127	166
$T_{RMED-TSTATAV}$	0.00	0.33	0.67	2.00	0.33	0.67	0.33	1.00
T_{DT}	133.50	170.50	126.00	168.50	127.25	183.50	128.00	167.50
σ_{DT}	1.00	12.34	2.94	5.80	0.96	3.00	1.41	3.11
T-initiation	134	170	130	190	143	190	139	190
Gas Loss	0	0	0	0	0	0	0	0
Concentration factor	1.04	0.81	1	1.23	1.08	1.36	1.10	1.08
Mineral Suite	chalcedony, pargasite, montmorillonite-k, clinochlore-alf	quartz, anhydrite, heulandite, stilbite	chalcedony, lawsonite, albite-hi, beidellite-mg	quartz, anhydrite, laumontite	chalcedony, prehnite, phlogopite-na, albite-lo	quartz, celadonite, stilbite, carpholite-mg	chalcedony, prehnite, phlogopite-na, albite-lo	quartz, anhydrite, heulandite, celadonite

Table 10: (Continued)

Sample Location	W10-79.5		W10-82		W11		W12	
min RMED	0.005	0.007	0.011	0.006	0.007	0.004	0.070	0.007
T_{RMED}	127	168	139	164	48	92	99	145
$T_{RMED-TSTATAV}$	0.67	0.67	0.00	1.33	0.00	0.33	0.00	0.00
T_{DT}	128.50	167.00	139.50	165.50	48.25	91.50	98.50	145.33
σ_{DT}	1.73	4.00	1.29	1.29	0.50	1.00	3.00	0.58
T-initiation	151	170	110	170	65	78	100	94
Gas Loss	0	0	0	0	0	0	0	0
Concentration factor	1.09	1	1.2	1.02	3.3	9	7	7
Mineral Suite	chalcedony, prehnite, phlogopite-na, albite-lo	quartz, anhydrite, heulandite, stilbite	chalcedony, pargasite, microcline, phlogopite-na	quartz, anhydrite, heulandite, stilbite	chalcedony, clinoptilolite-na, beidellite-mg, clinozoisite	sanidine-hi, montmorillonite-ca, montmorillonite-mg, quartz	chalcedony, strontianite, beidellite-mg, clinozoisite	microcline, quartz, montmorillonite-mg

Table 10: (Continued)

Sample Location	**W14**		**180°**		**Iron Spring**		**No Tobacco Spring**	
min RMED	0.047	0.005	0.008	0.008	0.005	0.005	0.008	0.006
T_{RMED}	137	172	145	171	137	171	133	170
$T_{RMED\text{-}TSTATAV}$	2.00	0.67	1.00	0.67	0.33	0.33	1.00	1.00
T_{DT}	133.00	173.67	144.25	170.00	136.75	170.75	132.25	169.75
σ_{DT}	5.48	2.08	1.00	3.37	1.26	0.50	1.71	1.26
T-initiation	52	123	107	169	124	170	107	170
Gas Loss	0	0	0.003	0	0	0	0	0
Concentration factor	1.99	2.63	1.08	0.95	1.02	1	1	1
Mineral Suite	chalcedony, beidellite-k, phlogopite-f, anhydrite	quartz, sanidine-hi, albite-hi, anhydrite	beidellite-ca, microcline, montmorillonite-mg, chalcedony	quartz, anhydrite, heulandite, stilbite	chalcedony, pargasite, aragonite, microcline	quartz, anhydrite, heulandite, stilbite	chalcedony, cummingtonite, aragonite, phlogopite-f	quartz, anhydrite, heulandite, stilbite

Table 10: (Continued)

Sample Location	**Sulphur Spring**		**South Camp Spring**	
min RMED	0.009	0.004	0.014	0.009
T_{RMED}	136	168	138	168
$T_{RMED-TSTATAV}$	1.00	0.00	0.00	1.00
T_{DT}	136.25	168.50	139.75	169.00
σ_{DT}	1.50	1.00	2.06	5.72
T-initiation	122	169	118	135
Gas Loss	0	0	0	0
Concentration factor	1.05	0.98	1.13	1.09
Mineral Suite	chalcedony, aragonite, chloritoid-fe, microcline	quartz, anhydrite, heulandite, stilbite	chalcedony, sepiolite, chloritoid-fe, microcline	quartz, anhydrite, stilbite, aragonite

Table 10: Summary Statistics

		Mean	Median	Standard Deviation		Mean	Median	Standard Deviation
min RMED	Chalcedony mineral suites	0.010	0.008	0.011	Quartz mineral suites	0.020	0.008	0.041
T_{RMED}		133.688	134.000	5.805		169.813	170.500	6.833
$T_{RMED-TSTATAV}$		0.583	0.500	0.538		1.083	0.833	0.993
T_{DT}		133.906	134.000	5.380		170.398	169.875	6.445
σ_{DT}		1.848	1.455	1.323		3.804	3.240	2.994
T-initiation		114.563	120.000	28.930		159.500	170.000	30.279
Gas Loss		0.000	0.000	0.001		0.000	0.000	0.000
Concentration factor		1.530	1.065	1.663		1.253	1.005	0.626

Summary Statistics do not include results from W2, W11, or W12, as they do not appear to reflect thermal water.

4.2.3 RTEst

Multi-component geothermometry was also conducted using the program RTEst. The fundamental principles of the program are the same as GeoT. Both programs assess the speciation of a water's chemistry at various temperatures, calculate the saturation indices at those various temperatures, and compare some statistical measure of similarity between the saturation indices of a mineral assemblage to determine which temperature best reflects aquifer conditions. However, whereas GeoT conducts these calculations internally, RTEst uses the thermodynamic reaction capability of Geochemist's Workbench to assess the speciation and saturation indices, and has PEST determine parameter values that minimize the weighted sum of squares of the saturation indices. In this regard, there is no way to use RTEst without optimization, although the user can choose to optimize for temperature, CO_2-fugacity, the mass of water gained or lost, and/or the amount of mixing with another user-input water sample. The "total saturation index," which is included in RTEst output files, describes the square root of the objective function. The weighting option used for this report depends on each mineral's basis species and each species' assumed analytical uncertainty. The scheme takes the inverse of the square root of the sum of the squares of the analytical uncertainties of each basis species multiplied by its stoichiometric coefficient in order to create a weighting scheme that more strongly considers simple mineral formulas. For instance, an SiO_2 mineral has only one basis species (i.e. SiO_2) with an estimated uncertainty of 5.0%. The associated

weight would be 20 (i.e. $1/(\sqrt{[1*(0.05)^2]})$, as compared to a more molecularly complex clay mineral, which may have a weight close to 1. This approach helps to ensure that minerals with a large number of basis species or large analytical errors are not overly weighted in the optimization.

RTEst has a user interface that informs the mineral selection process by eliminating minerals based on rock type, temperature, and pH, and ensures that the constituents of the selected minerals do not violate the Gibb's phase rule, in order to make sure that each constituent is independent. Unfortunately, the user interface was not compatible with my computer, and this functionality was not utilized.

To help further narrow down the possible minerals, the saturation indices of the remaining minerals were evaluated at temperatures estimated by classic chalcedony and quartz geothermometers in Geochemist's Workbench. Figure 30 shows a plot of candidate minerals with their saturation index curves for W4 water chemistry.

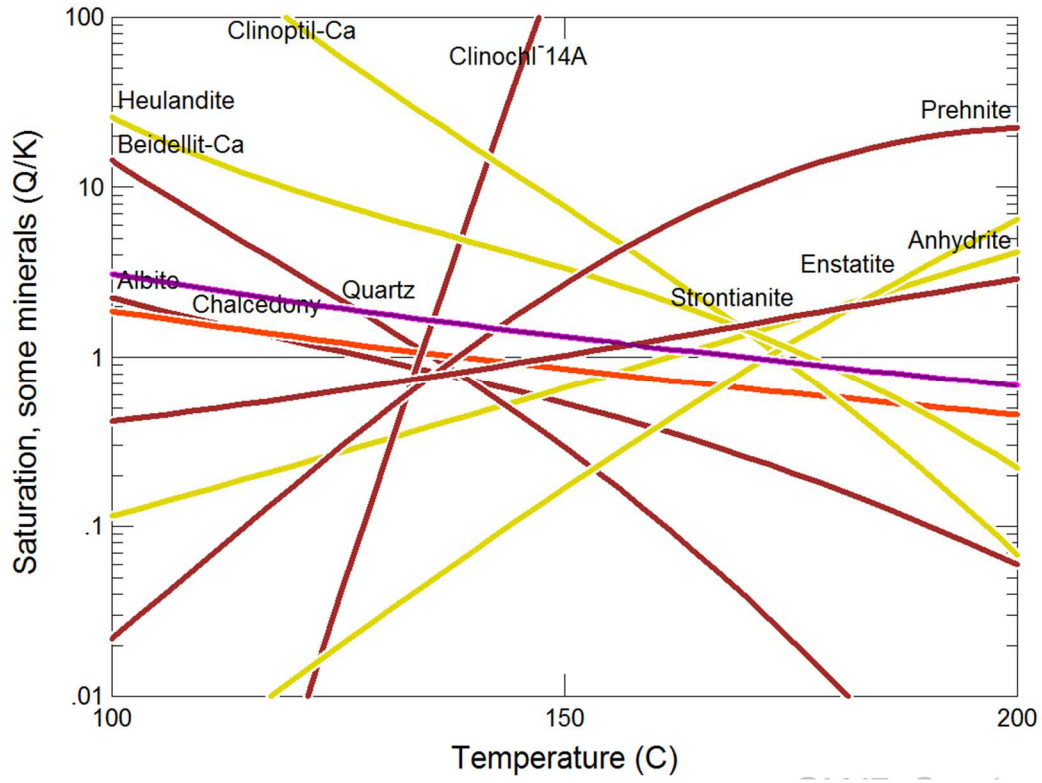

Figure 30: Geochemist workbench plot of mineral SIs versus temperature based on initial speciation of W4. Note the proximity of anhydrite, Ca-clinoptilolite, enstatite, and heulandite (all yellow) to the quartz curve (purple) and calcium beidellite, prehnite, strontianite, clinochlore and albite (all brown) to the chalcedony curve (orange).

` Using this initial estimate of likely mineral assemblages, a variety of mineral groups were attempted. The outputs from each attempt include a list of saturation index values for various minerals at the predicted reservoir temperature. This output file was visually examined for minerals with clustering saturation indices to further refine possible mineral combinations. Figure 31 shows a Geochemist's Workbench plot from an RTEst output using W3 water chemistry and the minerals quartz, anhydrite, laumontite,

and siderite. The associated equilibrium temperature is 174 ± 4.1 °C. The optimized log (fCO_2) is -0.709 which is an increase from the initial value of -1.615, indicating a loss of CO_2 between the reservoir and surface fluids (i.e. degassing during fluid ascent, observed in springs and at W14). The optimized dH_2O is -26.25 grams, a slight decrease in the mass of water, indicating a more concentrated reservoir fluid than the surface water (i.e. dilution of fluid during ascent).

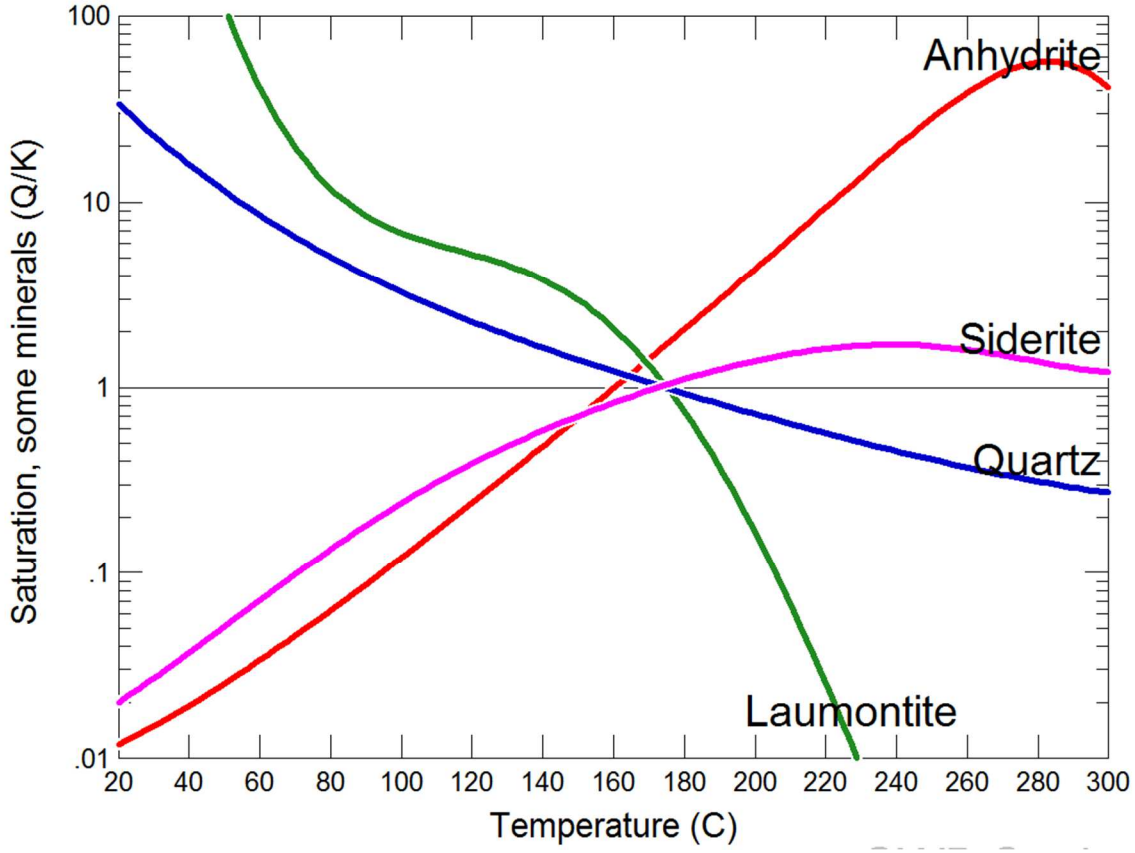

Figure 31: RTEst output for W3 water chemistry using anhydrite, laumontite, quartz, and siderite. Estimated temperature of 174 ± 4.1°C.

Figure 32 shows a Geochemist's Workbench plot of an RTEst output for W4 waters using calcium-beidellite, clinochlore, illite, and chalcedony showing a resultant temperature estimate of 138 ± 3.3 °C. The corresponding optimized fCO_2 was -0.73, an increase from the initial value, indicating gas loss during ascent. This sample was not optimized for dH2O, because adding an additional parameter for optimization resulted in an error of ±20 °C. A number of Breitenbush waters showed large increases in standard error when mineral assemblages that included chalcedony were selected for three parameter optimization.

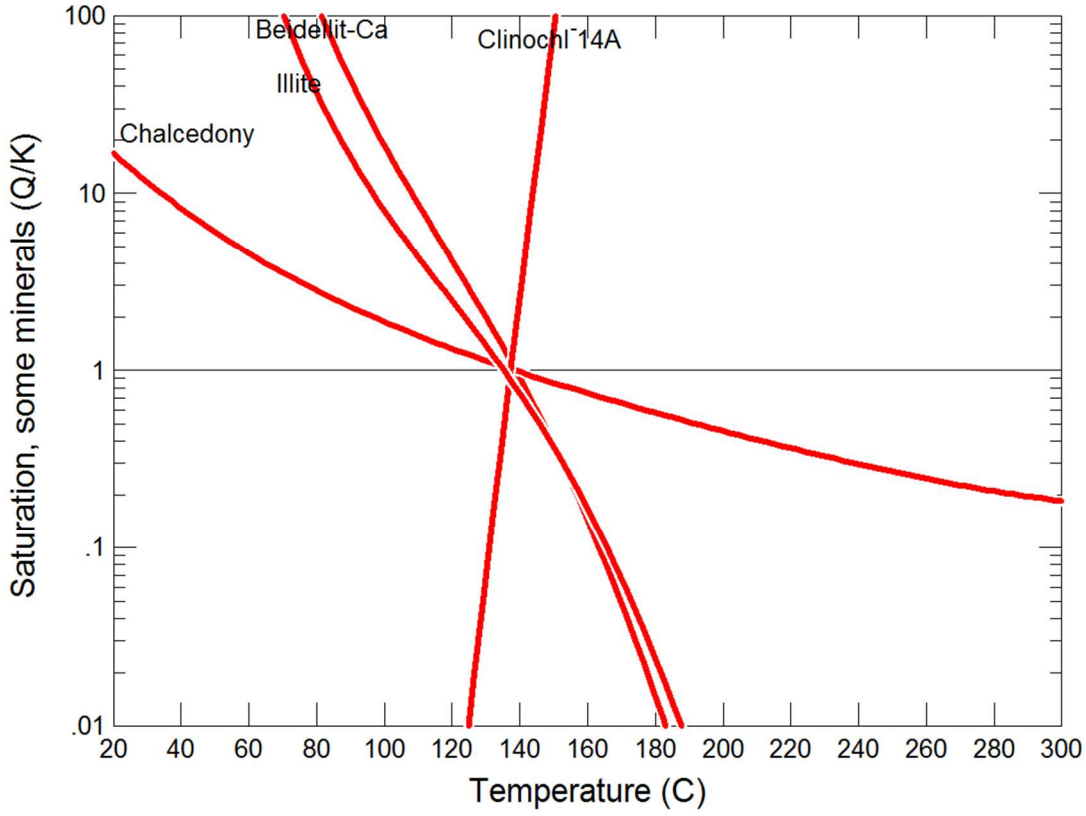

Figure 32: RTEst output using W4 water chemistry with the minerals chalcedony, illite, calcium-beidellite, and clinochlore. Optimized temperature is 138 ± 3.3 °C.

Table 11 shows the results of applying RTEst to each of the Breitenbush water samples. Good fits were not identified for the shallow waters (W2, W11, and W12) and a chalcedony mineral assemblage for W14 and are thus not present on the table. The median temperature estimate for chalcedony mineral assemblage was 131 with a standard deviation of 6.7. The median temperature estimate for the quartz mineral assemblage was 171 with a standard deviation of 6.0. The median log (fCO_2) for both assemblages indicates degassing of the reservoir during assent, though less pronounced for the

chalcedony assemblages when compared to the quartz assemblages. Similarly, both assemblages show an optimized reduction in water mass, indicating apparent dilution during ascent, though with more pronounced reduction in the quartz assemblages when compared to the chalcedony assemblages. Seven of the water samples were not optimized for three parameters with the chalcedony assemblage due to a large increase in standard error. Each sample was optimized for all three parameters using quartz assemblages.

Table 11: RTEst results for Breitenbush Hot Springs, including standard error, optimized parameters, objective functions, and mineral assemblages									
		W1		W3		W4		W10	
Temp	(°C)	137	173	139	174	138	165	123	163
Lower	(°C)	122.6	168.5	136.3	169.7	135.1	164.8	116.9	161.5
Upper	(°C)	150.8	177.5	141.9	177.9	141.8	166.2	128.6	164.6
S. Error	(°C)	14.1	4.5	2.8	4.1	3.3	0.7	5.9	1.6
log (fCO_2)		NO	3.60E-01	NO	-7.09E-01	-7.28E-01	-4.24E+00	-2.92E+00	-3.03E+00
dH_2O	kg	-1.21E-02	-6.75E-02	2.01E-02	-2.62E-02	NO	-2.68E-01	-1.39E-01	-2.83E-01
Total SI	unitless	7.42E-02	8.16E-02	1.46E-02	7.49E-02	6.14E-03	1.03E-02	4.68E-03	2.35E-02
Obj. Func	unitless	5.50E-03	6.66E-03	2.12E-04	5.61E-03	3.77E-05	1.07E-04	2.19E-05	5.51E-04
Mineral Suite		chalcedony, albite, strontianite	quartz, anhydrite, heulandite, paragonite	chalcedony, albite-lo, strontianite	quartz, siderite, anhydrite, laumontite	beidellite-ca, clinochlore-14A, chalcedony, illite	quartz, laumontite, anhydrite, strontianite	chalcedony, mordenite-na, sanidine-hi,	quartz, anhydrite, siderite, mordenite-k

Table 11: (Continued)

	W10-62		W10-72.4		W10-77.5		W10-79.5	
Temp	127.0	171	128.6	169	132	169	128	169
Lower	110.7	168.3	117.9	163.7	110.9	163.2	117.2	162.7
Upper	143.3	172.8	139.2	173.9	152.9	174.5	138.4	174.5
S. Error	16.3	2.3	10.6	5.1	21.0	5.7	10.6	5.9
log ($fCO_{2)}$	-1.15E+00	-6.63E-01	-1.26E+00	-6.95E-01	-1.11E+00	-6.90E-01	-1.11E+00	-7.19E-01
dH_2O	NO	-1.63E-01	-6.13E-02	-1.76E-01	-9.59E-02	-1.66E-01	-2.55E-02	-1.56E-01
Total SI	1.74E-01	4.23E-02	4.98E-02	9.24E-02	8.00E-02	1.02E-01	1.73E-02	1.07E-01
Obj. Func	3.01E-02	1.79E-03	2.48E-03	8.54E-03	6.40E-03	1.04E-02	3.01E-04	1.14E-02
Mineral Suite	chalcedony , clinochlore-7A, siderite	quartz, anhydrite, sepiolite, mordenite-k	chalcedony, prehnite, k-feldspar, witherite	quartz, anhydrite, sepiolite, heulandite	chalcedony, prehnite, phlogopite-na, albite-lo	quartz, anhydrite, sepiolite, siderite	chalcedony, prehnite, phlogopite-na, albite-lo	quartz, anhydrite, heulandite, siderite

Table 11: (Continued)

	W10-82		W14	180° Spring		Iron Spring	
Temp	119	169	150	139	172	125	173
Lower	109.8	167.0	137.3	138.5	170.5	121.4	171.7
Upper	127.7	171.2	163.6	139.3	173.4	127.9	174.6
S. Error	8.9	2.1	13.1	0.4	1.4	3.2	1.4
log (fCO_2)	-3.02E+00	-8.51E-01	9.54E-01	NO	-1.16E+00	1.51E-01	-6.00E-01
dH_2O	-1.58E-01	-1.27E-01	-4.19E-01	-5.11E-02	-7.16E-02	-1.22E+00	-9.97E-02
Total SI	2.46E-02	3.81E-02	2.33E-01	3.61E-03	2.60E-02	7.10E-03	2.61E-02
Obj. Func	6.05E-04	1.45E-03	5.41E-02	1.31E-05	6.75E-04	5.04E-05	6.82E-04
Mineral Suite	chalcedony, mordenite-k, clinoptilolite-ca, flourite	quartz, anhydrite, chamosite, witherite	quartz, sanididine-hi, albite-hi, anhydrite	chalcedony, laumontite, enstatite	quartz, anhydrite, heulandite chamosite	chalcedony, strontianite, mordenite-k, clinoptilolite-k	quartz, anhydrite, chamosite, enstatite

Table 11: (Continued)

	No Tobacco Spring		Sulphur Spring		South Camp Spring	
Temp	137	173	137	172	130	173
Lower	135.6	147.2	133.6	162.4	111.3	172.9
Upper	138.4	198.7	140.9	180.7	148.2	173.5
S. Error	1.4	25.7	3.6	9.1	18.5	0.3
log ($fCO_{2)}$	NO	4.60E-01	-7.61E-01	-6.28E-01	-1.96E+00	-9.12E-02
dH_2O	-4.83E-02	-9.74E-02	-1.50E-02	-5.65E-02	NO	-4.78E-01
Total SI	1.30E-02	4.70E-01	6.23E-03	1.64E-01	1.87E-01	5.86E-03
Obj. Func	1.68E-04	2.20E-01	3.88E-05	2.68E-02	3.49E-02	3.43E-05
Mineral Suite	chalcedony, enstatite, k-feldspar	quartz, anhydrite, aragonite, muscovite	chalcedony, clinoptilolite-k, mordenite-k, strontianite	quartz, anhydrite, chamosite, siderite	chalcedony, sepiolite, chloritoid-fe, microcline	quartz, anhydrite, enstatite, magnesite

Table 11: Summary Statistics

	Chalcedony	Mean	Median	Standard Deviation	Quartz	Mean	Median	Standard Deviation
Temp		131	131	6.69		169	171	5.98
Lower		122.7	119.7	10.9		163.4	164.8	9.5
Upper		139.9	140.1	7.9		174.5	173.9	8.2
S. Error		8.6	7.4	6.7		5.5	4.1	6.6
log (fCO_2)		-1.39E+00	-1.13E+00	9.86E-01		-8.20E-01	-6.90E-01	1.30E+00
dH_2O		-1.65E-01	-5.11E-02	3.56E-01		-1.77E-01	-1.56E-01	1.32E-01
Total SI		4.73E-02	1.60E-02	6.18E-02		9.97E-02	7.49E-02	1.20E-01
Obj. Func		5.77E-03	2.57E-04	1.16E-02		2.33E-02	5.61E-03	5.64E-02

NO = Not optimized. If a parameter value has this note, it suggests that a reasonable range of temperatures could not be constrained using sufficient minerals to optimize an

4.2.3.1 Mixing

In addition to the three parameters optimized above, mixing between select thermal signature waters (W1, W3, Sulphur Spring, and 180° Spring) and W12 was optimized using RTEst. Table 12 shows a comparison of mixing results with unmixed results. Mixing was done with the same quartz mineral assemblage as was determined in the preceding section. In this case, only temperature, log(fCO_2) and "react times" (essentially mixing mass) were optimized, as mixing essentially incorporates change in water mass, and when dH_2O and mixing were optimized synchronously, it generally led to a large range of possible temperatures (high standard error). Temperature estimates using the mixing parameter were similar to those using dH_2O. In both cases, temperature estimates using one parameter were within the range of error of those using the other.

Table 12: Results of using the RTEst mixing module on select Breitenbush waters. Also shown are the results of optimizing for change in water mass for ease of comparison between the two parameters.

	Temp	Lower	Upper	S. Error	log ($fCO_{2)}$	DH_20	React Times	Total SI	Obj. Func
	(°C)	(°C)	(°C)	(°C)		kg	unitless	unitless	unitless
W1 Mixing	172	169.9	175.0	2.6	3.21E-01	NO	-7.84E-02	4.60E-02	2.11E-03
W1 dH_2O	173	168.5	177.5	4.5	3.60E-01	-6.75E-02	NO	8.16E-02	6.66E-03
W4	166	163.3	168.3	2.5	-3.93E+00	NO	-2.42E-01	3.91E-02	1.53E-03
W4 dH_2O	165	164.8	166.2	0.7	-4.24E+00	-2.68E-01	NO	1.03E-02	1.07E-04
Sulphur	171	166.0	176.1	5.0	-6.74E-01	NO	-6.74E-02	8.75E-02	7.66E-03
Sulphur dH_2O	174	169.7	177.9	4.1	-7.09E-01	-2.62E-02	NO	7.49E-02	5.61E-03
180° Mixing	171	170.3	172.4	1.1	-1.20E+00	NO	-8.29E-02	1.93E-02	3.73E-04
180° dH_20	172	170.5	173.4	1.4	-1.16E+00	-7.16E-02	NO	2.60E-02	6.75E-04

4.2.3.2 Parameter Sensitivity

Using 180° Spring water chemistry and a mineral assemblage consisting of quartz, anhydrite, chamosite, and heulandite, each combination of parameters was optimized to assess temperature estimates and error using each parameter. Temperature was always optimized. Table 13 lists the results of each combination of parameters and the mineral assemblage. Each set of parameter combinations results in slightly different standard error and objective functions. However, the actual temperature estimate is more or less the same, ranging from 171 to 173 °C. As mentioned in the previous section, using dH_2O and mixing results in a large temperature range. Using all four parameters resulted in an estimate of 173 ±18.1 °C, though this run includes a fifth mineral (pseudowollastonite) in order to constrain the confidence interval.

Table 14 shows the same data, but with an equal weighting scheme for all minerals. In this case, the estimates for temperature and temperature plus CO_2-fugacity are 10 °C less than with the original weighting scheme. All other temperature estimates are within 2 °C of those listed in Table 13. The standard error is larger for the equal weighting scheme, with the exception of the run during which all four parameters are simultaneously assessed. This is likely due to the fact that in the original weighted scheme, after PEST has preferentially optimized parameters for quartz, any adjustments away from these parameters will have a stronger effect on the objective function than if it was not weighted, and the confidence interval will become closer to these values as a

result. The standard error of the estimate optimizing for temperature, dH_2O and mixing is 92.7 °C, and the temperature estimate of 173 °C is likely a product of the initial guess (173 °C for all of the runs). The Total SI and objective functions are less for the equal weighting scheme, but this is simply due to the fact that they are not multiplied by weighting coefficients before being summed and does not imply a better fit. In general, it appears that the weighting scheme used by RTEst provides better constrained results than if it simply regarded each mineral equally.

Table 13: A comparison of the results of each combination of RTEst optimization parameters. All runs used 180° spring chemistry and a mineral assemblage of quartz, anhydrite, chamosite, and heulandite. In addition, the run with all four parameters included psuedowollastonite.

	Temp	Lower	Upper	S. Error	log (fCO_2)	DH_20	React Times	Total SI	Obj. Func
	(°C)	(°C)	(°C)	(°C)		kg	unitless	unitless	unitless
Temperature only	172	164.5	179.6	7.5	NO	NO	NO	9.52E-01	9.07E-01
Temp. and log(fCO_2)	172	159.9	184.3	12.2	-1.16E+00	NO	NO	9.31E-01	8.68E-01
Temp. and dH_2O	172	170.3	173.6	1.7	NO	-7.25E-02	NO	1.26E-01	1.60E-02
Temp. and mixing	171	170.1	172.5	1.2	NO	NO	-8.38E-02	9.06E-02	8.20E-03
Temp.,log(fCO_2), and dH_2O	172	170.5	173.4	1.4	-1.16E+00	-7.16E-02	NO	2.60E-02	6.75E-04
Temp.,log(fCO_2), and mixing	171	170.3	172.4	1.1	-1.20E+00	NO	-8.29E-02	1.93E-02	3.73E-04
Temp., dH_2O, and mixing	172	126.9	217.9	45.5	NO	-1.00E+00	6.40E-02	1.48E-01	2.19E-02
Temp.,log(fCO_2), dH_2O, and mixing	173	155.2	191.3	18.1	-1.06E+00	-2.69E-01	1.75E-01	8.13E-02	6.62E-03

NO = not optimized.

Table 14: A comparison of the results of each combination of RTEst optimization parameters with equal weights for all minerals. All runs used 180° spring chemistry and a mineral assemblage of quartz, anhydrite, chamosite, and heulandite. In addition, the run with all four parameters included psuedowollastonite.

	Temp	Lower	Upper	S. Error	log (fCO_2)	DH_20	React Times	Total SI	Obj. Func
	(°C)	(°C)	(°C)	(°C)		kg	unitless	unitless	unitless
Temperature only	162	147.0	177.9	15.5	NO	NO	NO	2.12E-01	4.49E-02
Temp. and log(fCO_2)	163	137.2	188.0	25.4	-1.28E+00	NO	NO	2.09E-01	4.38E-02
Temp. and dH_2O	172	156.6	187.8	15.6	NO	-7.21E-02	NO	8.65E-02	7.48E-03
Temp. and mixing	172	161.0	182.4	10.7	NO	NO	-8.56E-02	6.21E-02	3.85E-03
Temp.,log(fCO_2), and dH_2O	172	169.9	173.9	2.0	-1.15E+00	-7.45E-02	NO	2.66E-03	7.10E-06
Temp.,log(fCO_2), and mixing	171	169.8	172.7	1.4	-1.19E+00	NO	-8.54E-02	1.96E-03	3.85E-06
Temp., dH_2O, and mixing	173	80.3	265.7	92.7	NO	-1.00E+00	6.42E-02	1.01E-01	1.02E-02
Temp.,log(fCO_2), dH_2O, and mixing	172	168.2	176.0	3.9	-1.12E+00	-9.99E-01	6.52E-02	7.43E-03	5.52E-05

NO = not optimized.

4.2.3.3 RTEst Utilizing the GeoT Database

In order to compare the outputs of RTEst and GeoT, I attempted to reproduce the database I used for GeoT (SOLTHERM) in a format recognizable to Geochemist's Workbench. Unfortunately, GeoT reads the coefficients used to generate temperature dependent equilibrium constants and Geochemist's Workbench only allows input of the constants themselves. The program reads the constants and calculates its own best-fit coefficients internally. Due to this inconsistency, some minerals were able to translate between the programs and some were not. Figure 33 shows an optimized output using W1 water for GeoT and RTEst for the mineral assemblage anhydrite, quartz, calcite, and heulandite optimized in both cases for water loss, steam weight fraction, and temperature. The GeoT temperature estimate is 174 °C and the RTEst temperature estimate is 175 °C. However, the shape of the curves is inconsistent between the two plots, even though they are both ostensibly using the same database.

Table 15 shows the effect that using the SOLTHERM database has on parameter sensitivity for minerals estimated using RTEst (again for 180 °C water using quartz, anhydrite, chamosite, and heulandite). The estimated temperatures are relatively close to those listed in Tables 13 and 14; however, this is largely a product of the initial guess value used for all three tables (173 °C). The standard errors range from 44.3 °C when optimizing for temperature only to 877.3 °C when optimizing for all four parameters. In addition, the suggested change in water volume and mixing rates show positive values,

which implies a concentration of fluid during ascent in contrast to all of the other estimates of Breitenbush Hot Spring behavior. These data further indicate a disagreement between the two databases, or the manner in which Geochemist's Workbench interprets the logK values provided.

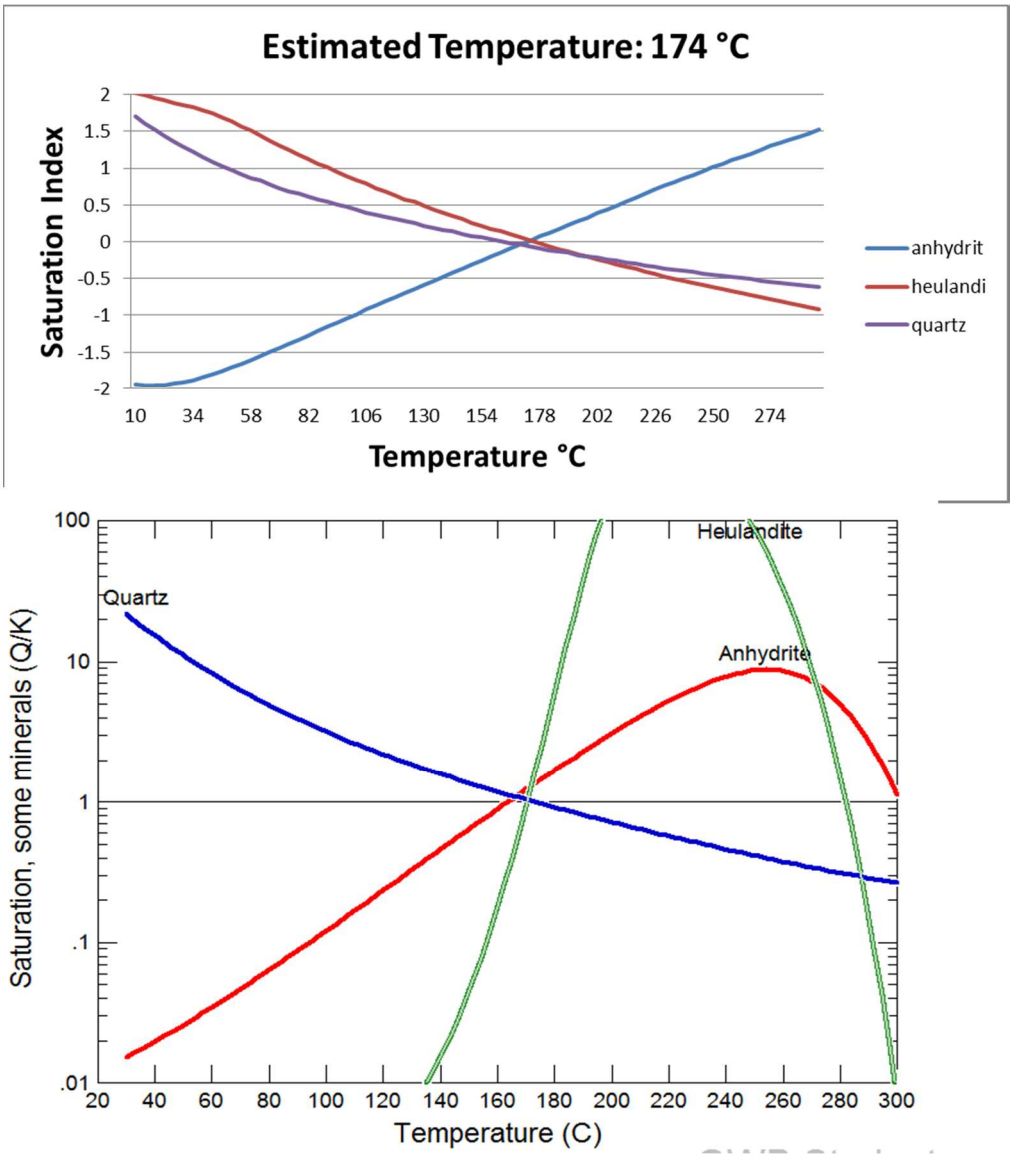

Figure 33: GeoT and RTEst outputs using W1 water, optimizing for temperature and dilution/concentration with pure water. A similar temperature estimate, but quite different curves.

Table 15: A comparison of the results of each combination of RTEst optimization parameters using the SOLTHERM database. All runs used 180° spring chemistry and a mineral assemblage of quartz, anhydrite, chamosite, and heulandite. In addition, the run with all four parameters included psuedowollastonite.

	Temp	Lower	Upper	S. Error	log (fCO_2)	DH_20	React Times	Total SI	Obj. Func
	(°C)	(°C)	(°C)	(°C)		kg	unitless	unitless	unitless
Temperature only	177	132.6	221.2	44.3	NO	NO	NO	5.86E+00	3.43E+01
Temp. and log(fCO_2)	173	93.7	252.6	79.4	-3.44E+00	NO	NO	5.42E+00	2.94E+01
Temp. and dH_2O	177	114.1	240.3	63.1	NO	2.62E-01	NO	5.07E+00	2.57E+01
Temp. and mixing	179	115.2	243.2	64.0	NO	NO	3.40E-01	4.97E+00	2.47E+01
Temp.,log(fCO_2), and dH_2O	177	-129.0	483.0	306.0	-1.41E+00	2.64E-01	NO	5.06E+00	2.56E+01
Temp.,log(fCO_2), and mixing	179	-177.5	536.1	356.8	-1.23E+00	NO	3.50E-01	4.97E+00	2.47E+01
Temp., dH_2O, and mixing	176	-324.5	676.4	500.4	NO	-1.00E+00	-2.09E-01	5.15E+00	2.65E+01
Temp.,log(fCO_2), dH_2O, and mixing	204	-673.0	1081.7	877.3	-4.21E-03	1.90E-01	1.00E+01	4.13E+00	1.71E+01

NO = not optimized.

4.2.3.4 RTEst Using a Single Mineral Assemblage

In addition to the independent runs exhibited in Table 11, RTEst was also applied to all of the Breitenbush thermal water samples using a common mineral assemblage in order to develop a model of reservoir conditions consistent between points. Samples from W11 and W12 were not included due to their apparent influence from a separate water source (Sections 4.1 and 4.2.1). Samples from W2 and W14 were not included because of differences between their chemistries and the other thermal water samples that may be the result of mineral precipitation during ascent (Section 4.1). Results were compared to the saturation states of minerals observed in the nearby geothermal wells (Table 2). The quartz mineral assemblages included in Table 11 showed undersaturation of chalcedony, which was commonly observed throughout the borings. In contrast, the chalcedony mineral assemblages showed supersaturation of quartz (also commonly observed), and thus both minerals could be explained by chalcedony equilibrium. In this regard, mineral assemblages that included chalcedony or that resulted in reservoir conditions showing supersaturation of chalcedony were preferred to those using quartz. A number of mineral assemblages were attempted.

It was observed that samples with similar Al concentrations were capable of attaining consistent estimates of reservoir conditions, but that samples with contrasting Al concentrations did not provide similar estimates. The well samples generally had much higher Al values than the springs, possibly due to Al present as colloidal particles from

well materials that were smaller than the filters used for the collection of cation samples (i.e. smaller than 0.45 um) or dissolved Al from well materials. The time-series pumping of W10 showed a decrease in Al with time, which may have been due to the gradual removal of these particles from the well as it was purged. W14 shows the highest Al concentration of any of the Breitenbush Hot Spring samples. This well was filled with rocks and could not be properly purged before sampling, further suggesting that high Al concentrations may be related to insufficient well purging. Another possibility is that the spring samples showed low concentrations of Al due to near surface precipitation of Al bearing minerals, including co-precipitation with iron oxides resulting from the oxidation of Fe^{2+} near the surface. Due to this uncertainty, the Al concentrations for each sample were generated by assuming equilibrium with K-feldspar as per the fix-Al method of Pang and Reed (1998).

The most promising mineral suite consisted of chalcedony, heulandite, mordenite-K, and calcite. Table 16 shows the resultant saturation indices of minerals that were observed in nearby geothermal borings and that were present in the thermodynamic database thermo.tdat for each water sample using this assemblage. Included on Table 16 is the uncertainty of saturation index estimation, which is related to the analytical uncertainty of each of its component species and is calculated using the methods described in Palmer (2014). Most of the minerals show equilibrium or supersaturation. Laumontite and analcime both show apparent undersaturation. However, In the case of laumontite, the average saturation index for laumontite is -0.34, which is well within the

range of uncertainty for laumontite saturation (~1.1 standard deviations below saturation). Analcime is clearly undersaturated (by >3.5 standard deviations). However, this could be due to deviations from ideal stoichiometry as analcime can have significant variations in Na, Al, and Si contents (Neuhoff et al., 2004).

In addition to minerals identified in nearby borings, Table 16 includes calculated SIs for muscovite, fluorite, and petalite. Although muscovite was not described, it is included as a proxy for celadonite, with which it forms a solid-solution series and which was not present in the chosen thermodynamic database. Flourite is in equilibrium with the chosen assemblage and may control F- in the system, which ranges from 3.2 to 3.7 mg/L among the samples included in Table 16. Petalite is also in equilibrium with the assemblage and may control Li in the system. Li ranges from 1.6 to 2.6 mg/L among samples included in Table 16.

Table 17 shows the estimated pH, charge balance error, temperature, log CO_2 fugacity, and estimated Al concentration for each sample using a chalcedony, heulandite, mordenite-K, and calcite mineral suite and deriving Al from equilibrium with K-feldspar. Optimization was conducted on CO_2 fugacity and temperature. When also optimizing for dH_2O, the resulting reservoir estimates were similar with a large increase in uncertainty and close to zero change in water mass. This suggests that there was not significant loss or gain of water during ascent and that optimization with dH_2O caused an unnecessary over-parameterization of the system, and optimization for dH_2O was therefore excluded. Temperature estimates ranged from 130 to 141 °C, with a mean of 136 ±3 °C. The

sample collected from W10 yielded an estimate 5 °C lower than the next coolest estimate. This well may have been influenced by mixing with a shallower aquifer, as recorded in the temperature gradient log (Waibel, 1983). Excluding this well, temperature estimates ranged from 135 to 141 °C, with a mean of 137 ±2 °C.

Estimates of reservoir log CO_2 fugacity ranged from -5.54×10^{-3} to -1.14×10^{-1}, all of which are greater than the surface water log CO_2 fugacity values, which ranged from -2.36 to -1.47, suggesting that CO_2 was lost during ascent at each of the sample locations. Estimates of pH showed consistency between sampling points within 0.2 pH units. Absolute values of calculated charge balance errors were less than 3% for all samples. The Al concentrations from assumed equilibrium with K-feldspar were also consistent between sample locations. Values ranged from 9.1 to 11 ppb, with a mean of 9.95 ppb. This value is between the average measured Al value for the wells (11.5 µg/L) and the springs (5.9 µg/L) and is close to the value measured from 180° Spring (8.8 µg/L). Isotopic data suggests that 180° Spring may have the greatest contribution from andesitic water (Section 4.1, Figures 16 and 17). Figure 34 is a graphical representation of the temperature, log CO_2 fugacity, and pH results. Standard deviations calculated from PEST are included in the temperature and log CO_2 fugacity displays.

Table 16: Saturation states from Geochemist's Workbench/RTEst outputs using a mineral assemblage consisting of chalcedony, mordenite-K, calcite, and heulandite. Listed minerals were both observed in nearby geothermal boreholes and are included in the geochemical database thermo.tdat.

Mineral	W1	W3	W4	W10-82	180°	Iron	No Tobac	Sulphur	South Camp	Mean	SD	SI Uncertainty
Calcite	0.00	0.00	0.00	0.00	0.00	0.00	0.00	0.00	0.00	0.00	0.00	0.11
Chalcedony	0.00	0.00	0.00	0.00	0.00	0.00	0.00	0.00	0.00	0.00	0.00	0.02
Mordenite-K	0.16	0.16	0.16	0.16	0.16	0.15	0.16	0.16	0.16	0.16	0.00	0.22
Heulandite	0.09	0.24	0.14	0.09	0.25	0.08	0.10	0.15	0.10	0.14	0.07	0.30
Analcime	-0.79	-0.75	-0.78	-0.71	-0.78	-0.81	-0.80	-0.77	-0.74	-0.78	0.02	0.21
Beidellite-K	-0.01	0.18	0.09	-0.01	0.25	0.00	0.01	0.23	0.11	0.10	0.10	0.29
Beidellite-Mg	0.60	0.81	0.69	0.60	0.86	0.63	0.63	0.87	0.76	0.72	0.11	0.29
Clinoptilolite-Ca	0.68	0.84	0.73	0.73	0.85	0.67	0.76	0.32	0.69	0.69	0.16	0.31
Clinoptilolite-K	0.32	0.34	0.33	0.33	0.33	0.32	0.32	0.32	0.32	0.33	0.01	0.31

Table 16: (continued)

Mineral	W1	W3	W4	W10-82	180°	Iron	No Tobac	Sulphur	South Camp	Mean	SD	SI Uncertainty
Epidote	1.21	1.32	1.18	1.21	0.89	1.43	1.76	1.23	2.05	1.36	0.35	0.37
Goethite	2.07	2.14	2.08	2.07	1.73	2.31	2.62	2.22	3.01	2.25	0.37	0.17
Illite	0.15	0.27	0.18	0.15	0.30	0.18	0.19	0.34	0.29	0.23	0.07	0.30
Kaolinite	0.40	0.57	0.49	0.40	0.66	0.42	0.43	0.64	0.53	0.51	0.10	0.26
Laumontite	-0.38	-0.29	-0.36	-0.38	-0.23	-0.37	-0.36	-0.32	-0.36	-0.34	0.05	0.30
Quartz	0.20	0.20	0.20	0.20	0.20	0.20	0.20	0.20	0.20	0.20	0.00	0.02
Muscovite[a]	1.14	1.31	1.23	1.14	1.39	1.16	1.16	1.38	1.26	1.24	0.10	0.34
Flourite[b]	-0.09	-0.11	-0.13	-0.09	0.06	-0.13	-0.12	-0.09	-0.11	-0.09	0.06	0.04
Petalite[b]	0.05	-0.07	-0.08	0.05	0.07	0.04	0.03	0.05	0.38	0.06	0.13	0.30

a = Muscovite was not identified in nearby borings. It is used here as a proxy for celadonite, which was described in nearby borings, but which was not in the geothermal database.

b = Flourite and petalite were not identified in nearby borings. They are included here due to their apparent equilibrium conditions, which would explain the consistency of F (flourite) and Li (petalite) in Breitenbush thermal water samples.

Table 17: Estimated Breitenbush reservoir conditions from Geochemist's Workbench/RTEst outputs using a mineral assemblage consisting of chalcedony, mordenite-K, calcite, and heulandite.

Sample Location	pH	Charge Balance Error	Temp (°C)	Temp SD	log[f(CO2)]	log[f(CO2)] SD	Measured Al (ug/L)	Calculated Al (ppb)
W1	6.09	0.70%	136.77	3.89	-1.18E-01	0.15	14	9.1
W3	6.00	-0.53%	140.85	5.65	-5.54E-03	0.24	16	10
W4	6.04	-2.44%	138.94	4.36	-3.04E-03	0.17	12	9.4
W10- 82	6.08	0.31%	129.62	3.64	-1.14E-01	0.15	4.1	11
180°	5.97	-0.17%	136.80	5.56	-2.79E-03	0.22	8.8	11
Iron	6.11	0.41%	134.88	3.77	-1.55E-01	0.15	6.1	9.2
NoTobac	6.11	0.78%	135.30	3.89	-1.51E-01	0.15	6.2	9.3
Sulphur	5.99	-0.17%	136.60	4.44	5.50E-03	0.18	4.7	11
South Camp	6.05	1.47%	135.38	3.91	-5.07E-02	0.15	3.6	9.8
Mean	6.05	0.78%	136.13	4.35	-0.07	0.17	8.39	9.95
SD	0.053	0.011	3.090	0.759	0.068	0.034	4.577	0.743
Mean w/out W10	6.04	0.83%	136.94	4.43	-0.06	0.18	8.93	9.81
SD w/out W10	0.056	0.012	2.028	0.760	0.070	0.035	4.581	0.659

SD = standard deviation

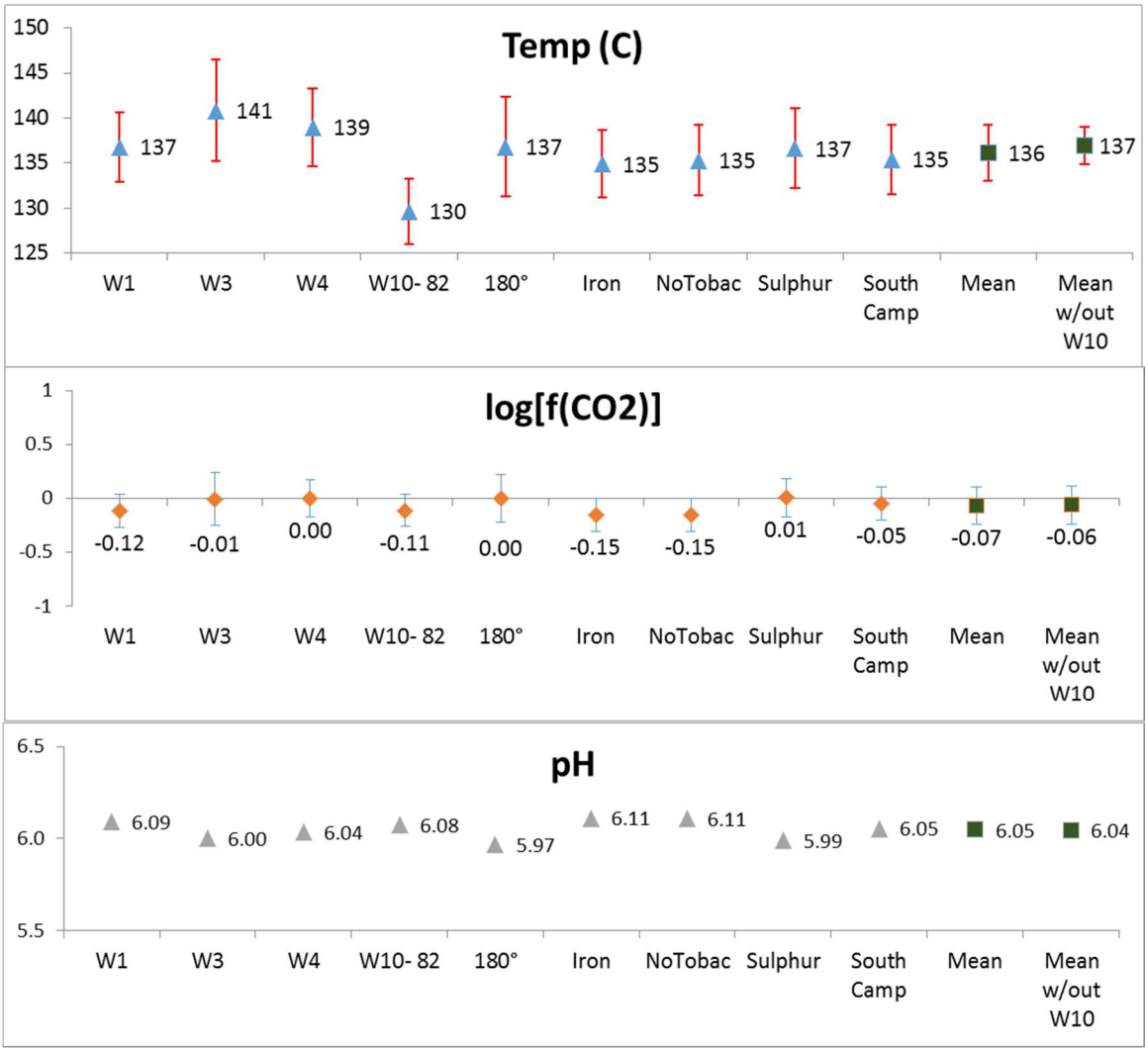

Figure 34: Temperature, log fCO2, and pH estimates from RTEst outputs for thermal springs and wells at Breitenbush using a mineral assemblage consisting of mordenite-K, chalcedony, heulandite, and calcite.

4.2.4 Discussion

There is good agreement between the temperature estimates from the quartz mineral assemblages of GeoT and RTEst, and the median of estimates of the Na-K and quartz classical geothermometers with estimates ranging from 169 to 175 °C. Similarly, there is agreement between the chalcedony geothermometer and multi-component estimates using a chalcedony mineral assemblage, with estimates ranging from 130 to 140°C.

Using RTEst with a chalcedony, mordenite-K, calcite, and heulandite mineral assemblage and deriving Al concentrations from assumed equilibrium with K-feldspar resulted in an average estimate of 137 ±2 °C. This estimate shows promise in its consistency in estimated reservoir CO_2 fugacity and pH (Table 17; Figure 34) and that many of the minerals observed in samples collected during drilling of nearby geothermal wells can be explained by equilibrium or supersaturation (Table 16). The mineral assemblages containing quartz show undersaturation of chalcedony, which was frequently observed in the geothermal wells. In addition, the estimates using quartz mineral assemblages relied upon equilibrium between quartz and anhydrite. Although anhydrite was observed in samples obtained from boreholes drilled in the area, pyrite and chalcopyrite were much more frequently described, suggesting that sulfate reducing conditions exist in the subsurface that would preclude anhydrite equilibrium.

All four of the minerals used in the assemblage were identified in both the CTGH-1 and SUNDECO borings (Table 2; Figure 4; Bargar, 1994; Bargar, 1988). Calcite and heulandite were also identified during drilling of W10 (Table 2; Waibel, 1983). Regarding the occurrence of mordenite, Bargar states that, "mordenite is a late hydrothermal mineral deposited in open spaces of fractures and vugs together with heulandite and chalcedony" (Bargar, 1994). The chosen assemblage may thus represent the current geothermal system. The use of K-feldspar to derive Al concentrations has been applied in many other multi-component geothermometry investigations, including at Breitenbush Hot Springs by Spycher (2016). In addition, adularia was reported in a sample collected from CTGH-1 at a depth of 1,293 m (Bargar, 1988), showing that it is present in the geothermal system.

Minerals identified in the SUNEDCO drillhole that did not show supersaturated conditions using chalcedony, mordenite-K, calcite, and heulandite include analcime and laumontite. The former was found in only a few of the core samples. The latter was found consistently at depths between 768 and 1,981 meters (Bargar, 1994). However, as described in Section 4.2.3.4, laumontite is within the range of equilibrium conditions when the uncertainty in estimating its saturation index is accounted for. It may have also formed prior to the present hydrothermal system. Bargar states that "SEM studies indicate that laumontite formed later than quartz, mixed-layer chlorite-smectite, and siderite and was deposited earlier than smectite and heulandite."

Past reservoir temperature estimates range from 174 to 180 °C (Forcella, 1982; Ingebritsen et al., 1992; Pang and Reed, 1998; Spycher et al., 2016) . These are consistent (if slightly higher) than the median quartz assemblage temperatures determined with GeoT and RTEst, but much higher than the chalcedony, heulandite, mordenite-K, and calcite temperature estimate of 137 °C. The previous multi-component geothermometry applications at Breitenbush relied on mineral assemblages that were not necessarily observed in the subsurface (Pang and Reed, 1998; Spycher et al., 2016). In both studies, Al concentrations were generated by assumed equilibrium with a feldspar. However, because of the other minerals used to generate temperature estimates (in particular quartz and anhydrite) the resultant Al concentrations were much higher. Pang and Reed (1998) describe a reservoir estimate of 180 °C for Breitenbush Hot Springs by forced equilibrium with albite, coincident with quartz and anhydrite equilibrium. This would necessitate an Al concentration of 0.6 to 0.7 x 10^{-5} mol/kg (using GeoT's built-in FixAl feature). Similarly, Spycher et al. (2016) use forced equilibrium with microcline at quartz and anhydrite equilibrium to generate a temperature of 176 °C , which would result in Al concentrations of 0.3 to 0.5 x 10^{-5} mol/kg. These estimates are two orders of magnitude greater than the measured and predicted concentrations during this study. In addition to these studies, other previous estimates involved assessing equilibrium with anhydrite as a reliable method for estimated reservoir temperature in the Cascades (Ingebritsen, 1992; Mariner, 1993). As described above, the reliance on anhydrite does not reflect the

apparently reduced subsurface conditions suggested by the frequent occurrence of sulfide minerals.

The maximum recorded borehole temperature from the SUNEDCO well of 141 °C (Bargar, 1994) is consistent with estimates based on chalcedony mineral assemblages, and not the quartz-based assemblages used in previous studies. An estimated reservoir temperature close to 140 °C is also consistent with fluid inclusion data from the SUNEDCO well, which showed a good correlation between measured borehole depth and fluid inclusion temperature (Bargar, 1994). As mentioned in Section 2.1.1.5, Arnórsson (2000) recommended as a general rule of thumb that for temperatures less that 180 °C, the chalcedony geothermometer of Fournier (1977) should be applied. The median estimate for thermal water samples from Breitenbush using this geothermometer is 135 °C.

4.3 Wind River Geothermometry

4.3.1 Classical Geothermometry

Geothermometry estimates for the four samples collected from the Wind River hot springs yielded lower temperatures than Breitenbush Hot Springs. As evident in Table 9, few of the classic geothermometry estimates have values in excess of 100 °C. Figures 35 and 36 shows each of the considered classical geothermometers applied to St Martin's Hot Spring and Shipherd's Hot Spring, respectively. The difference between ion

concentrations are generally within the range of analytical uncertainty between the two St. Martin's samples and between the two Shipherd's samples, and each will be treated as a single source. In particular, St Martin's Well sample (collected closer to the source) and the upstream Shipherd's sample (slightly higher concentrations) are those chosen for this analysis.

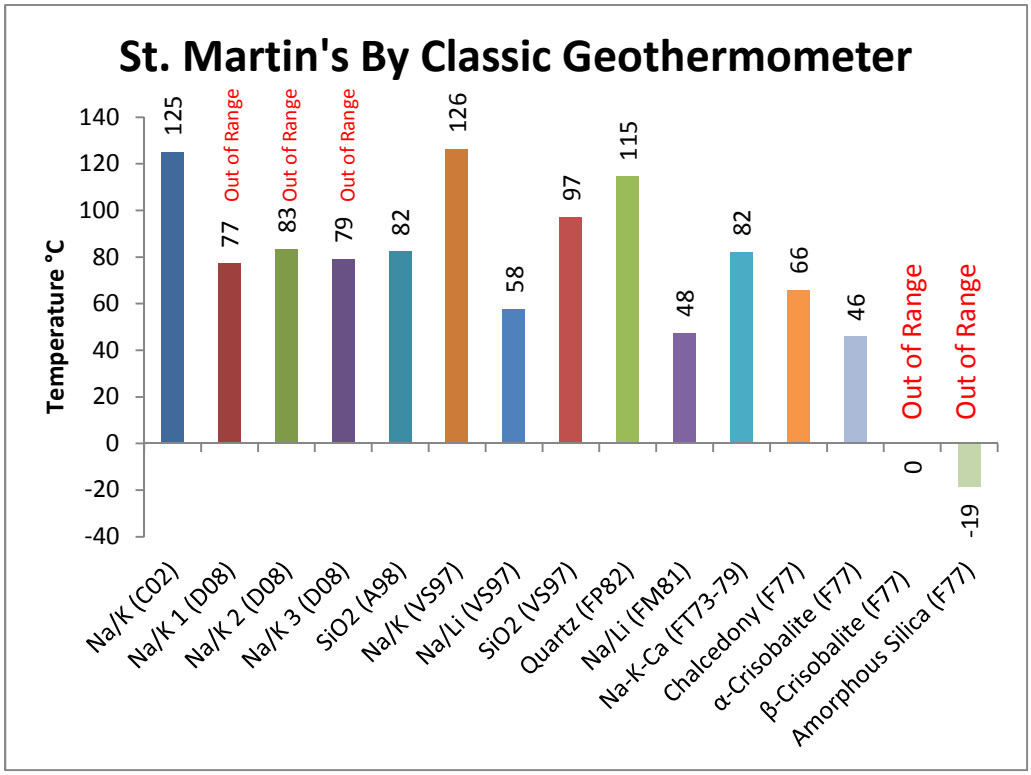

Figure 35: St. Martin's Hot Spring by classical geothermometer.

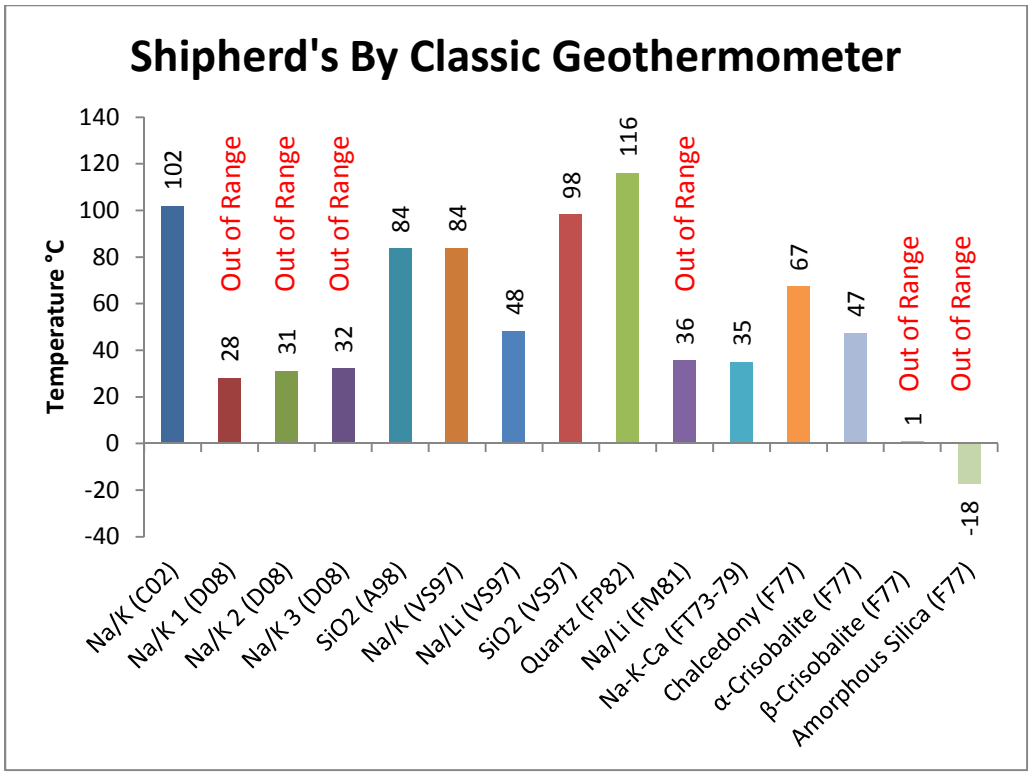

Figure 36: Shipherd's Hot Spring by classical geothermometer.

4.3.2 GeoT

As with the Breitenbush samples, the initial mineral selection process for GeoT was to allow it to generate the closest fit based on all the minerals in its database. The resultant plot for St. Martin's Hot Spring is depicted as Figure 37, and shows good agreement among saturation index curves at 89 °C. Figure 38 shows the plots for the same procedure applied to Shipherd's Hot Spring. For Shipherd's Hot Spring, the

temperature estimate was 71 °C. The curves for several of the minerals were quite flat for these plots. Neither initial input included a free-silica mineral.

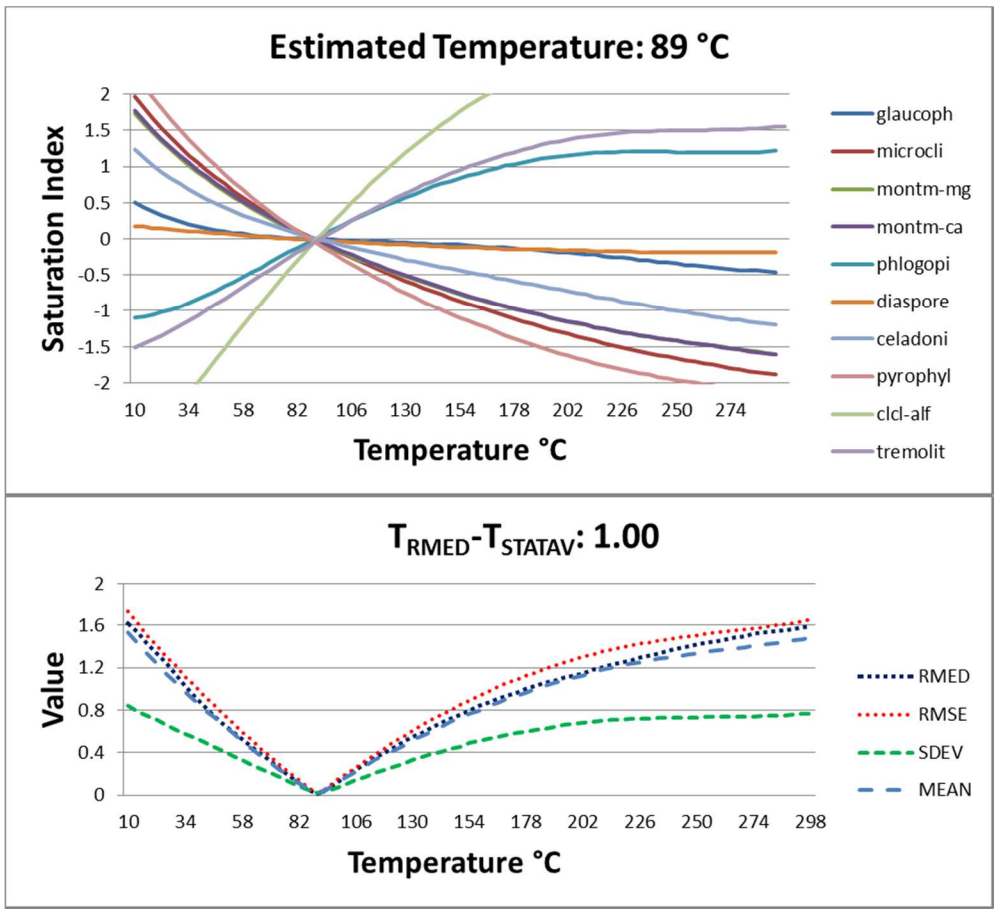

Figure 37: GeoT output using the chemistry of St. Martin's Hot Springs.

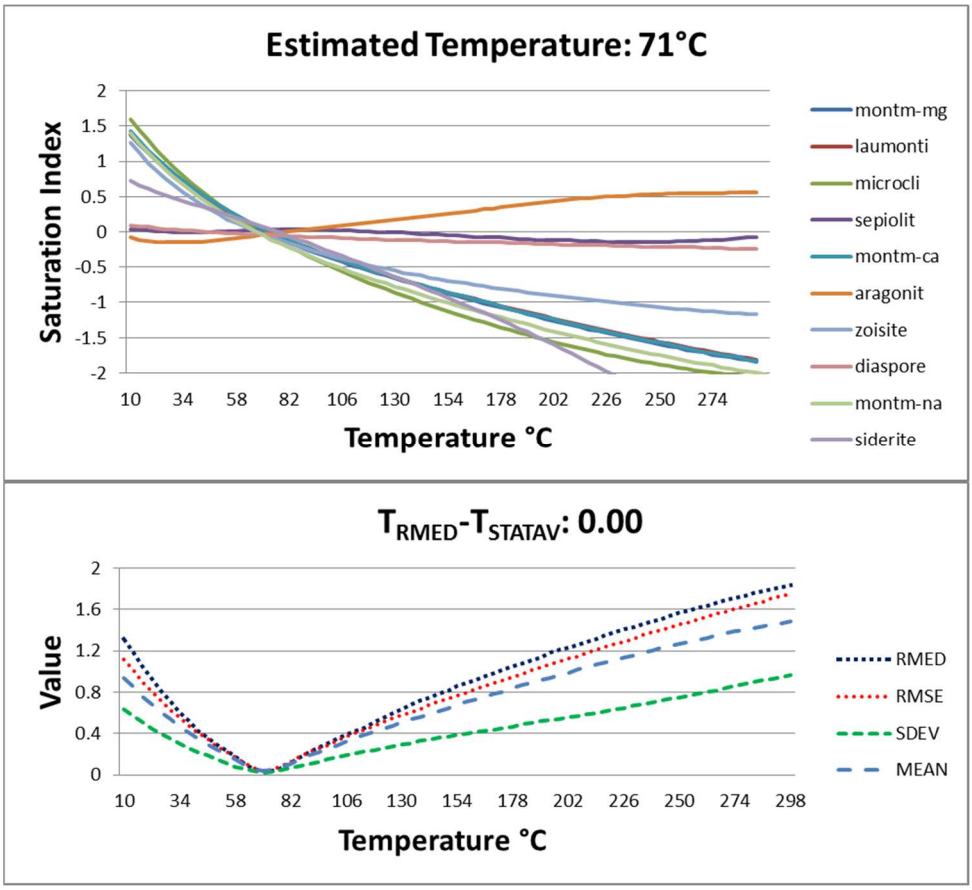

Figure 38: GeoT output using Shipherd's Hot Springs chemistry.

The GeoT inputs were amended to force inclusion of a free silica mineral and to eliminate minerals that did not fit within the geologic framework of the Wind River area. Both chalcedony and quartz were used to identify possible proximal mineral assemblages. Figures 39 and 40 show the resultant plots for St. Martin's Hot Spring, with a temperature estimate of 68 °C ±5.26 °C for the listed chalcedony suite, and an estimate of 97 °C 3.35 °C for the listed quartz suite. Figures 41 and 42 show the resultant plots for

Shipherd's Hot Spring sample, with a temperature estimate of 55 ± 3.21 °C for the listed chalcedony suite, and an estimate of 85 ± 3.85 °C for the listed quartz suite.

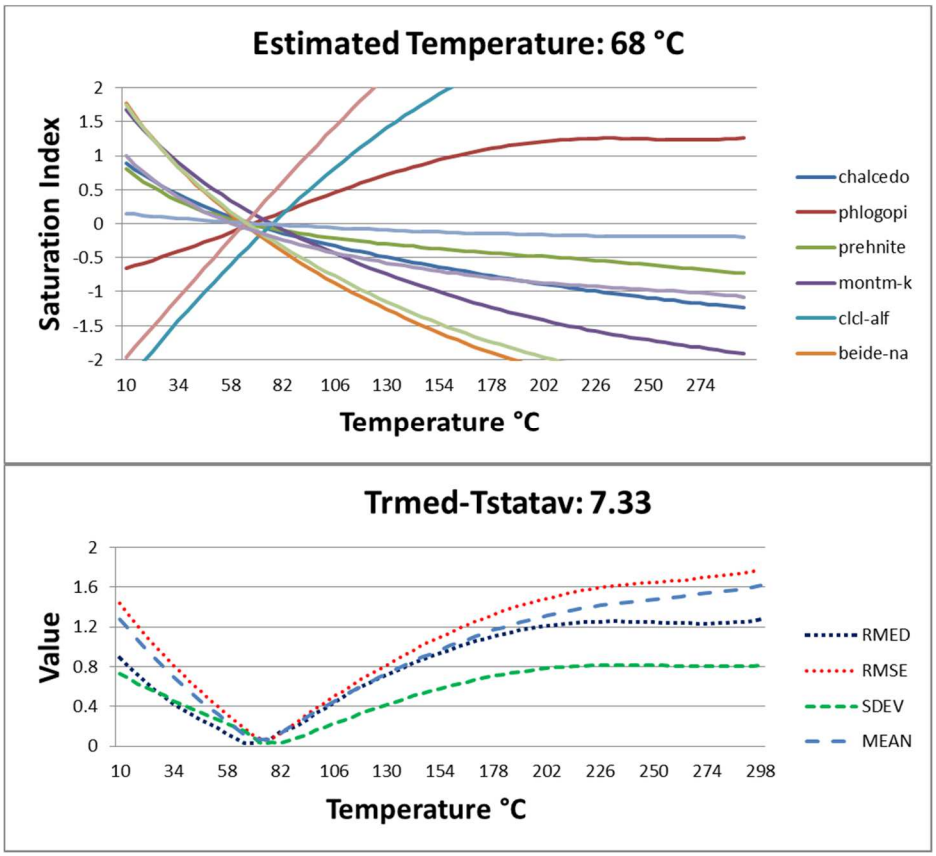

Figure 39: GeoT output for St. Martin's Hot Spring using chalcedony.

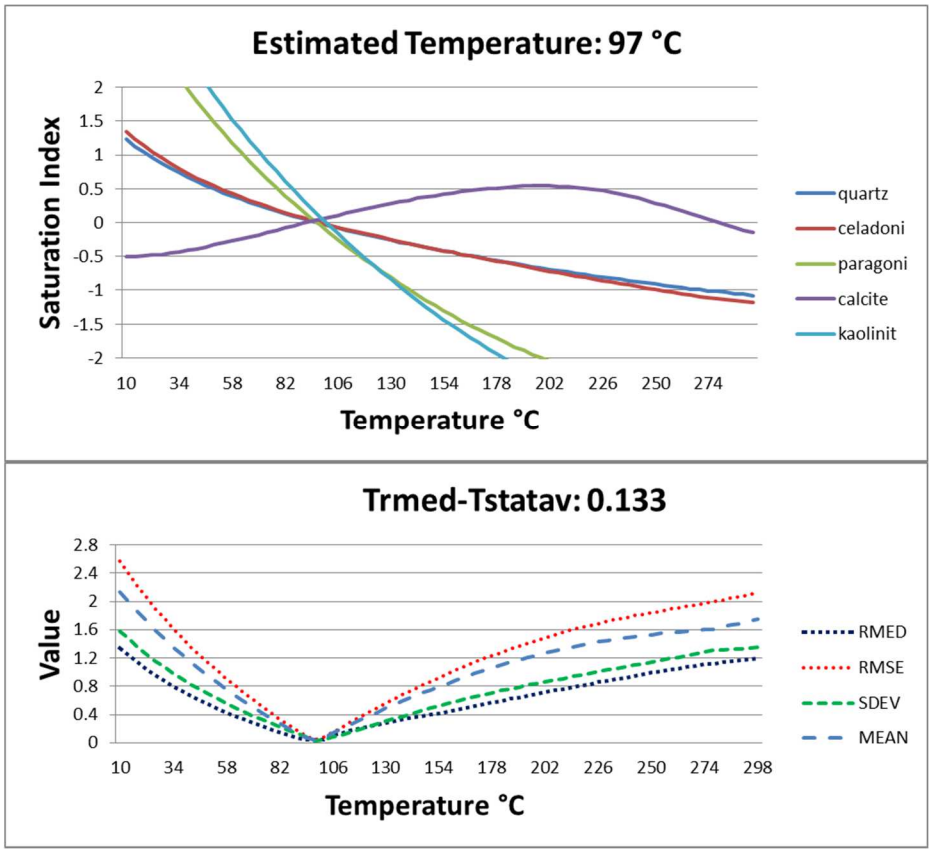

Figure 40: GeoT output for St. Martin's Hot Spring using quartz.

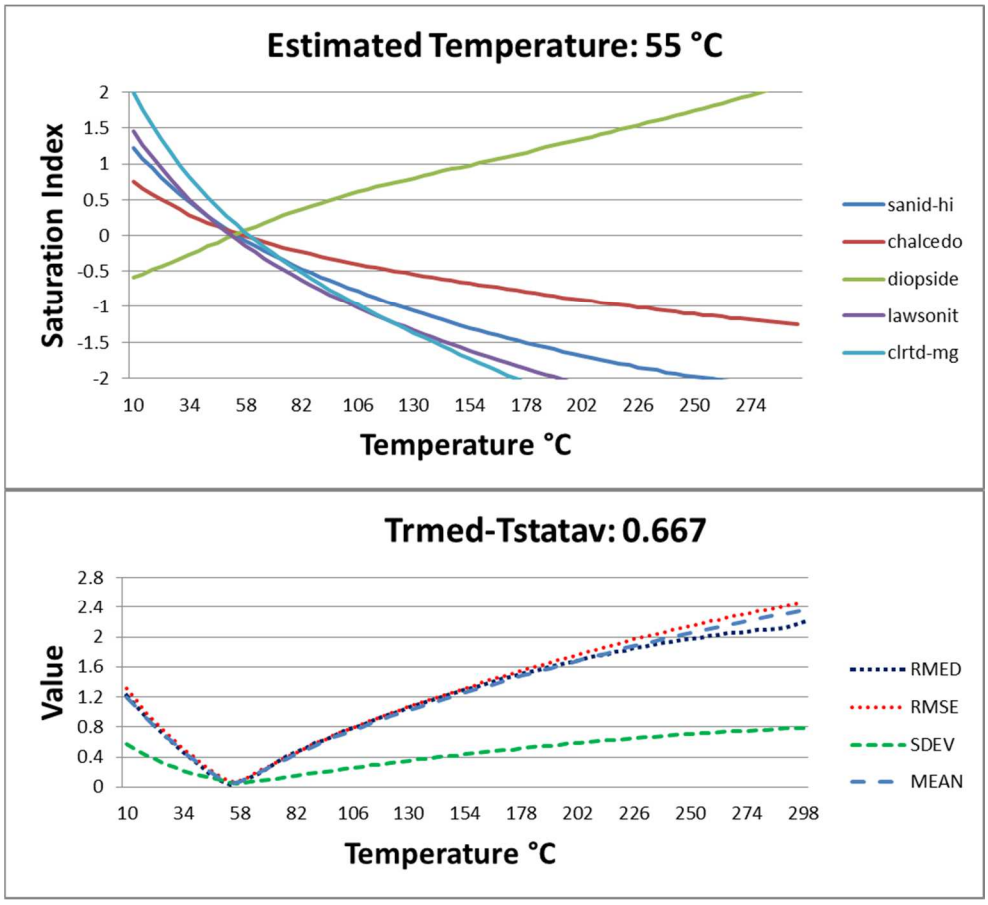

Figure 41: GeoT output from Shipherd's Hot Spring using minerals with SI=0 close to chalcedony equilibrium.

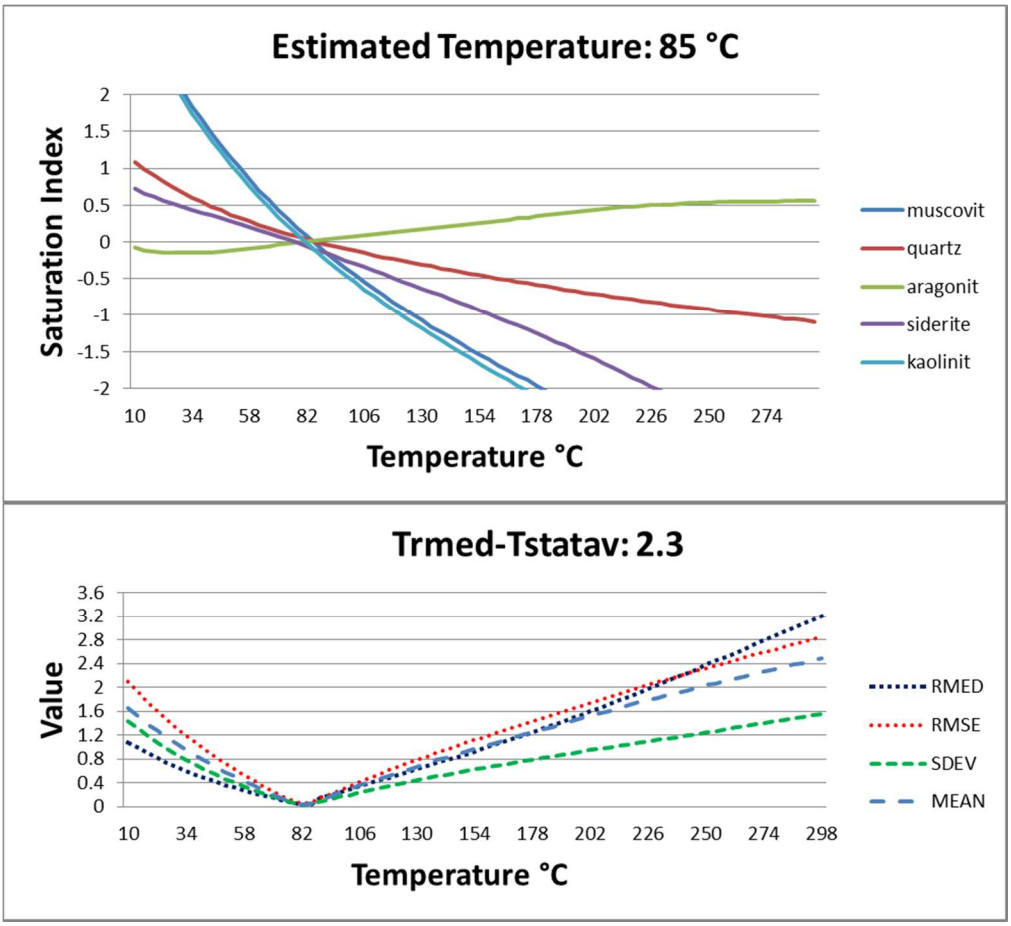

Figure 42: GeoT output using from Shipherd's Hot Spring using quartz mineral assemblage.

4.3.2.1 Optimization

Optimization of the St. Martins Hot Spring chemistry using a quartz mineral assemblage resulted in a temperature estimate of 83 ±2.28 °C and approximately 17% steam loss (Figure 43). Optimization for St. Martins using a chalcedony mineral assemblage resulted in a temperature estimate of 101°C ±3.2 °C, with an associated

concentration factor of 1.8, suggesting mixing between a mass of dilute water almost equal to that of the thermal water prior to its discharge at the surface.

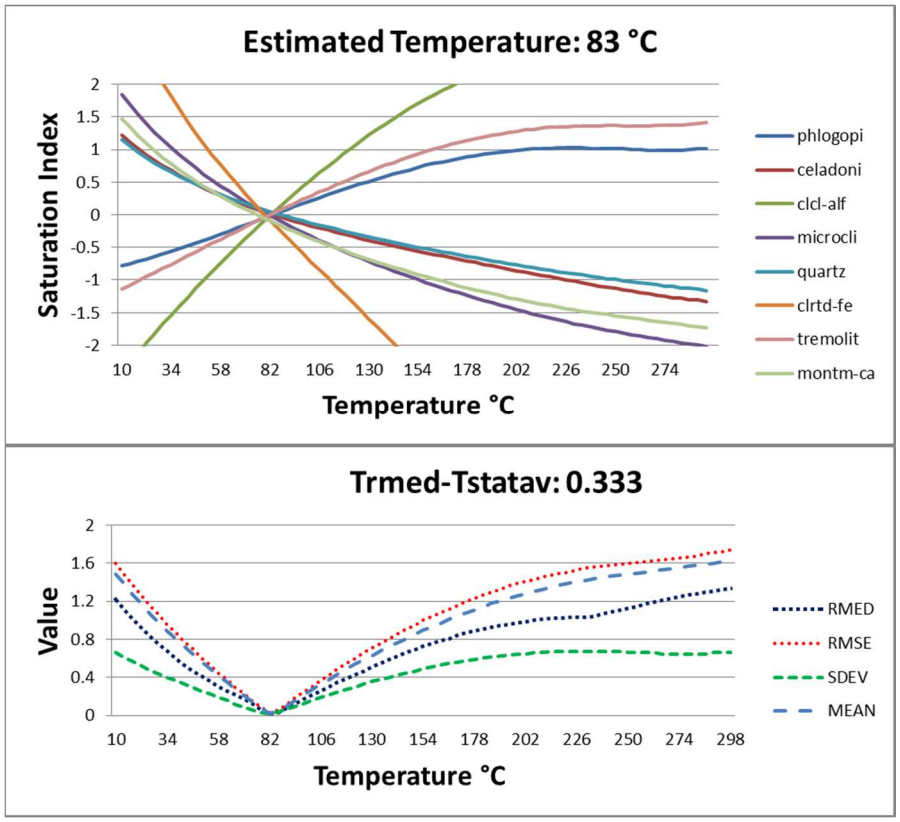

Figure 43: Optimized GeoT output corresponding to approximately 17% steam loss from St Martins Hot Spring.

Optimization of Shipherd's Hot Spring chemistry with a quartz mineral assemblage yielded a temperature estimate of 80 °C ±2.87°C and 20% water loss. Optimization using a chalcedony mineral assemblage (Figure 44) yielded a temperature estimate of 93 °C±58°C and a concentration factor of 2.74, implying that the thermal

water has mixed with almost three times its volume in dilute water before discharging at the spring.

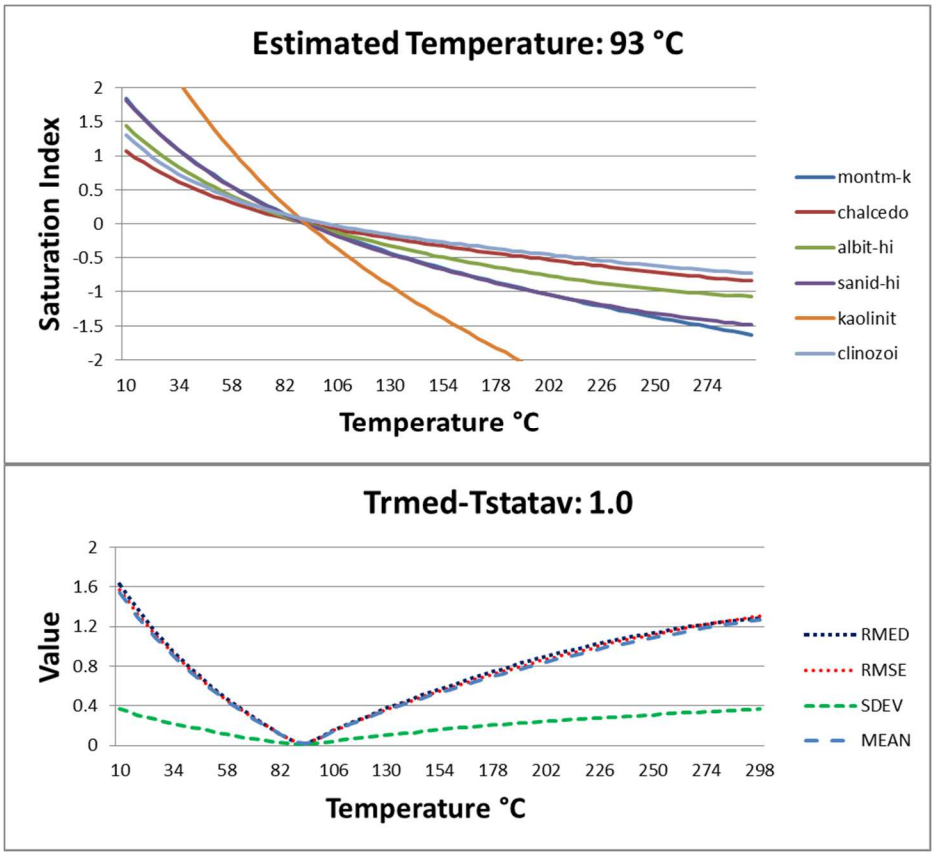

Figure 44: Optimized GeoT output for Shipherd's Hot Spring using the listed mineral assemblage.

4.3.3 RTEst

RTEst was applied for the Wind River Valley samples in a similar fashion to its application at Breitenbush Hot Springs. Figure 45 shows the initial mineral suite estimation using Geochemist's Workbench. This initial snapshot indicates a number of

possible minerals in equilibrium with chalcedony, and few close to equilibrium with quartz.

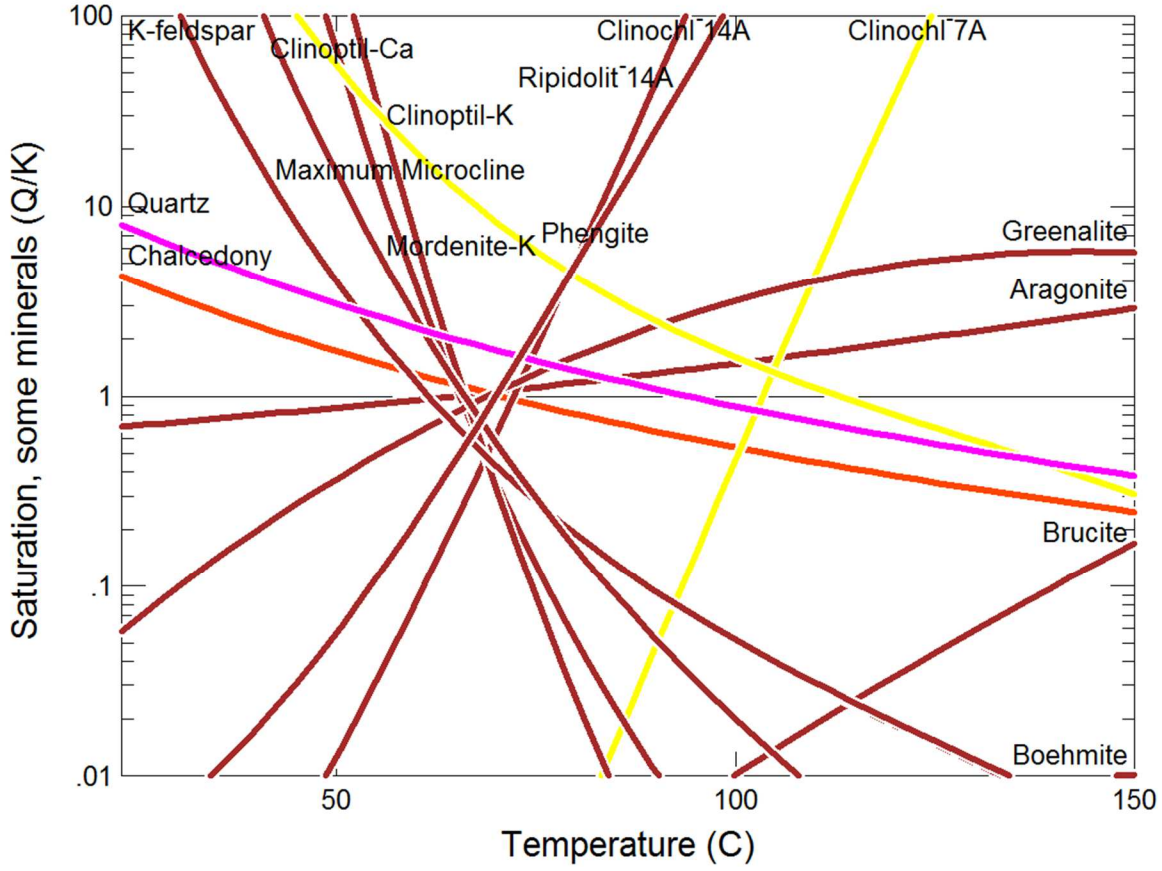

Figure 45: Initial mineral suite estimation based on St. Martin's Hot Springs water chemistry. Minerals close to the chalcedony (orange) equilibrium temperature are in brown. Quartz does not seem to cross close to any minerals, though those colored yellow are possible fits.

RTEst output for St. Martin's Hot Springs using a chalcedony mineral assemblage resulted in a temperature estimate of 83 °C when constraining all three parameters with minerals chalcedony, clinoptilolite, clinochlore, and aragonite (Figure 46). Optimized

dH_2O was -0.24 kg, suggesting dilution by surface waters. Optimized log (fCO_2) was -2.5, which is approximately one order of magnitude greater than present in initial speciation, suggesting loss of CO_2 during ascent. I was unable to generate a temperature estimate with reasonably constrained standard error using a quartz mineral assemblage for St. Martin's Hot Springs with RTEst. This suggests that the initial snapshot of equilibrium conditions (Figure 45) showing quartz far from equilibrium with St. Martin's Hot Spring water may be accurate.

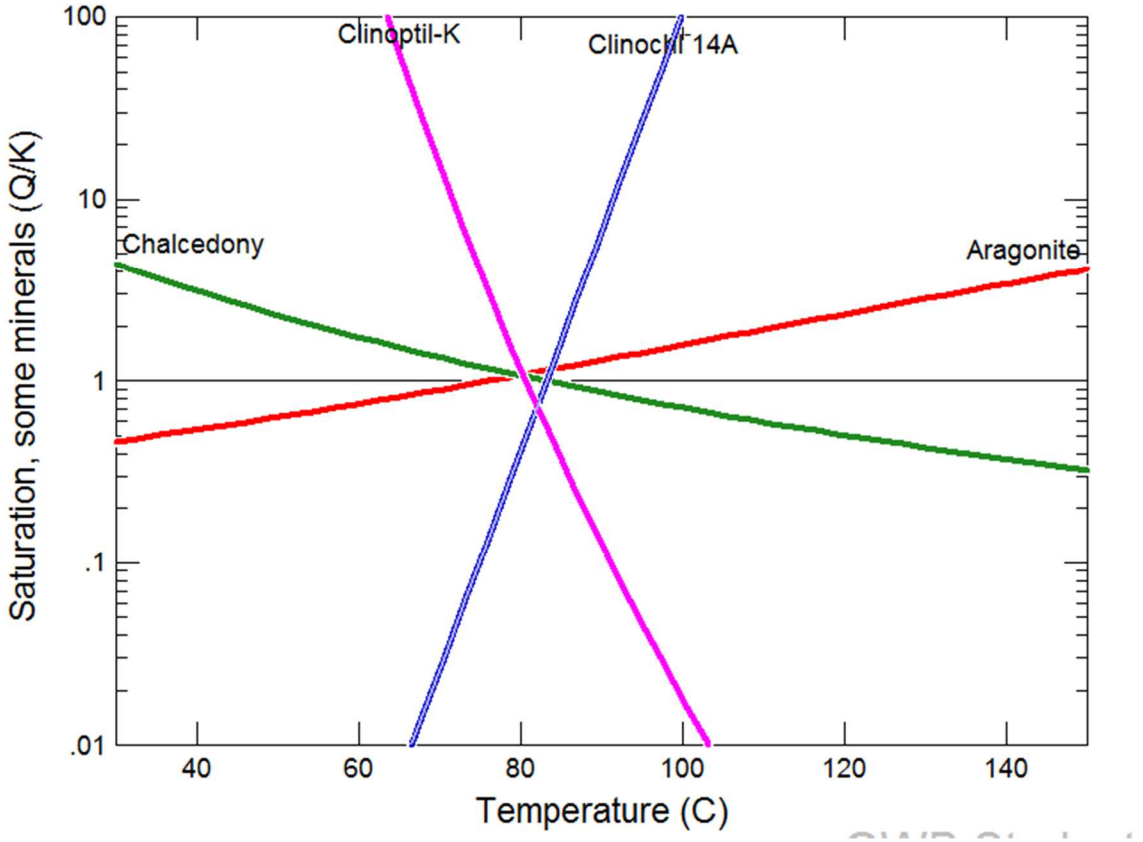

Figure 46: RTEst output for St. Martin's Hot Spring water showing an estimated temperature of 83°C.

The optimized temperature for Shipherd's Hot Spring using a mineral assemblage consisting of chalcedony, clinoptilolite, and siderite was 83 ± 10.4 ° C (Figure 47). Optimized dH_2O was -0.34, indicating mixture with a dilute source. Optimization was not possible with log (fCO_2) for this sample without resulting in an unreasonable range of temperatures. Using quartz, chamosite, and aragonite, the optimized temperature was 85 ±6.8 °C with an increase in water mass of 0.09 kg, suggesting steam loss. Similar to the chalcedony assemblage, optimization with log (fCO_2) increased the error substantially, with a resultant temperature of 85 ±26.1 °C. No shallow water sample was available for use in RTEst's mixing optimization schema.

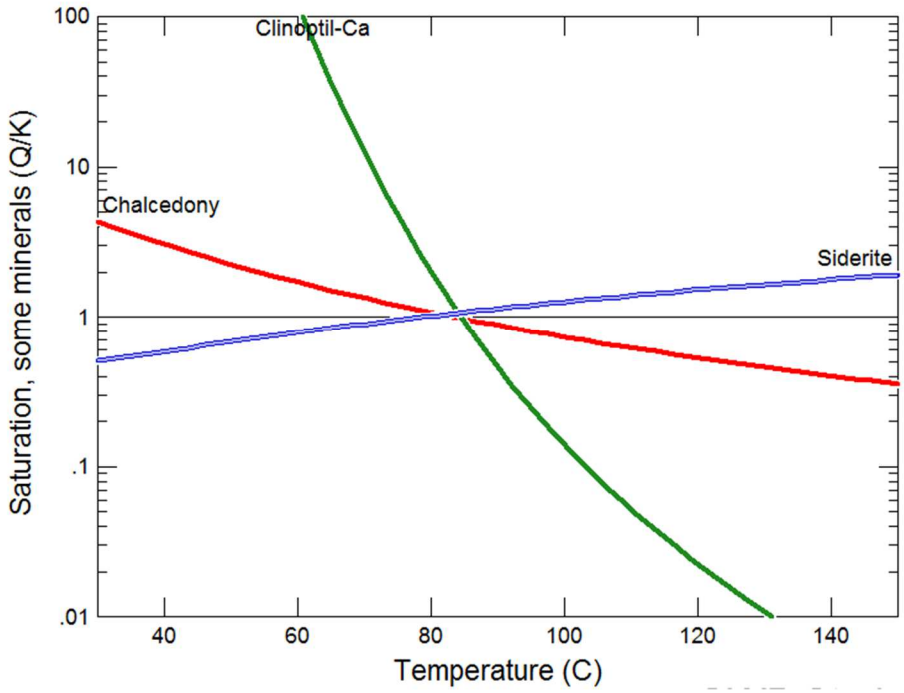

Figure 47: RTEst output for Shipherd's Hot Spring with an estimated temperature of 83°C.

4.3.4 Discussion

A curious feature of the Wind River sample results is the consistency between the silica concentrations of the two springs and the disparity between them when almost every other analyte is considered. It is tempting to imagine that Shipherd's represents the product of mixing between shallow, cool water and water of the St. Martin's reservoir (as seemed to be the case on the Piper Diagram [Figure 14] and the isotope plot [Figure 13]). If this is the case, however, we would expect the silica values to also be much lower in the Shipherd's Hot Spring sample. This could indicate silica precipitation of the St. Martin's Hot Spring sample during ascent. Based on geothermometry results, it appears that St. Martin's and Shipherd's Hot Springs have the same thermal source, but that Shipherd's has mixed with a greater quantity of shallow, dilute waters.

For both spring samples, the GeoT optimization suggested that if the water had been in equilibrium with quartz, it would have meant substantial steam loss during ascent. This was also true of the Shipherd's RTEst quartz mineral assemblage result. In contrast, both GeoT and RTEst suggest dilution of waters during ascent for the chalcedony mineral assemblages, with more dilution for Shipherd's Hot Spring. Considering the proximity to the Wind River, the precipitation in the days before the sampling event, the number of shallow seeps in the vicinity, and the apparent mixing pathways between the two springs, it seems more likely that the reservoir is in equilibrium with the chalcedony assemblage. In addition, chalcedony is a lower temperature polymorph and, based on all geothermometers assessed for Shipherd's and

St. Martin's Hot Springs, the Wind River geothermal system appears to be a low temperature resource.

Optimized temperature estimates range from 83 °C using RTEst to 101 °C using GeoT. This discrepancy is possibly due to differences in the thermodynamic databases used for the programs, which affects the mineral selection process in that different groups of minerals appear closer to equilibrium with each other than other possible assemblages. The optimized amount of mixing with shallow waters was also higher for GeoT (for St. Martin's 1.8) than it was for RTEst (for St. Martin's 1.24), which explains why the estimate with GeoT is higher. The RTEst estimate is consistent between springs and mineral assemblages (83, 83, and 85 °C) in contrast to the apparent spread in the GeoT estimate (80, 83, 93, and 101 °C).

5 CONCLUSIONS

5.1 Breitenbush Hot Springs

The most likely reservoir temperature for Breitenbush Hot Springs corresponds to chalcedony equilibrium at a temperature of approximately 137 °C. This value is close to the maximum recorded borehole temperature in the SUNEDCO well of 141 °C (Conrey and Sherrod, 1988) and is supported by fluid inclusion data and the apparent order of mineral formation within the thermal aquifer identified in the SUNEDCO well (Bargar, 1994). Multi-component geothermometry outputs using a mineral assemblage consisting of chalcedony, mordenite-K, heulandite, and calcite were able to explain many of the minerals observed in the nearby geothermal wells and showed consistency in estimated reservoir conditions, including a temperature of 137 ±2 °C.

An estimated reservoir temperature of 137 °C contrasts with past reservoir temperature estimates, which range from 174 to 180 °C for both classic and multi-component geothermometry (Forcella, 1982; Ingebritsen et al., 1992; Pang and Reed, 1998; Spycher et al., 2016). These estimates relied on either equilibrium with quartz (which would preclude the presence of chalcedony which shows undersaturation when quartz is in equilibrium) or anhydrite (which would preclude the presence of pyrite and chalcopyrite due to a difference in oxidation state). Chalcedony, pyrite, and chalcopyrite were commonly observed in nearby geothermal wells (Bargar, 1994). Previous multi-

component temperature estimates used forced equilibrium to determine Al concentrations that were several orders of magnitude greater than those detected in Breitenbush well and spring samples analyzed as part of this thesis. Using higher Al concentrations is counter to the pattern observed during time-series sampling of W10, which showed a reduction in Al concentrations as time elapsed. When deriving Al concentrations from assumed equilibrium with K-feldspar while optimizing with a chalcedony-based mineral assemblage, the resultant Al concentrations are consistent with the pattern of observed Al distribution in wells and springs.

Isotopic data from samples collected for this thesis indicates between 6 and 10 percent mixing with "andesitic waters" of Giggenbach (1992), suggesting the hot springs are contributed to by subducted ocean and oceanic sediment interacting with the upper mantle. This fits within the framework described by Mariner et al. (2003) that postulates a sedimentary source for chloride and calcium, and a magmatic source for He. Isotopic data further suggest that the remainder of the thermal waters is sourced from precipitation deposited near the Cascade crest, based on depletion of isotopes relative to nearby meteoric water. A higher elevation source for Breitenbush Hot Spring water is consistent with a narrow High Cascade heat source for the area that is then distributed laterally, as described by Ingebritsen et al. (1992).

5.2 Wind River Hot Springs

Both Wind River hot springs seem to share the same thermal source. Whereas Shipherd's Hot Spring shows more dilution, St. Martin's Hot Spring shows the potential of silica precipitation during ascent. Based on multi-component geothermometry, a reservoir temperature between 83 and 100 °C is likely for these springs. This conclusion is consistent with previous estimates of Wind River Hot Spring reservoir temperatures. Although specific deep mineralogy was not available, the application of multi-component geothermometry to the Wind River geothermal system was constrained by knowledge of likely mineral occurrence. In this regard, the lack of subsurface data did not significantly hinder this study. The collection of a shallow, dilute end-member sample, such as from Gunderson Spring, would have allowed use of the GeoT and RTEst mixing modules which could have increased confidence in these estimates.

An estimate of less than 100 °C for the Wind River Valley reservoir temperature contrasts with a reported geothermal gradient of 160 °C/km. This steep gradient was extrapolated from a well with a bottom hole temperature of 28 °C. It is likely that the extrapolated thermal gradient is not realistic. The temperature estimates generated during this thesis are consistent with theoretical heat source being a shallow cooling intrusion (Czajkowski et al., 2013).

5.3 Multi-Component Geothermometers

For GeoT and RTEst, there appears to be a built-in hierarchy of effective utilization and parameter optimization. Based on these results, the list of components in order of importance is:

- Mineral selection
- Thermodynamic database
- Weighting scheme (for RTEst)
- Concentration/dilution parameter
- Shallow water mixing parameter
- Gas loss parameter
- Activity correction parameters

Without successful mineral selection it is not possible to find success in multi-component geothermometry, despite the sophistication of optimization schema that can be incorporated. In this regard, a possibility for future multi-component geothermometer development would be the incorporation of a method with which to automatically test various mineral assemblages. The use of PEST regularization and prediction modes to identify range of possible "correct" estimates could also be a useful method of further constraining uncertainty and potential strength of fits for each potential assemblage.

6 REFERENCES

Arnórsson S, Fridriksson T, Gunnarsson I, 1998, Gas chemistry of the Krafla geothermal field, Icelan, Proc. International Symposium on Water-Rock Interaction, Auckland, New Zealand p. 613-616.

Arnórsson, S., 2000, Isotopic and Chemical Techiques In Geothermal Exploration (S. Arnórsson, Ed.): International Atomic Energy Agency, Vienna, Austria.

Bargar, K.E., 1994, Hydrothermal alteration in the SUNEDCO 58-28 geothermal drill hole near Breitenbush hot springs, Oregon: Oregon Geology, v. 56, no. 4, p. 75–87.

Berri, D.A., and Korosec, M.A., 1983, Geological and geothermal investigation of the lower Wind River valley, Southwestern Washington Cascade Range: State of Washington Department of Natural Resources, Division of Geology and Earth Resources, v. Open File, p. 48.

Blackwell, D.D., and Baker, S.L., 1988, Thermal analysis of the Austin and Breitenbush geothermal systems , Western Cascades, Oregon: USGS Open File Report 0-88-5, p. 47–62.

Boschmann, Darrick, Czajkowiski, Jessica, and Bowman, J., 2014, Geothermal favorability model of Washington State: , no. July 2014.

Brooks, J.R., Wigington, P.J., Phillips, D.L., Comeleo, R., and Coulombe, R., 2012, Willamette River Basin surface water isoscape ($\delta^{18}O$ and $\delta^{2}H$): temporal changes of source water within the river: Ecosphere, v. 3, no. 5, p. art39, doi: 10.1890/ES11-00338.1.

Conrey, R.M., and Sherrod, D.R., 1988, Stratigraphy of drill holes and geochemistry of surface rocks , Breitenbush Hot Springs 15-minute quadrangle, Cascade Range, Oregon: USGS Open File Report 0-88-5, p. 15–30.

Czajkowski, J.L., Bowman, J.D., Fusso, L.A., and Boschmann, D.E., 2013, Geologic Map and Geothermal Assessment of the Wind River Valley , Skamania County , Washington: , p. 108.

Czajkowski, J.L., Bowman, J.D., Fusso, L.A., and Boschmann, D.E., 2014, Geologic mapping and geothermal assessment of the Wind River Valley, Skamania County, Washington: Washington Division of Geology and Earth Resources, v. Open File, no. March 2014.

Forcella, L., 1982, Geochemistry of Thermal and Mineral Waters in the Cascade Mountains of Western North America: Ground Water, v. 20, no. 1, p. 39–47.

Fouillac, C., and Michard, G., 1981, Sodium/lithium ratio in water applied to

geothermometry of geothermal reservoirs: Geothermics, v. 10, no. 1, p. 55–70, doi: 10.1016/0375-6505(81)90025-0.

Fournier, R.O., 1977, Chemical geothermometers and mixing models for geothermal systems: Geothermics, v. 5, no. 1–4, p. 41–50, doi: 10.1016/0375-6505(77)90007-4.

Fournier, R.O., and Potter, R.W., 1982, An equation correlating the solubility of quartz in water from 25° to 900°C at pressures up to 10,000 bars: Geochimica et Cosmochimica Acta, v. 46, no. 10, p. 1969–1973, doi: 10.1016/0016-7037(82)90135-1.

Fournier, R.., and Potter, R.., 1979, Magnesium correction to the Na□K□Ca chemical geothermometer: Geochimica et Cosmochimica Acta, v. 43, no. 9, p. 1543–1550, doi: 10.1016/0016-7037(79)90147-9.

Fournier, R.O., and Rowe, J.J., 1966, Estimation of underground temperatures from the silica content of water from hot springs and wet-steam wells: American Journal of Science, v. 264, no. 9, p. 685–697, doi: 10.2475/ajs.264.9.685.

Fournier, R.O., and Truesdell, a. H., 1973, An empirical Na□K□Ca geothermometer for natural waters: Geochimica et Cosmochimica Acta, v. 37, no. 5, p. 1255–1275, doi: 10.1016/0016-7037(73)90060-4.

Fournier, R.O., and Truesdell, A.H., 1970, Chemical indicators of subsurface temperature applied to hot spring waters of Yellowstone National park, Wyoming, U.S.A.: Geothermics, v. Special Is, no. 2, p. 529–535.

Garchar, L., Badgett, A., Nieto, A., Young, K., Hass, E., Weathers, M., Renewable, N., and Parkway, D.W., 2016, Geothermal Play Fairway Analysis : Phase I Summary: , no. October 2014, p. 1930–1942.

Gherardi, F., and Spycher, N., 2014, Application of integrated multicomponent geothermometry at the Chachimbiro thermal area , a difficult geothermal prospection case: Proceedings , Thirty-Eighth Workshop on Geothermal Reservoir Engineering, Stanford University, p. 1–6.

Giggenbach, W.F., 1988, Geothermal solute equilibria. Derivation of Na-K-Mg-Ca geoindicators: Geochimica et Cosmochimica Acta, v. 52, no. 12, p. 2749–2765, doi: 10.1016/0016-7037(88)90143-3.

Giggenbach, W.F., 1992, Isotopic shifts in waters from geothermal and volcanic systems along convergent plate boundaries and their origin: Earth and Planetary Science Letters, v. 113, no. 4, p. 495–510, doi: 10.1016/0012-821X(92)90127-H.

Grainey, M.W., 2014, Geothermal Energy in Oregon : Job Creation and Other Benefits From New Geothermal Technologies Recent Technology : The Emergence of Geothermal Electricity in Oregon: GRC Transactions, v. 38, p. 65–70.

Gran, G., 1952, Determination of the equivalence point in potentiometric titrations. Part II: The Analyst, v. 77, no. 920, p. 661–671, doi: 10.1039/an9527700661.

Guffanti, M., and Muffler, L.J.P., 1995, Geothermal Potential of Diverse Volcanotectonic Settings of the Cascade Range: Proceedings of the World Geothermal Congress, 1995, v. 1, p. 719–724.

Hammond, P.E., 1979, A tectonic model for evolution of the Cascade Range, *in* Pacific Coast Paleogeography Symposium 3: Cenozoic Paleogeography of the Western United States, p. 219–237.

Hook, J., 2005, Geothermal Energy from the Cascades: GRC Transactions, v. 30, p. 263–265, doi: 10.1080/09640560701402075.

Ingebritsen, S.E., Sherrod, D.R., and Mariner, R.H., 1992, Rates and patterns of groundwater flow in the Cascade Range Volcanic Arc, and the effect on subsurface temperatures: Journal of Geophysical Research, v. 97, no. B4, p. 4599–4627.

Jutzeler, M., 2013, Characteristics and origin of subaqueous pumice-rich pyroclastic facies Ohanapecosh Formation (USA) and Dogashima Form: , p. 193.

Keith, T.E.C., 1988, Regional patterns of hydrothermal alteration in the Breitenbush-Austin Hot Springs area of the Cascade Range, Oregon: USGS Open File Report 0-88-5, p. 31–38.

Mariner, R.H., Evans, W.C., Presser, T.S., and White, L.D., 2003, Excess nitrogen in selected thermal and mineral springs of the Cascade Range in northern California, Oregon, and Washington: Sedimentary or volcanic in origin? Journal of Volcanology and Geothermal Research, v. 121, no. 1–2, p. 99–114, doi: 10.1016/S0377-0273(02)00414-6.

Mariner, R.H., Presser, T.S., and Evans, W.C., 1993, Geothermometry and water—rock interaction in selected thermal systems in the cascade range and modoc plateau, western United States: Geothermics, v. 22, no. 1, p. 1–15, doi: 10.1016/0375-6505(93)90017-H.

Morey, G.., Fournier, R.., and Rowe, J.., 1962, The solubility of quartz in water in the temperature interval from 25° to 300° C: Geochimica et Cosmochimica Acta, v. 26, no. 10, p. 1029–1043, doi: 10.1016/0016-7037(62)90027-3.

Neupane, G., Mattson, E.D., Mcling, T.L., Palmer, C.D., Smith, R.W., and Thomas, R., 2014, Deep geothermal reservoir temperatures in the eastern Snake River Plain , Idaho using multicomponent geothermometry: Proceedings , Thirty-Eighth Workshop on Geothermal Reservoir Engineering, Stanford University, p. 1–12.

Palandri, J.L., Reed, M.H., Sciences, G., and March, R., 2001, Reconstruction of in situ composition of sedimentary formation waters: Geochimica et Cosmochimica Acta, v. 65, no. 11, p. 1741–1767, doi: 10.1016/S0016-7037(01)00555-5.

Palmer, C.D., 2015, Reservoir temperature estimator (RTEst) user's manual. IN: Mattson, E.D., Smith, R.W., Neupane, G., Palmer, D.D., Fujita, Y., McLing, T.L., Reed, D.W., Cooper, C., and Thompson, V.S., 2015, Improved geothermometry through multivariate reaction-path modeling and evaluation of geomicrobiological influences on geochemical temperature indicators: Idaho National Laboratory, INL/EXT-14-33959.

Pang, Z.H., and Reed, M., 1998, Theoretical chemical thermometry on geothermal waters: problems and methods: Geochimica et Cosmochimica Acta, v. 62, no. 6, p. 1083–1091, doi: 10.1016/S0016-7037(98)00037-4.

Powell, T., Cumming, W., and Zealand, N., 2010, Spreadsheets for Geothermal Water and Gas Geochemistry: Water, v. 9, no. 1174–5878 (Print) LA–eng PT–Case Reports PT–Journal Article PT–Research Support, Non–U.S. Gov't RN–0 (Anesthetics, Local) RN–137–58–6 (Lidocaine) SB–IM, p. 10.

Priest, G.R., 1990, Volcanic and tectonic evolution of the Cascade Volcanic Arc, Central Oregon: Journal of Geophysical Research, v. 95, no. B12, p. 585–599.

Reed, M.H., 1982, Calculation of multicomponent chemical equilibria and reaction processes in systems involving minerals, gases and an aqueous phase: Geochimica et Cosmochimica Acta, v. 46, no. 4, p. 513–528, doi: 10.1016/0016-7037(82)90155-7.

Reed, M., and Spycher, N., 1984, Calculation of pH and mineral equilibria in hydrothermal waters with application to geothermometry and studies of boiling and dilution: Geochimica et Cosmochimica Acta, v. 48, no. 7, p. 1479–1492, doi: 10.1016/0016-7037(84)90404-6.

Sherrod, D.R., 1988, Geology and geothermal resources of the Bretenbush-Austin hot springs area, Clackamas, and Marion counties: USGS Open File Report 0-88-5, p. 91.

Sherrod, D.R., and Conrey, R.M., 1988, Geologic setting of the Breitenbush-Austin Hot Springs area, Cascade Range, north-central Oregon: USGS Open File Report 0-88-5, p. 1–14.

Sifford, A., 2014, Geothermal Energy in Oregon: GRC Transactions, v. 38, p. 99–106.

Sonnenthal, E., Spycher, N., Callahan, O., Cladouhos, T., Petty, S., Division, E.S., Berkeley, L., and Energy, A., 2012, a Thermal-Hydrological-Chemical Model for the Enhanced Geothermal System Demonstration Project At Newberry Volcano , Oregon:

Spycher, N., Finsterle, S., Dobson, P., Berkeley, L., and Road, C., 2016, New Developments in Multicomponent Geothermometry: , p. 1387–1395.

Spycher, N., Peiffer, L., and Sonnenthal, E., 2014, GeoT user ' s guide, a computer program for multicomponent geothermometry and geochemical speciation:

Lawrence Berkeley National Laboratory Report Number LBNL-6172E (rev.), p. 1–38.

Truesdell, H., and Fournier, R.O., 1976, Conditions in the deeper parts of the hot springs systems of Yellowstone National Park, Wyoming: USGS Open File Report 76-428, p. 1–25.

Verma, S.P., Pandarinath, K., and Santoyo, E., 2008, SolGeo: A new computer program for solute geothermometers and its application to Mexican geothermal fields: Geothermics, v. 37, no. 6, p. 597–621, doi: 10.1016/j.geothermics.2008.07.004.

Verma, S.P., and Santoyo, E., 1997, New improved equations for Na/K,Na/Li, and SiO2 geothermometers by outlier detection and rejection: Journal of Volcanology and Geothermal Research, v. 79, no. 1–2, p. 9–23, doi: 10.1016/S0377-0273(97)00024-3.

Waibel, A., 1983, An assessment of Heidgerken Breitenbush wells 1, 2, and 3, Marion County, Oregon: Columbia Geosciences, p. 24.

Walther, J. V, and Helgeson, H.C., 1977, Calculation of thermodynamic properties of aqueous silica and solubility of quartz and its polymorphs at high-pressures and temperatures: American Journal of Science, v. 277, no. 10, p. 1315–1351, doi: 10.2475/ajs.277.10.1315.

Wanner, C., Peiffer, L., Sonnenthal, E., Spycher, N., Iovenitti, J., and Kennedy, B.M., 2013, On the use of chemical geothermometry: A reactive transport modeling study of the Dixie Valley geothermal area: Procedia Earth and Planetary Science, v. 7, p. 884–887, doi: Doi 10.1016/J.Proeps.2013.03.107.

White, D.E., 1970, Geochemistry applied to the discovery, evaluation, and exploitation of geothermal energy resources: Proceedings of the U.N. Symposium on the Development and Utilization of Geothermal Resources, Pisa, v. 1, no. 2, doi: 10.1017/CBO9781107415324.004.

APPENDIX A: OREGON WATER RESOURCES DEPARTMENT WELL LOGS FOR BREITENBUSH HOT SPRING RESORT WELLS

Appendix A consists of nine .pdf files. Files are named based on the well displayed on the well log. The following wells are included: W1, W2, W3, W4, W11, W12, W14, and W15. Files can be accessed at the Portland State digital archive:

http://pdxscholar.library.pdx.edu/

APPENDIX B: LABORATORY QUALITY CONTROL

RESULTS

Appendix B consists of a .csv file containing laboratory quality control results. The file can be accessed at the Portland State digital archive:

http://pdxscholar.library.pdx.edu/

APPENDIX C: GEOT INPUT FILES

Appendix C consists of 47 .inp files used with GeoT to generate the results tabulated in Table 10. The files are labeled based on the well from which the sample with the input chemistry was collected. For each well, there is at least one quartz and one chalcedony mineral assemblage relating to the associated assemblages listed on Table 10. Quartz assemblages are indicated by the letter 'q' after the sample name. Chalcedony assemblages are indicated by the letter 'c' after the sample name. For the W10 time series, the naming scheme is W10 followed by the temperature of collection. For example, W1082c is the input file associated with the sample collected from W10 at 82 °C using a chalcedony mineral assemblage and W1072q is the input file associated with the sample collected from W10 at 72°C using a quartz mineral assemblage. Files can be accessed at the Portland State digital archive:

http://pdxscholar.library.pdx.edu/

APPENDIX D: PEST FILES USED WITH GEOT

Appendix D consists of the .ins, .pst, and .tpl files used for optimization of GeoT to generate the results tabulated in Table 10. Each file type is located in a separate sub-file on the server

Instruction files: There are only two .ins files. The first, 'Geot.ins,' is used for PEST runs when analyzing one water chemistry at a time. The second, 'allwaters.ins' is used for PEST optimization for all waters simultaneously. Currently the files are stored as 'filenameins.txt'. Before running pest, it would be necessary to change this to 'filename.ins.'

PEST Files: A total of 37 .pst files are included in the Appendix D. The .pst files are named based on the well or spring from which the sample was collected. For example, "sulphurc.pst" is the file used to optimize water collected from Sulphur Spring using a chalcedony mineral assemblage.

Template Files: A total of 37 .tpl files are included in Appendix D. The .tpl files are named similarly to their corresponding .pst files. For example "W1q.tpl" represents the template file used with "W1q.pst" for optimization of W1 water chemistry using a quartz mineral assemblage. These files need to be changed to "GeoT_inp.tpl" in the chosen PEST directory prior to using.

Files can be accessed at the Portland State digital archive:

http://pdxscholar.library.pdx.edu/

APPENDIX E: RTEST INPUT AND REACT FILES

Appendix E consists of files for use with RTEst. The files in this appendix are arranged in folders associated with a particular sample. Each folder contains at least one .rea file and two .txt files. The .rea file is the associated Geochemist's Workbench file. The .txt files are used as RTEst input files. For example, the folder "180" contains the files 180.rea 180chalcmins.txt, and 180qrtzmins.txt. Several folders contain react files used with the soltherm database. These files are labeled with Solt in their filename, for example "W10Solt.rea" is the react file used with the Soltherm database on water chemistry from W10. A total of 105 files are in Appendix E.

Files can be accessed at the Portland State digital archive:

http://pdxscholar.library.pdx.edu/